Thesis Project Portfolio

Design of a Processing Plant for the Extraction of Lithium from Geothermal Brines in the Salton Sea, California

(Technical Report)

A Care Ethics Analysis of BP and its Role in the Texas City Isomerization Unit Explosion

(STS Research Paper)

An Undergraduate Thesis

Presented to the Faculty of the School of Engineering and Applied Science
University of Virginia • Charlottesville, Virginia

In Fulfillment of the Requirements for the Degree
Bachelor of Science, School of Engineering

Hailey Elizabeth Hall
Spring, 2023
Department of Chemical Engineering

Table of Contents

Sociotechnical Synthesis

My technical report and STS research are connected through concepts of process safety, which encompasses the safe and effective design and maintenance of chemical facilities. Understanding hazards in process design is key to developing safer, more sustainable plants and units in chemical engineering systems. Though my STS research focuses on refining and my technical work encompasses lithium production, the need to minimize process hazards through inherently safer design and process management is essential across all chemical fields. By assessing risks and hazards in my STS thesis and developing a safe production process through my technical work, the importance of process safety through the entire lifecycle of a chemical facility is emphasized. Applying safety principles across various types of chemical processes provides opportunities to highlight the skills and creativity needed to implement hazard mitigating safeguards and promote strong safety culture.

The technical portion of my thesis focuses on lithium capture from geothermal brines using a novel technique developed by professors within the chemical engineering department. My capstone team designed a chemical processing unit to be retrofitted onto an existing geothermal power plant for the extraction and purification of lithium. The end product of our process is battery-grade lithium hydroxide monohydrate for use in electric vehicle batteries or grid-scale energy storage. My team designed the lithium extraction plant using hand calculations and ASPEN simulations to model brine properties. The proposed design utilizes environmentally friendly techniques to remove lithium from geothermal brines and is a net producer of water in an arid region of the United States. Throughout our design process, we considered risks and hazards to develop inherently safer units. We believe that our lithium extraction plant would increase the use and accessibility of green technologies while also providing a blueprint for a safer, more eco-friendly lithium production process.

My STS research studies the BP Texas City isomerization unit explosion that occurred in 2005. Numerous factors leading up to the incident caused safety to deteriorate within the plant, ultimately claiming the lives of 15 contractors. Care ethics, developed by Nel Noddings and Carol Gilligan, provides a framework to assess morality based on actions and attitudes of care. Using this framework, I claim that BP did not provide sufficient care to its Texas City site leading up to the incident. Through this analysis, I consider the aspects of care that BP neglected to provide and the safety shortages that contributed to the disaster. The care ethics analysis can easily be extended to other cases and highlights the importance of safety both in initial design and upkeep of a plant. Through this research, I hope to emphasize the importance of care and thus safety in chemical processing.

By performing my STS research and technical work simultaneously, each portion of my thesis helped inform and influence the other while enriching both. My technical design involved the selection of safe process materials and reliable equipment for use in a chemical plant, helping me better recognize shortcomings in care within my STS thesis case. At the same time, my STS thesis helped me identify ways to make inherently safer choices in my technical process and helped me conceptualize care in design. Together, the STS and technical papers built upon one another constructively to stress the importance of providing safe working conditions throughout the entire lifespan of a chemical manufacturing facility.

Design of a Processing Plant for the Extraction of Lithium from Geothermal Brines in the Salton Sea, California

A Technical Report submitted to the Department of Chemical Engineering

Presented to the Faculty of the School of Engineering and Applied Science
University of Virginia • Charlottesville, Virginia

In Partial Fulfillment of the Requirements for the Degree
Bachelor of Science, School of Engineering

Hailey Elizabeth Hall
Spring, 2022
Technical Project Team Members
William Ferguson
Lena Keesecker
Kijeong Nam
Sean Robinson

On my honor as a University Student, I have neither given nor received unauthorized aid on this assignment as defined by the Honor Guidelines for Thesis-Related Assignments

Eric Anderson, Department of Chemical Engineering

TABLE OF CONTENTS

EXECUTIVE SUMMARY

Fueled by increased demand for electric vehicles, the United States is expected to be unable to keep up with demands for energy dense materials, such as lithium, as early as 2030. Currently, the United States relies on overseas countries to source their lithium, where environmentally unfriendly practices are utilized to extract the metal. Eyes have turned towards the Salton Sea, California, as it possesses large, untapped quantities of lithium in underground pools. Existing geothermal plants in the region pumps brine to the surface which is later sent back into the ground after the power cycle to generate electricity for the local area. Capturing lithium from geothermal brines can be profitable and alleviate projected lithium shortages.

This Capstone thesis focuses on a process that can generate clean and renewable energy while extracting and producing lithium hydroxide monohydrate ($LiOH•H_2O$); with existing infrastructure located in the Salton Sea region of California, this process can be readily retrofitted after the geothermal power cycle. Extraction of lithium is done using a novel redox intercalation process which selectively captures lithium ions over similarly charged cations found in the geothermal brines. By using electrolysis in tandem with the capture process, the deintercalation material can be continuously regenerated, significantly reducing feedstock costs. With an input of 6,000 gallons per minute of geothermal brine, this process can produce a net power output of 25.5 MW and 7,701 tonnes per year of $LiOH•H_2O$, producing $474 million annually. Economic analysis of the process over a period of 20 years reveals an internal rate of return of 175%. Despite the process' favorable economics, we selected the *no go* decision due to the cost of calcium citrate and other unknowns associated with the process. We determined that the process may be economically viable if further studies are performed to better understand the lithium capture process.

1. INTRODUCTION

Green transportation, such as electric vehicles (EVs), have garnered increased attention as fossil fuels continue to contribute to climate change. These EVs rely on rechargeable batteries, requiring the use of large quantities of energy dense materials such as lithium. Currently, the United States sources a majority of its lithium from Chile and Argentina (Warren, 2021). However, current lithium supply cannot meet projected demands (Ambrose et al., 2020). New large-scale and domestic sources of lithium will be needed to meet rapidly increasing demand.

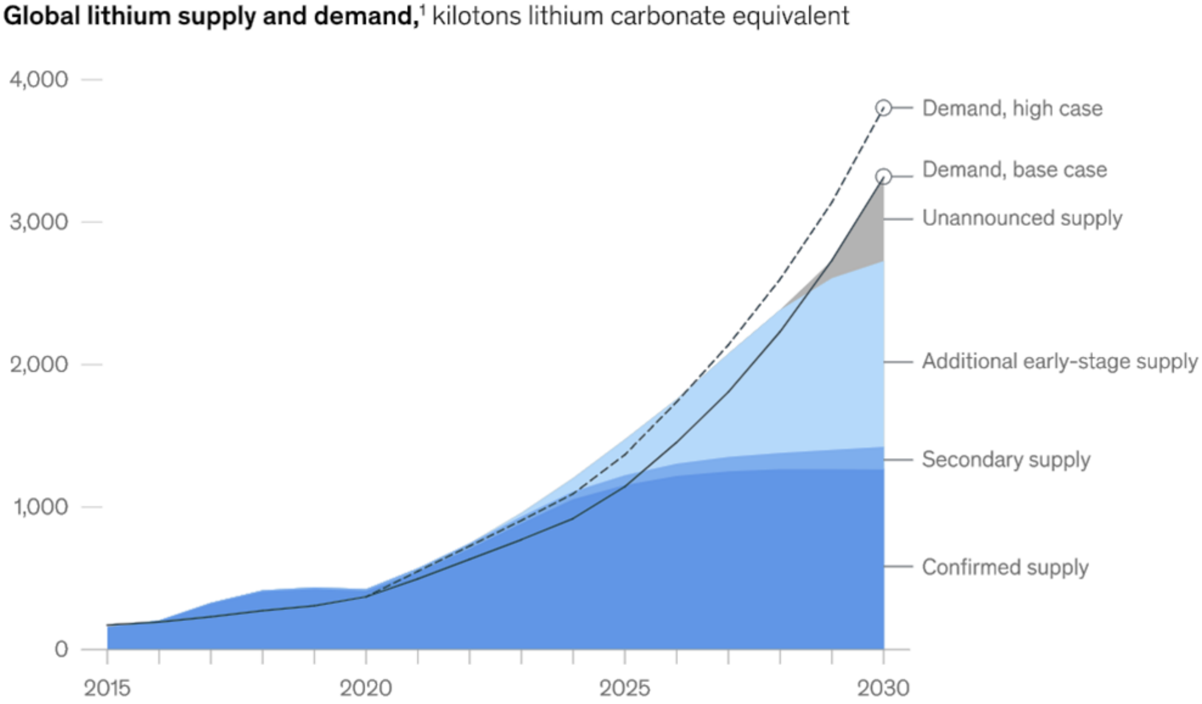

Figure 1.1: *Projected Lithium Supply and Demand (Azevedo et al., 2022)*

Superheated brines located beneath the Earth's crust have attracted interest as potential green energy sources. These brines are pumped to the surface in many areas to generate geothermal energy. Some of these geothermal brines contain relatively high concentrations of lithium and are attractive options for lithium extraction operations. Currently, lithium is collected from brines using a technique known as evaporative extraction, a resource-intensive and environmentally unfriendly process (Warren, 2021). Different techniques must be utilized to sustainably produce lithium from geothermal brines. Existing power plants drawing from geothermal seas take in thousands of gallons of hot brine every minute. Even at low concentrations, a single well could potentially produce thousands of tons of lithium each year if it can be separated and purified. Here, we propose a design of a lithium extraction plant that can be retrofitted to a geothermal brine power plant in the Salton Sea, California. After heated brine passes through the plant, it is usually injected back into the geothermal well. Our process could be implemented after brine completes the power cycle but before reinjection. We aim to create a design that offers a domestic, economical, and environmentally conscious method of increasing the production of battery grade lithium hydroxide.

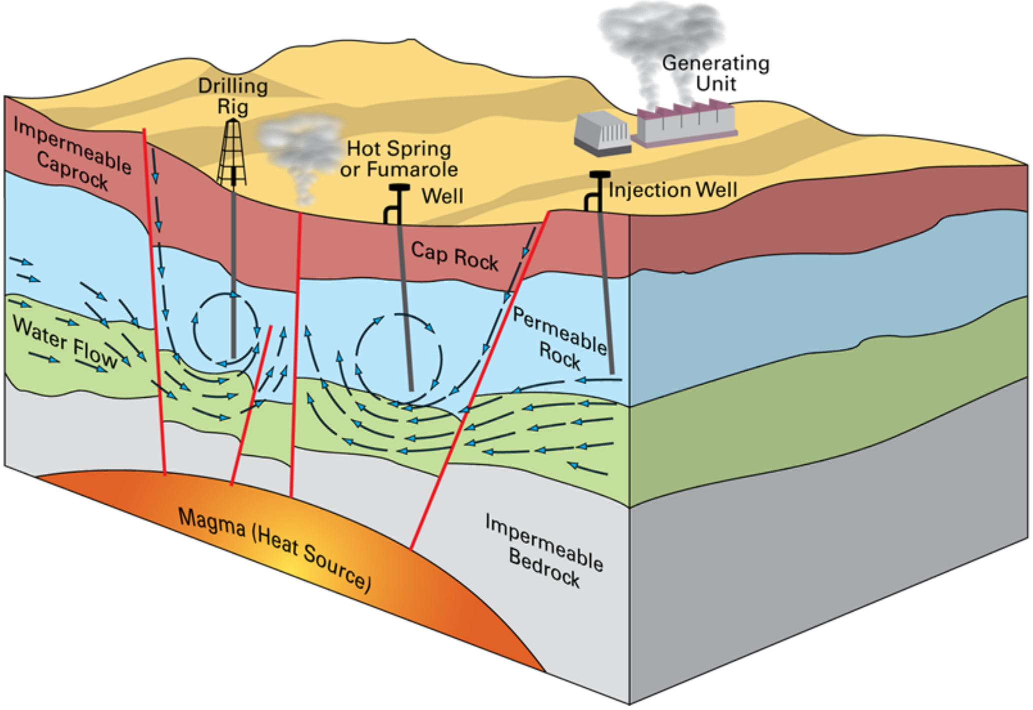

Figure 1.2: *Geothermal Power Plant (Geothermal Energy, n.d.)*

2. PREVIOUS WORK

It is estimated that the United States imports 90% of its lithium from overseas, where current technologies used to extract a majority of the world's lithium supply include hardrock mining and evaporative extraction techniques. These technologies are both energy and resource intensive. During evaporative extraction, lithium-rich solution is pumped from underground into large ponds and allowed to sit for a span of 18 to 24 months. Slaked lime is introduced to the highly concentrated solution, which then passes through multiple purification steps to produce lithium carbonate (Li_2CO_3) or lithium hydroxide monohydrate ($LiOH \cdot H_2O$) as final products (Warren, 2021). This process typically takes place in desert areas, where already strained water resources are depleted further by mining. The process proposed in this project seeks to develop a domestic, environmentally conscious solution to meet the growing need for lithium.

The designs detailed in this project are based on the work of chemical engineering professors Geoffrey Geise, Gaurav Giri, and Gary Koenig at the University of Virginia. These professors, along with industry partner PowerTech water, are competing for the Department of Energy American-Made Geothermal Lithium Extraction Prize, valued up to $2,000,000 (McManamay, 2022). Together, they make up team TELEPORT, which stands for Targeted Extraction of Lithium with Electroactive Particles for Recovery Technology. Team TELEPORT has proposed a process for extracting lithium utilizing iron (III) phosphate as a redox capture material. Using iron chloride, the redox state of the iron phosphate crystals can be controlled to either capture or release lithium. The advantage of this process is the recyclability of iron chloride through an electrodialysis process, significantly reducing the cost of extraction. This process design aims to test the viability of proposed technologies made by team TELEPORT at a scale that enables extraction of lithium from geothermal brine at a single well in the Salton Sea.

3. DISCUSSION

3.0 BRINE MODELING

Brine was modeled in Aspen Plus v11 software using the Electrolyte-NRTL (ELECNRTL) method. This non-random, two-liquid model was selected because it is best suited to simulate non-ideal solutions such as the high temperature and pressure geothermal brine in the system. Brine in the Salton Sea contains a vast array of dissolved salts; to simplify analysis, the most prevalent components were considered including water (H_2O), lithium ions (Li^+), sodium ions (Na^+), potassium ions (K^+), calcium ions (Ca^{2+}), manganese ions (Mn^{2+}), iron ions (Fe^{2+}), chloride ions (Cl^-), and silicates (SiO_2) (Warren, 2021).

Table 3.0.1

Selected components of geothermal brine for Aspen 11 Simulations

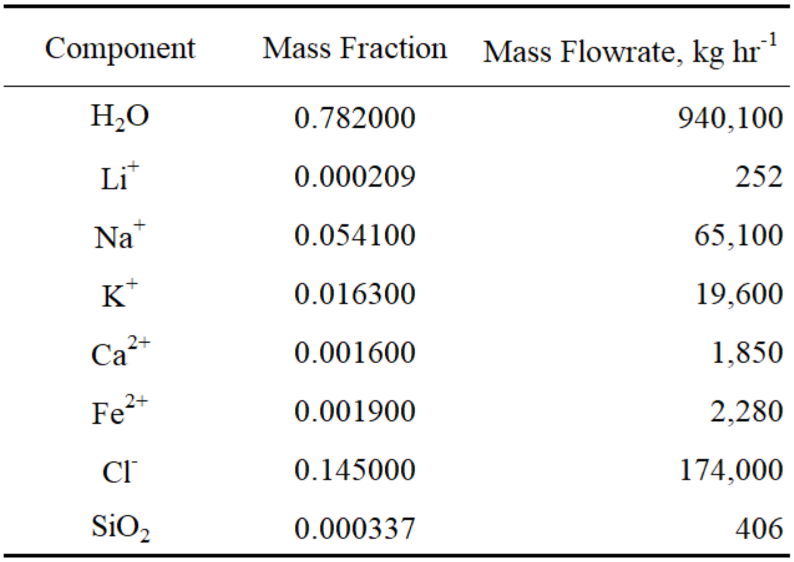

Component	Mass Fraction	Mass Flowrate, kg hr^{-1}
H_2O	0.782000	940,100
Li^+	0.000209	252
Na^+	0.054100	65,100
K^+	0.016300	19,600
Ca^{2+}	0.001600	1,850
Fe^{2+}	0.001900	2,280
Cl^-	0.145000	174,000
SiO_2	0.000337	406

The overall process is illustrated in Figure 3.0.1 presented on the following page.

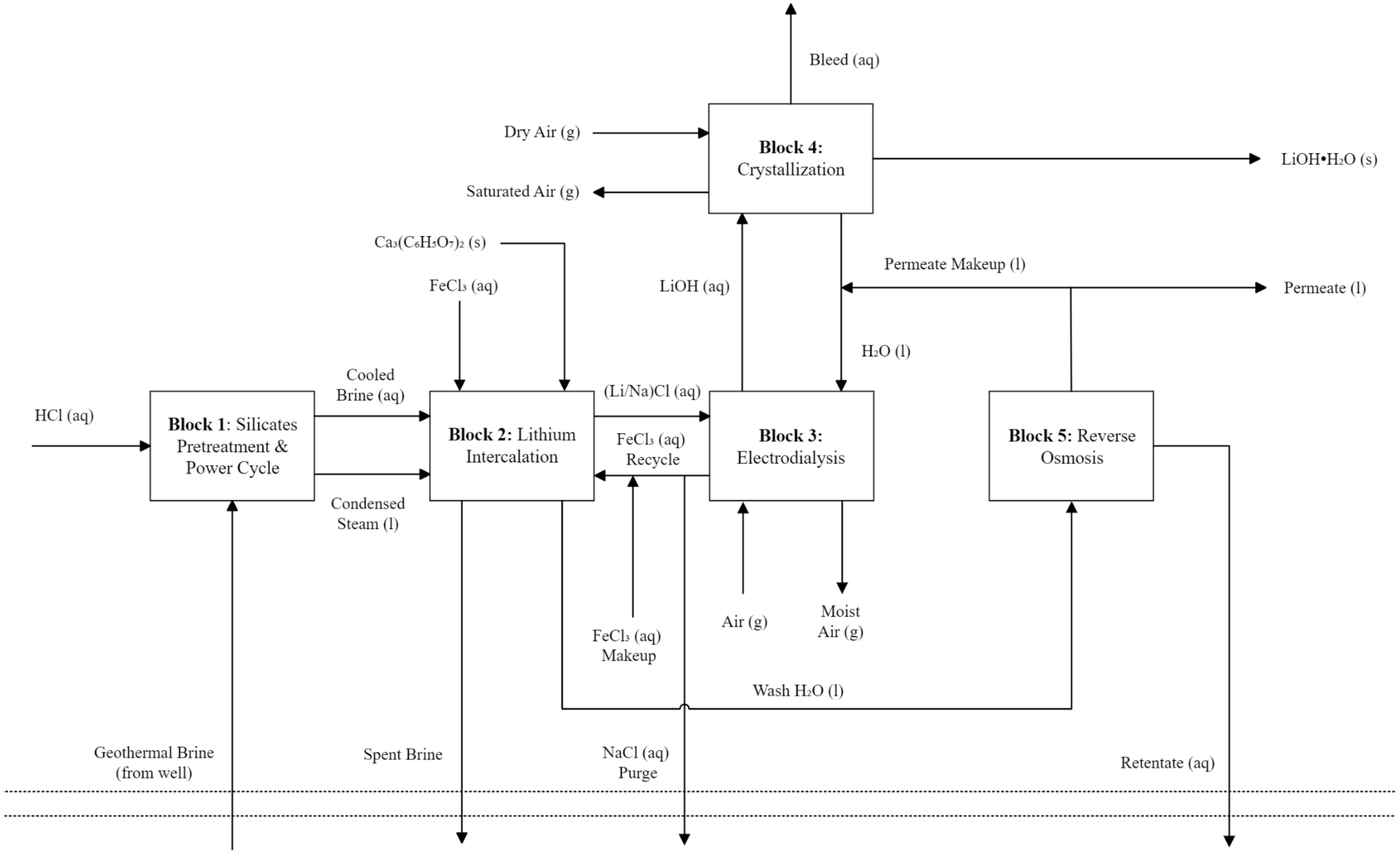

Figure 3.0.1: *Block Flow Diagram of Geothermal Power Generation & Lithium Ion Intercalation Plant*

3.1 SILICATE TREATMENT

Brine from the Salton Sea contains an average of 390 ppm of dissolved silicates (Warren, 2021). Silicates present in these brines are known to cause fouling in piping. This significantly reduces the efficiency of the power generation cycle and could impede the flow of brine with silicate deposits building up over time. Silicate scaling can be controlled by altering the pH of brines. At low pH values, silicates are significantly less likely to polymerize and thus cause fouling (Guerra & Jacobo, 2012).

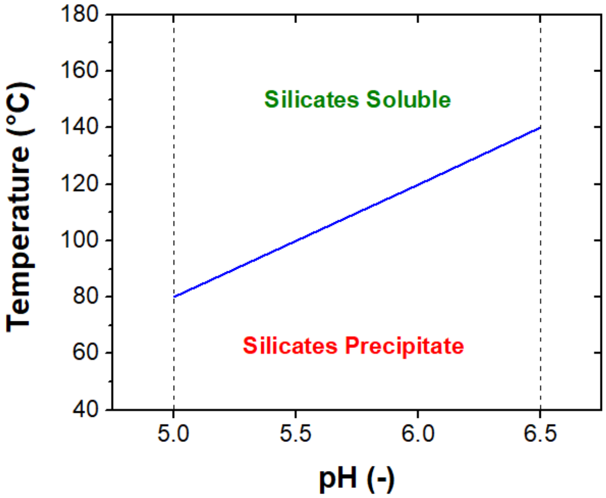

Figure 3.1.1: *Silicate Solubility Temperature at Various pH Values*

Raw brine pumped out of the ground enters the process at 275°C, 60 bar, density of 912 kg m^{-3}, and pH of 6.7. To adjust pH of the incoming brine, pressurized 9.6M hydrochloric acid (HCl) solution at 25℃ will be added to the inlet brine stream to reach an initial pH of 2.36. Current infrastructure in the Salton Sea pumps brine to the surface at a rate of 6,000 gal min^{-1} or 1,240,000 kg hr^{-1} (Ventura et al., 2016). To reach the desired pH of 2.2 leaving the power cycle, HCl solution must be added at 2,500 kg hr^{-1}. As flow through the tubing is turbulent, HCl solution can be injected directly into the brine feed and assumed to be well mixed after flowing over a length of 10 pipe diameters (Anderson, personal communication, January 2023). No additional process units are required to mix the HCl solution with brine.

3.2 STEAM GENERATION FOR POWER CYCLE

Infrastructure in the Salton Sea already exists to generate steam and thus power. We selected to complete this exercise to study power generation and silicate pretreatment steps in detail while also estimating water generation rates for future process steps. Knowing this, we gained an understanding of how much water and energy we could purchase from the geothermal power plant.

After pH is adjusted, the brine is flashed to generate steam for the power cycle. This step also concentrates the ions present in the brine. Flashing is a single stage vaporization process that involves rapidly reducing the pressure of a saturated liquid. Solubility curves for the salts generated through the Electrolyte Wizard in the ELECNRTL method in Aspen were modeled in order to confirm that no salts precipitated out during the flash process. Three flash vessels will be used to create 40 bar, 20 bar, and 1.1 bar steam to prepare the brine for the lithium capture step. All three flash vessels will be constructed of Monel 400 to withstand the highly corrosive brine.

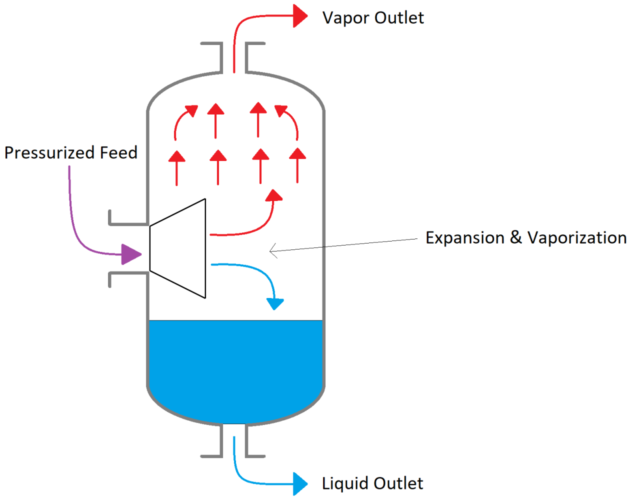

Figure 3.2.1: *Diagram of a Flash Vessel*

Flash drums were modeled using the Flash2 block in Aspen Plus v11. A pressure change of 20 bar was used for the first two drums while a 18.9 bar pressure drop was used for the third. The diameter of the flash drums were calculated in two ways. First, the minimum volume of the tank was determined based on the incoming brine volume and the mean residence time in the tank. Typically, for a flash vessel with product feeding to another tower, the holdup time ranges between 5 to 10 minutes, and a liquid level at half the height of the tank is assumed (Turton, 2018). A holdup time of 7.5 min was used in this calculation.

$$V = 2 \times \frac{Feed * mean\ residence\ time}{density\ of\ brine} \tag{E 3.2.1}$$

Knowing the required volume, V, based on the stream, the minimum diameter, D_{tank}, was calculated with an optimal L/D ratio of 3 (Turton, 2018).

$$D_{tank} = \sqrt[3]{\frac{2V}{3\pi}} \tag{E 3.2.2}$$

Using the first method, the drum volumes for 40 bar, 20 bar, and 1.1 bar flash vessels were estimated to be 342 m^3, 288 m^3, and 240 m^3 respectively. This corresponds to a diameter of 4.17 m for the 40 bar vessel, 3.94 m for the 20 bar vessel, and 3.71 m for the 1.1 bar vessel.

In the second calculation, diameter was computed based on the permissible velocity, μ, above which liquids are entrained in the gas stream. This is highly undesirable as it can cause damage to equipment in the power cycle (Turton, 2018).

$$\mu = K\sqrt{\frac{\rho_L - \rho_V}{\rho_V}} \tag{E 3.2.3}$$

The permissible velocity is dependent on the density of the liquid, ρ_L, and the density of the vapor, ρ_V. It is also dependent on *K*, a constant determined using the following two correlations:

$$K = e^{-1.877 - 0.814 lnF_{lv} - 0.187(lnF_{lv})^2 - 0.0145(lnF_{lv})^3 - 0.00102(lnF_{lv})^4} \qquad \text{(E 3.2.4)}$$

$$F_{lv} = \frac{\dot{m}_L}{\dot{m}_V}\sqrt{\frac{\rho_V}{\rho_L}} \qquad \text{(E 3.2.5)}$$

In Equation 3.2.5, $\dot{m}_L$ and $\dot{m}_V$ represent liquid and vapor mass flow rates respectively. Based on modeled mass flow rates of gas and liquid stream along with their densities, minimum cross-sectional area, *A*, and diameter were determined.

$$A = \frac{\dot{m}_V}{\rho_V \times \mu} \qquad \text{(E 3.2.6)}$$

$$D = \sqrt{\frac{4A}{\pi}} \qquad \text{(E 3.2.7)}$$

Using the second calculation technique, the 40 bar, 20 bar, and 1.1 bar tank diameters were estimated to be 1.63 m, 1.47 m, and 1.54 m respectively.

The larger of the two diameter values were chosen for the actual sizing of the flash drums to provide the most conservative estimate, from which the final volumes were calculated. The 40 bar, 20 bar, and 1.1 bar vessels have diameters of 4.17 m, 3.94 m, and 3.71 m respectively, corresponding to tank volumes of 342 m^3, 288 m^3, and 241 m^3.

Flash Vessel Design

The design of the first flash is detailed in Table 3.2.3.

Table 3.2.3

Design of High Pressure Flash Vessel for Steam Generation

Parameter	Value
Temperature	264°C
Pressure	40 bar
Vapor Fraction	0.13
Diameter	4.17 m
Length	12.5 m
Volume	342 m^3
Material of Construction	Monel-400

The design of the second flash is detailed in Table 3.2.4.

Table 3.2.4

Design of Intermediate Pressure Flash Vessel for Steam Generation

Parameter	Value
Temperature	226°C
Pressure	20 bar
Vapor Fraction	0.1
Diameter	3.94 m
Length	11.8 m
Volume	288 m^3
Material of Construction	Monel-400

The design of the third flash is detailed in *Table 3.2.5*.

Table 3.2.5
Design of Low Pressure Flash Vessel for Steam Generation

Parameter	Value
Temperature	110°C
Pressure	1.10 bar
Vapor Fraction	0.05
Diameter	3.71 m
Length	11.1 m
Volume	241 m^3
Material of Construction	Monel-400

Steam from the 40 bar vessel and 20 bar section is then fed to separate turbines for power generation. The 40 bar vessel is expected to produce 144,000 kg hr^{-1} of steam, and the 20 bar vessel will create 96,400 kg hr^{-1}. Turbines were modeled in Aspen using the COMPR block to estimate power generation capabilities. The 40 and 20 bar steam are expected to produce 19 MW and 10 MW respectively; a total of 29 MW of power is generated at a brine flow rate of 6,000 gallons per minute. All power generation equipment should be made from acid resistant materials due to trace HCl present in the steam from the silicate removal step. After the power generation, steam is condensed used to wash the lithium intercalation reactors.

The low pressure vessel is estimated to produce 44,000 kg hr^{-1} of 1.1 bar steam. This steam is too low in pressure to produce energy but will be condensed in the lithium intercalation block to wash the lithium intercalation reactors. Brine leaving the 1.1 bar drum at a flow rate of 968,000 kg hr^{-1} then flows to the lithium intercalation reactors for further processing.

Auxiliary Equipment Sizing and Operating Conditions

There are two pumps used to pump geothermal brine and HCl feed to the system at 60 bar. The power requirement calculation assumed the pump efficiency to be 80% and using Eq. 3.2.8:

$$P = \frac{\dot{m}\,\Delta h}{\eta\rho} \tag{E 3.2.8}$$

where P is hydraulic power requirement in W, $\dot{m}$ is mass flow rate of the stream in kg s^{-1}, Δh is pressure difference in pascal, η is pump efficiency, and ρ is the density of the stream in kg m^{-3}, the two power requirements are calculated at 2.78 MW and 4.5 kW.

Prior to flowing the brine to the lithium intercalation reactors, the brine is first passed through a heat exchanger to lower the temperature to the operating temperature of 80 ^{o}C.

The heat exchanger is a countercurrent shell and tube heat exchanger modeled using Aspen Plus with a MHeatX block. The heat transfer area of the heat exchanger can be determined using Eq. 3.2.9:

$$Q = UA_o \Delta T_{lm} F(S, R) \tag{E 3.2.9}$$

where Q is the total heat duty of the heat exchanger in W, U is the overall heat transfer coefficient of the heat exchanger in W m^{-2} K^{-1}, A_o is the total contact area between the cold and hot fluid in m^2, ΔT_{lm} is the logarithmic mean temperature difference between cold stream and hot stream in K, and $F(S, R)$is the correction factor for shell and tube heat exchanger (Carta, 2021). Q is either obtained through Aspen simulation or calculated using the Eq 3.2.10:

$$Q = m_x C_{p,x}(T_{x,out} - T_{x,in}) \tag{E 3.2.10}$$

where Q is total heat duty in kJ hr^{-1}, m_x is mass flow of either hot or cold stream in kg hr^{-1}, $C_{p,x}$ is heat capacity of the stream in kJ kg^{-1} K^{-1} , and T is the temperature of the stream in Kelvin. The log mean temperature difference is the driving force for temperature in flow systems, which is calculated through Eq. 3.2.11:

$$\Delta T_{lm} = \frac{(T_h^{in} - T_c^{out}) - (T_h^{out} - T_c^{in})}{ln\frac{T_h^{in} - T_c^{out}}{T_h^{out} - T_c^{in}}} \qquad \text{(E 3.2.11)}$$

where T_h^{in} and T_h^{out} are temperatures of inlet and outlet hot streams in Kelvin and T_c^{in} and T_c^{out} are temperatures of inlet and outlet cold streams in Kelvin. The correction factor, $F(S, R)$, is obtained using a correlation in (Carta, 2021) along with Eq. 3.2.12 and 3.2.13:

$$S = \frac{T_{tube,out} - T_{tube,in}}{T_{shell,in} - T_{tube,in}} \qquad \text{(E 3.2.12)}$$

$$R = \frac{T_{shell,in} - T_{shell,out}}{T_{tube,out} - T_{tube,in}} \qquad \text{(E 3.2.13)}$$

The overall heat transfer coefficient is estimated for shell and tube heat exchanger with brine and water to be around 900 W m^{-2} K^{-1} according to (Perry et al., 2007), which can be accounted for by the fouling coefficient through Eq. 3.2.14.

$$U_{o,d} = \left(\frac{1}{U_o} + \frac{1}{h_{d,i}}\frac{r_o}{r_i} + \frac{1}{h_{d,o}}\right)^{-1} \qquad \text{(E 3.2.14)}$$

where $U_{o,d}$ is the overall heat transfer coefficient accounted for fouling expressed in W m^{-2} K^{-1}, U_o is the overall heat transfer coefficient without fouling in W m^{-2} K^{-1}, $h_{d,i}$ is tube side fouling coefficient in W m^{-2} K^{-1}, $h_{d,o}$ is shell side foundling coefficient in W m^{-2}K^{-1}, r_o is outer radius of the pipe in m, and r_i is the inner radius of the pipe in m. Assuming the pipe is thin enough, the inner radius is equal to the outer radius. We assumed 4000 W m^{-2} K^{-1} for both fouling coefficient terms, so using Eq 3.2.14, the corrected overall heat transfer coefficient is 562.5 W m^{-2} K^{-1} (Carta, 2021).

Using Eq. 3.2.9~3.2.14, total heat transfer area is calculated to be 772 m^2, which is constructed out of Monel to withstand corrosion from HCl in the brine. According to heuristics, the typical radius of heat exchanger pipes are 0.025 m and typical length of these pipes are 7.32 m (Peters et al., 2003). The total number of pipes, N_{total}, is determined through Eq. 3.2.15:

$$A_o = 2\pi r_o L N_{total} \tag{E 3.2.15}$$

where A_o is heat transfer area in m^2, r_o is outside radius of the pipe, and L is the length of the pipe. Using this equation, the total number of pipes for the heat exchanger in the power cycle is 672. The heat exchanger uses water coming in at 30 ºC and exiting at 45 ºC to cool off the brine and the flow rate of this water stream is 1,393,871 kg hr^{-1}. Per heuristics, typical pressure drop in the heat exchanger is 0.4 bar, so the brine stream leaving the power cycle will exit at 0.7 bar (Peters et al., 2003).

3.3 LITHIUM ION INTERCALATION

Selective Capture of Lithium Ions

After passing through the geothermal plant to generate steam, the liquid brine is then fed to the lithium ion intercalation reactor. Brine flows into the reactor process block at a rate of 968,000 kg hr^{-1}. The reactor is filled with iron (III) phosphate ($FePO_4$), which acts as an intercalation material.

$$Fe^{2+}{}_{(aq)} + FePO_{4\,(s)} + Li^{+}{}_{(aq)} = LiFePO_{4\,(s)} + Fe^{3+}{}_{(aq)} \qquad \text{(R 3.3.1)}$$

Iron 2+ ions present in the brine solution reduce $FePO_4$ to $FePO_4^-$. To lower redox potentials, an oxidizing agent must also be added to the incoming brine. Studies have only been performed using citrate; calcium citrate ($Ca_3(C_6H_5O_7)_2$) was selected by Team TELEPORT as an oxidizing agent to promote favorable intercalation thermodynamics. Despite its known low solubility, calcium citrate was assumed to dissolve upon addition to the brine stream without the use of a mixing tank. The negative charge of $FePO_4^-$ allows the Li^+ "guest" ion to intercalate into interstitial spaces within its crystalline structure as other cations are rejected based on size and charge (Gupta et al., 2022). It is also possible for Na^+ ions to intercalate into the bed with a selectivity $[Na^+]/[Li^+]$ between species of 0.0082.

After the bed has reached the desired saturation level, the raw brine feed is cut off to begin the regeneration process. After washing with steam condensed from power generation, 500mM $FeCl_3$ solution is fed to the reactor to deintercalate Li^+ from $LiFePO_4$.

$$FeCl_{3\,(aq)} + LiFePO_{4\,(s)} = FePO_{4\,(s)} + FeCl_{2\,(aq)} + LiCl_{(aq)} \qquad \text{(R 3.3.2)}$$

The regeneration process recovers the $FePO_4$ intercalation material, and the aqueous solution of $FeCl_2$ and LiCl is sent to the electrodialysis unit for further processing and recovery.

Reactor Modeling

The intercalation reactors were modeled as packed bed reactors (PBR). PBRs are a type of reactor in which solid particles, typically a catalyst or an adsorbent, are packed into tubes which reactant fluid passes through.

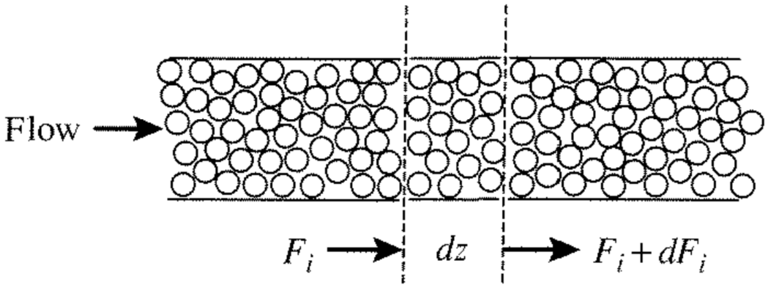

Figure 3.3.1: *Diagram of a Packed Bed Reactor with a differential volume element (Davis, 2003)*

The equations are derived from Arim et al. (2018) and adjusted for the competitive intercalation of Li^+ and Na^+. Performing a differential material balance on a reactor volume element yields:

$$\frac{\partial C_i}{\partial t} = -\frac{u_0}{\varepsilon}\frac{\partial C_i}{\partial z} - \rho_s(1-\varepsilon)\frac{\partial W_i}{\partial t} + D_{ax}\frac{\partial^2 C_i}{\partial z^2} \qquad \text{(E 3.3.1)}$$

Where C_i is the concentration of component i in the fluid in mol m^{-3} ($i = L$ for Li^+ and N for Na^+), W_i is the concentration of component i that is intercalated in $FePO_4$ in mol kg^{-1}, u_0 is the superficial velocity of the fluid flowing through the reactor in m s^{-1}, ε is the void fraction of the bed, equal to 0.6, ρ_s is the density of $FePO_4$, equal to 3,056 kg m^{-3}, and D_{ax} is the axial dispersion coefficient in m^2 s^{-1}.

Each term in the equation has a specific role in the material balance. First, $\frac{\partial C_i}{\partial t}$ accounts for the accumulation of material in the bed, as this process does not reach steady state. The

$\frac{-u_0}{\varepsilon}\frac{\partial C_i}{\partial z}$ term accounts for the in/out flow for the volume element. Potential variations in the superficial velocity are ignored, thus u_0 is treated as a constant. The $-\rho_s(1-\varepsilon)\frac{\partial W_i}{\partial t}$ term addresses the material that is leaving the fluid and being intercalated in the $FePO_4$. Finally, $D_{ax}\frac{\partial^2 C_i}{\partial z^2}$ accounts for axial dispersion of material that becomes significant due to highly laminar flow in the reactor. The axial dispersion coefficient was calculated using a correlation with the Reynolds number (Re):

$$D_{ax} = u_0 d_s(0.11Re^{0.4} + 0.2)^{-1} \tag{E 3.3.2}$$

$$Re = \frac{u_0 d_s \rho_f}{\mu_f} \tag{E 3.3.3}$$

Where d_s is the radius of the $FePO_4$ particles, equal to 0.002 m, ρ_f is the density of the brine flowing through the bed, equal to 1,080 kg m^{-3}, and μ_f is the dynamic viscosity of the brine flowing through the bed, equal to 0.0019 Pa-s. Our models resulted in Reynolds number between 6 and 12, which is characteristic of highly laminar flow.

The rate at which Li^+ and Na^+ intercalate is treated as a mass-transfer limited process modeled as:

$$\frac{\partial W_i}{\partial t} = k_{LDF,i}(W_{i,eq} - W_i) \tag{E 3.3.4}$$

Where $k_{LDF,i}$ is the linear driving force coefficient for component i in s^{-1} and $W_{i,eq}$ is the equilibrium concentration of component i intercalated in $FePO_4$ in mol kg^{-1}, corresponding to the surrounding concentration C_i.

$W_{i,\,eq}$ is modeled using a competitive Langmuir isotherm for two components:

$$W_{L,\,eq} = W_{sat}\frac{K_{eq,L}C_L}{1+K_{eq,L}C_L+K_{eq,N}C_N} \qquad \text{(E 3.3.5)}$$

$$W_{N,\,eq} = W_{sat}\frac{K_{eq,N}C_N}{1+K_{eq,L}C_L+K_{eq,N}C_N} \qquad \text{(E 3.3.6)}$$

Where W_{sat} is the saturation concentration of ions intercalated in $FePO_4$ in mol kg^{-1} and $K_{eq,\,i}$ is the equilibrium constant for the intercalation of component i in m^3 mol^{-1}. Assuming a maximum molar ratio of 1:1 intercalated ions to moles of $FePO_4$, W_{sat} would be 6.65 mol kg^{-1}. The linear driving force coefficient is calculated as:

$$k_{LDF,\,i} = \frac{2\Omega D_{eff.\,i}}{\rho_s d_s\left(\frac{\partial W_{i,\,eq}}{\partial C_i}\right)} \qquad \text{(E 3.3.7)}$$

Where Ω is the linear driving force parameter, equal to 15 for spherical particles, $D_{eff,\,i}$ is the effective diffusivity of component i in m^2 s^{-1}, and $\frac{\partial W_{i,\,eq}}{\partial C_i}$ is the derivative of component i equilibrium isotherm with respect to the concentration of component i in the fluid. Effective diffusivity was calculated based on several equations from Carta (2021):

$$D_{eff.\,i} = \frac{\phi}{\tau}D_{pore,i} \qquad \text{(E 3.3.8)}$$

$$D_{pore.\,i} = \left(\frac{1}{D_{k,i}} + \frac{1}{D_{H2O,\,i}}\right)^{-1} \qquad \text{(E 3.3.9)}$$

$$D_{k,i} = 4.85 * 10^{-8}(d_{pore})\left(\frac{T}{M_{w,\,i}}\right)^{0.5} \qquad \text{(E 3.3.10)}$$

Where $D_{k,\ i}$ is the Knudsen diffusivity of component *i*, $D_{H2O,\ i}$ is the diffusivity of component *i* in water, $D_{H2O,\ pore}$ is the diffusivity of component *i* in the pores of $FePO_4$, *d* is the diameter of the pores, assumed to be 500 nm, Φ is the porosity of the $FePO_4$ particles, equal to 0.5, τ is the tortuosity of the $FePO_4$ particles, assumed to be 4, *T* is the operating temperature of the reactor in kelvin, and $M_{w,\ i}$ is the molecular weight of component *i* in g mol^{-1}.

Langmuir equilibrium constants were estimated based on the standard reduction potential of the two half reactions of the total Li^+ intercalation reaction. The two half reactions occurring are the oxidation of Fe^{2+} in the brine and the reduction of Fe^{3+} in the $FePO_4$.

$$Fe^{2+} = Fe^{3+} + e^- \qquad \text{(R 3.3.3)}$$

$$Li^+ + e^- + Fe^{3+}PO_4 = LiFe^{2+}PO_4 \qquad \text{(R 3.3.4)}$$

The standard cell potential, E^o_{cell}, can be calculated as the difference between the standard reduction potential (SRP) of the reduction reaction (E^o_{red}) and the SRP of the oxidation reaction, E^o_{ox}. The temperature adjusted cell potential can then be calculated using the Nernst equation:

$$E^o_{cell} = E^o_{red} - E^o_{ox} \qquad \text{(E 3.3.11)}$$

$$E_{cell} = E^o_{cell} - \frac{RT}{nF} ln(\frac{[Fe^{3+}]}{[Fe^{2+}]}) \qquad \text{(E 3.3.12)}$$

Where *n* is the number of electrons transferred in the redox reaction (equal to 1), *F* is Faraday's constant, *R* is the ideal gas constant, and $\frac{[Fe^{3+}]}{[Fe^{2+}]}$ is the ratio of Fe^{3+} to Fe^{2+} ions in solution, which is assumed to be 1:99.

Once the temperature adjusted cell potential is calculated, the Gibbs free energy change of the redox reaction, ΔG, can be calculated:

$$\Delta G = - nFE_{cell} \tag{E 3.3.13}$$

From the Gibbs free energy change, the equilibrium constant of the reaction can be calculated:

$$K_{eq,\,L} = exp(\frac{-\Delta G}{RT}) \tag{E 3.3.14}$$

In order for the reaction to be thermodynamically favorable, ΔG must be negative, therefore E^o_{cell} must be positive. Under normal experimental conditions, the SRP of Fe^{2+} to Fe^{3+}oxidation is 0.77 V, while the SRP of $Fe^{3+}PO_4$ to $LiFe^{2+}PO_4$ is 0.41 V. This would lead to a standard cell potential of -0.36 V, which is not thermodynamically favorable. The presence of citrate ions, which is accomplished by adding calcium citrate, lowers the SRP of Fe^{2+} to Fe^{3+}oxidation to 0.244 V, leading to a standard cell potential of 0.166 V. After applying the Nernst equation and calculating ΔG, $K_{eq,\,L}$ comes out to 23,210.

Lastly, the Langmuir equilibrium constant for Na^+ was estimated based on selectivity data provided by Gupta et al. The selectivity, S, equal to 0.0082, is the ratio of Na^+ to Li^+ intercalated into $FePO_4$ particles from a solution of 1:1 Li^+ to Na^+:

$$K_{eq,\,N} = \frac{S}{1-S} K_{eq,\,L} \tag{E 3.3.15}$$

For this model, we assumed that the reactor would behave isothermally. In reality, the reactor would experience temperature change as the intercalation reaction is exothermic. However, this temperature change is likely to be minor since the amount of lithium and sodium ions capture is relatively small compared to the amount of water in the reactors, which is the primary component that would affect the system's heat capacity. More importantly, the regeneration reaction is the reverse reaction of the intercalation reaction, thus it would be endothermic and absorb heat from the system, lowering the temperature. It is unknown how the presence of citrate ions could effect the symmetry of the heat of reaction for the forward and reverse reactions; therefore, it was assumed that the symmetry would be retained and any heat released during capture would be canceled out during release.

In total, we have a system of four partial differential equations, including the material balance equations and mass transfer equations for both Li^+ and Na^+. The system was solved numerically using a finite difference method to transform the system of partial differential equations into a system of ordinary differential equations. MATLAB's ode45 function, which implements an explicit Runge-Kutta formula, was used to solve the equations. The reactor was modeled as a single large vessel containing several smaller tubes of standard diameters. The program took inputs of reactor length (L), tube diameter (d_t), superficial velocity, and total volumetric flow rate to the reactor (V_{tot}). The number of tubes needed was calculated as:

$$n_{tubes} = \frac{4V_{tot}}{\pi u_0 d_t^2} \qquad \text{(E 3.3.16)}$$

Using a guess-and-check method, several different input conditions were tested to see what conditions maximize both recovery of lithium and saturation of the bed. The modified Ergun equation was used to calculate the pressure drop (0.0015 bar) across the reactor (Davis, 2003):

$$\Delta P = L\left(\frac{1-\varepsilon}{\varepsilon^3}\right)\left(1 + \frac{2d_s}{3(1-\varepsilon)d_t}\right)^2\left(\frac{1.75}{1+\frac{2d_s}{3(1-\varepsilon)d_t}} + 150\frac{1-\varepsilon}{Re}\right) \qquad \text{(E 3.3.17)}$$

It is important to note that this model is intended as a first-pass analysis of the potential behavior of the system. Improvements can be made to make the model more accurate, but were unable to be implemented due to the increased complexity they would introduce. For example, in reference to the lithium intercalation reactor, Gupta et al. speculates that “the heterogeneous reaction in the PBR [packed-bed reactor] follows a shrinking core process with regards to the LFP [lithium iron (III) phosphate] aggregate particle” (2022). According to Fogler (1986), shrinking core processes describe the change in size of solid catalyst/adsorbent particles due the material reacting to form a new material. This transient change in size has major effects on internal mass transfer effects by causing effective diffusivity of species to change due to shrinking or expanding pore sizes in the material. Because the $FePO_4$ intercalant is changing to $LiFePO_4$ during Li^+ capture, and back to $FePO_4$ during regeneration, it seems likely that this shrinking core effect would be occurring to some degree. There are mathematical models that are available from Fogler that could be used to simulate this effect, but implementing them with the rest of our model proved to be too complex and was considered outside the scope of this project.

Sizing and Operating Conditions

Although the selectivity of Li^+ intercalation vs. Na^+ intercalation is high, the concentration of Na^+ in the raw brine is much higher than that of Li^+. This results in a large amount of Na^+ being captured along with Li^+ after a single pass through the reactor. Therefore, two different types of reactors will be utilized. Primary reactors handle the intercalation of Li^+ from the brine coming from the silica pretreatment/power cycle, while secondary reactors will handle the intercalation of Li^+ ions from the stream coming from the primary reactor during regeneration. Primary reactors will operate at 80℃ and 1.1 bar to avoid silicate precipitation, which could negatively impact the efficiency of the column. Secondary reactors will operate at the same pressure, but at a temperature of 50℃ instead. An operating temperature of 50℃ was selected to meet the operating temperature requirement for the electrodialysis unit that follows.

The reactors will be constructed of high density polyethylene (HDPE) due to its corrosion resistant properties and low capital cost.

The reactors are designed similarly to a shell and tube heat exchanger, with several small diameter inner tubes. This design was selected in the event that heating/cooling was needed to keep the reactor isothermal; however, did this not end up being necessary. Both reactor types consist of a series of 4” inner diameter, 12 m long tubes. These tubes are filled with pelletized, 2 mm diameter $FePO_4$ spheres. The external void fraction of the bed is assumed to be 0.63, while the internal porosity is 0.5. A tortuosity of 4 was assumed. Primary reactors contain 2,715 tubes and have a superficial velocity within each tube of 1 cm s^{-1}, yielding a residence of time of 20 min. This reactor will require a total $FePO_4$ loading of 323 tonnes. Secondary reactors handle a smaller volumetric flow rate of brine compared to primary reactors, requiring only 835 internal tubes. The superficial velocity within the secondary reactor’s tubes is 0.572 cm s^{-1}, yielding a residence time of 35 min. This reactor will require a total $FePO_4$ loading of 90.5 tonnes and is estimated to capture 170 kg hr^{-1} of lithium ions. The design specifications of both reactors are summarized in Table 3.3.1.

Table 3.3.1

Reactor Operating Conditions & Design Specifications

Parameter	Primary Reactor Value	Secondary Reactor Value
Temperature	80°C	50°C
Pressure	1.1 bar	1.1 bar
Reactor Length	12 m	12 m
Tube Diameter	4 in.	4 in.
Number of Tubes	2715	835
Superficial Velocity	1.000 cm s^{-1}	0.572 cm s^{-1}
Residence Time	20 min	35 min
Loading of $FePO_4$	323 tonnes	90.5 tonnes
Li^+ Recovery	70%	96%
Saturation after 24 hrs	80%	99%
Tube Material	HDPE	HDPE

Cycling & Operation Schedule

Lithium intercalation reactors will be operated in four separate modes to isolate the lithium product: (1) primary capture/secondary regeneration, (2) initial wash, (3) primary regeneration/secondary capture, and (4) final wash.

In primary capture mode, raw brine is fed to the primary reactor at a rate of 968,000 kg hr^{-1} and temperature of 80℃, and Li^+ is captured by the $FePO_4$. The depleted brine is then pumped back down the geothermal well as waste at 81.5℃. This temperature increase is caused by the exothermic intercalation step. After a span of 23 hours and 50 minutes, brine feed will be cut off to the primary reactor. The primary bed is estimated to reach 80% total bed saturation (Li^+ and Na^+) and accomplish 70% Li^+ recovery during this cycle. Following the primary capture step, wash water will be fed to both the primary and secondary reactors for 10 minutes to wash away trace impurities that may reside in the beds. After the initial wash cycle, 500mM $FeCl_3$ solution will be fed to the primary reactor at a rate of 49,400 kg hr^{-1} and temperature of 50℃ to regenerate intercalated Li^+ and Na^+ ions, forming $FePO_4$ in the bed and producing $FeCl_2$, LiCl, and NaCl in the effluent.

Heats of reaction were estimated to provide an estimate of temperature change within the capture and release steps in the reactors using the standard enthalpy of formation:

$$\Delta_r H^{\theta} = \sum_{prod} v_i \, \Delta_f H^{\theta}_i - \sum_{rxt} v_i \Delta_f H^{\theta}_i \qquad \text{(E 3.3.18)}$$

where v_i is the stoichiometric coefficient on the reactant or product and $\Delta_f H^{\theta}_i$ is the standard enthalpy of formation of a component. Phan et al. provides the enthalpies of formations for the components reacting in the lithium intercalation reaction (R 3.4.4).

$$\Delta_f H^{\theta}_{LiFePO_4} = -1616\ kJ\ mol^{-1} \qquad \text{(E 3.3.19)}$$

$$\Delta_f H^{\theta}_{FePO_4} = -1279\ kJ\ mol^{-1} \qquad \text{(E 3.3.20)}$$

$$\Delta_f H^{\theta}_{Li^+} = -278.5\ kJ\ mol^{-1} \qquad \text{(E 3.3.21)}$$

Using E 3.3.18, the heat of reaction for lithium capture is -58.5 kJ mol^{-1}. As previously mentioned, sodium also competitively intercalates into $FePO_4$ through the following mechanism:

$$Na^+ + e^- + Fe^{3+}PO_4 = NaFe^{2+}PO_4 \qquad \text{(R 3.3.5)}$$

Xiao et al. presents the enthalpies of formations for these components in the competitive reaction:

$$\Delta_f H^{\theta}_{NaFePO_4} = -1571.8\ kJ\ mol^{-1} \tag{E 3.3.22}$$

$$\Delta_f H^{\theta}_{Na^+} = -239.7\ kJ\ mol^{-1} \tag{E 3.3.23}$$

Invoking E 3.3.18 provides a heat of reaction for sodium capture of -53.1 kJ mol^{-1}. For this project, it was assumed that the forward and reverse reactions released equal magnitudes of energy in opposite directions. Applying an energy balance around the reactor yields one unknown, the outlet temperature, which can be solved for.

The effluent leaves at 42.2℃ as the deintercalation step is endothermic. It was assumed that all of the captured ions are recovered, and $FeCl_3$ is completely converted into $FeCl_2$ as it is fed in 1:1 molar ratio to the $FeLiPO_4$. The first condition is based on the assumption that the intercalation and deintercalation steps are symmetric over time. The effluent from the primary reactor is then fed directly into its corresponding secondary reactor, along with calcium citrate, for secondary capture. This secondary capture step occurs simultaneously with primary regeneration.

Calcium citrate must be added to the secondary reactor at a rate of 13,700 kg hr^{-1}. The depleted brine from the secondary reactor is pumped back down the geothermal well as waste at 45℃. After a span of 23 hours and 50 minutes, $FeCl_3$ feed will be cut off to the primary reactor. The secondary bed is estimated to reach 99% total bed saturation, which is almost completely Li^+, with 96% Li^+ recovery in this near 24 hour cycle. Following the primary capture step, condensed steam from the power cycle will again be fed to both the primary and secondary reactors for 10 minutes to wash away trace impurities that may reside in the beds. After the secondary wash cycle, the brine feed is switched back on to reinitiate primary capture, while 500mM $FeCl_3$ solution is simultaneously fed to the secondary reactor to regenerate the secondary bed. The exiting stream will reach a temperature of 41.7℃. The effluent coming off of the secondary reactor during regeneration contains primarily $FeCl_2$ and LiCl, with trace amounts of NaCl. This stream is fed to the electrodialysis block to both recover $FeCl_3$, which is recycled for regeneration, and further process LiCl to LiOH.

In summary, the reactors will switch between capture and regeneration cycles, which will last 23 hours and 50 minutes, and at the end of each cycle all of the reactors will be washed for 10 minutes. During this short down time period for the reactors, the brine will simply circumvent the reactors and be reinjected back into the well. In total, two pairs of primary reactors and secondary reactors (4 total) are needed to ensure continuous operation for a total estimated Li^+ recovery of 67%. The operating schedule for the reactor system is summarized in Figure 3.3.1.

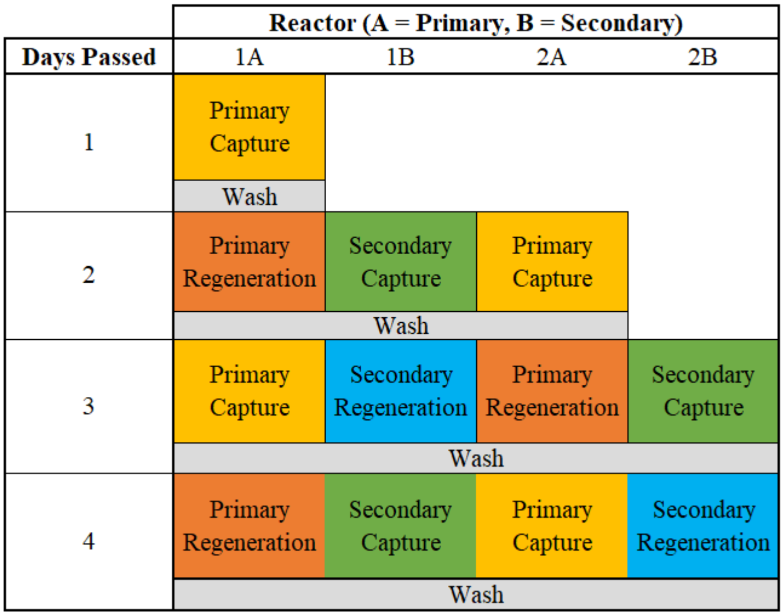

	Reactor (A = Primary, B = Secondary)			
Days Passed	1A	1B	2A	2B
1	Primary Capture			
	Wash			
2	Primary Regeneration	Secondary Capture	Primary Capture	
	Wash			
3	Primary Capture	Secondary Regeneration	Primary Regeneration	Secondary Capture
	Wash			
4	Primary Regeneration	Secondary Capture	Primary Capture	Secondary Regeneration
	Wash			

Fig. 3.3.1: *Lithium Intercalation Reactor System Schedule; Start-up to Steady Operation (capture & regeneration cycles are 23 hrs and 50 minutes, while wash cycles are 10 minutes)*

Auxiliary Equipment Sizing and Operating Conditions

The reactors will need to be washed between capture and regeneration in order to remove impurities. For this, the condensate of the power cycle block will be used to wash the reactors rather than be reinjected back into the geothermal well. Since the washing process is not continuous, a holding tank is needed to contain the condensate over the course of a day, which totals approximately 6,738,000 liters. It is suggested that holding tanks be 1.5 times the maximum volume of the liquid to account for potential overfilling (Peters et al., 2003); thus, the volume of the wash water holding tank will be 10,100 m^3. This tank will be constructed out of stainless steel. After washing, reverse osmosis will be used to deionize and purify the dirty water, which can be used as a feed to the electrodialysis unit and sold as a product.

Prior to sending in the condensate to the tank, the stream is cooled with a countercurrent shell and tube heat exchanger using a 30 ^oC cooling water at 1.01 bar. The overall coefficient was calculated with the effect of fouling similar to the heat exchanger in the power cycle at 565.5 W m^{-2} K^{-1} (E 3.2.14). The heat transfer area is calculated in three stages with phase transition stage as the middle stage, and the total area is 2618 m^2 with 2277 pipes of .025 m radius and 7.2 m length. With the overall heat duty of 182 MW and exit temperature of cooling water at 45 ^oC, the amount of cooling water needed is 10,456,351 kg hr^{-1} (E 3.2.10). The exit stream of the heat exchanger flows to the reactors at 80 ^oC at 0.7 bar, which prevents melting the lithium intercalation reactors made out of HDPE. Similar to the tank, this heat exchanger is constructed using stainless steel.

A pump made from Monel is used to pump concentrated geothermal brine exiting the heat exchanger to the reactors. To compensate for friction loss through piping and control valves, the stream is brought to 2.1 bar. Assuming pump efficiency of 80%, the power requirement for this pump is estimated to be 38.8 kW (E 3.2.8).

The stream exiting the secondary reactor to electrolysis goes through a heat exchanger where the stream is heated to 50^oC using saturated steam at 1.01 bar. The overall coefficient of the shell and tube exchanger with steam and brine is estimated at 2750 W m^{-2} K^{-1}, and after accounting for fouling with fouling coefficient of 4000 W m^{-2} K^{-1} on the shell side and 15,000 W m^{-2} K^{-1} on the tube side, the corrected overall heat transfer coefficient is 1180 W m^{-2} K^{-1} (E 3.2.14). The heat transfer area of this heat exchanger is calculated to be 62 m^2 with 54 pipes, each with .025 m outer radius and 7.3 m in length, in a countercurrent single pass shell and tube heat exchanger (E 3.2.15). The flow rate of 39,706 kg hr^{-1} is required for the saturated steam to heat lithium rich brine from 41.7ºC to 50ºC. Because the brine remains corrosive, stainless steel is used to construct the heat exchanger.

3.4 ELECTRODIALYSIS

Introduction to Electrochemistry

In electrochemical engineering, reactions are driven by applying voltage across a cell. These cells typically contain two electrodes of opposite charges submerged in an electrolytic solution. The cathode, which is negatively charged, is the site at which reduction occurs ($E^o<0$). At the positively charged anode, oxidation occurs ($E^o > 0$). The voltage applied across these electrodes determines the products of the electrochemical reactions, which depend on the minimum applied voltage of reduction-oxidation reaction pairs.

In the electrodialysis cell, brine solution will be fed to the anode as water is supplied to the cathode. The following reactions occur at the anode and cathode in our system respectively:

$$2Fe^{2+} \rightarrow 2Fe^{3+} + 2e^- \qquad \text{(R 3.4.1)}$$

$$2\ H_2O + 2e^- \rightarrow 2\ OH^- + H_2 \qquad \text{(R 3.4.2)}$$

Reaction R 3.4.1 has a standard redox potential of 0.770 V whereas reaction R 3.4.2 has a redox potential of -0.827 V. The minimum voltage applied across one cell is thus:

$$E^o_{Cell} = E^o_{oxd} - E^o_{red} = 0.770\ V + 0.827\ V = 1.6\ V \quad \text{(E 3.4.1)}$$

The cathode and anode are separated by a cation exchange membrane (CEM) that allows for certain cations to pass from the anode to the cathode. In this electrodialysis system, Li^+ ions will be allowed to diffuse through the CEM to form LiOH while Fe^{2+} ions and trace Na^+ ions are rejected based on size. This migration of Li^+ ions across the CEM is driven by electric and chemical potential. The design of this electrodialysis unit was based upon the chlor-alkali process, a common industrial-scale technique in which sodium chloride (NaCl) fed at the anode is converted into sodium hydroxide (NaOH) at the cathode (O'Brien et al., 2005). This reaction also evolves chlorine gas (Cl_2) and has a minimum applied voltage of 2.1 V.

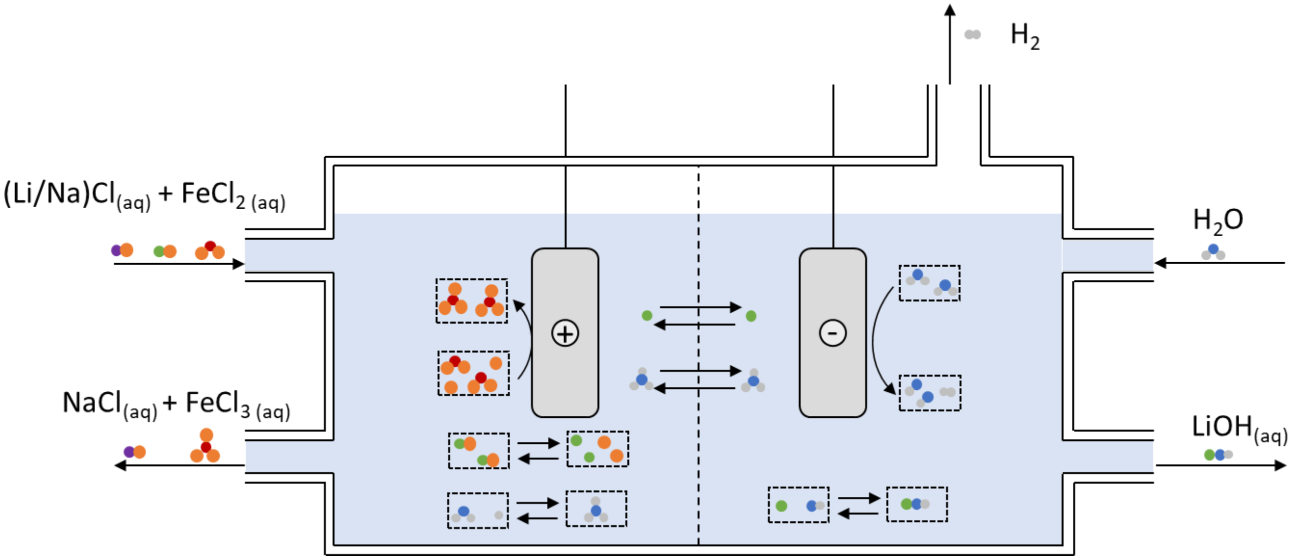

Figure 3.4.1: *Electrodialysis Cell for Production of Lithium Hydroxide*

Electrodialysis Unit Design

It is estimated that 170 kg hr^{-1} of Li^+ ions will enter the electrodialysis unit based on an overall recovery of 67% from the reactors. Assuming a Li^+ recovery of approximately 99% in the cell, our electrodialysis unit is estimated to produce 579 kg hr^{-1} of LiOH to be sent to the crystallizers.

To regenerate the Fe^{3+} used to remove Li^+ from the packed bed reactors, we will need to oxidize 1,366 kg hr^{-1} of Fe^{2+} to Fe^{3+}. Temperature and pressure of the electrodialysis unit were selected based on literature. Above a temperature of 50ºC, it was found that salt leakage through the CEM increased; this is undesirable as it would negatively impact purity (Grageda et al., 2020). A cell voltage of 2.0 V was selected. An overpotential of 0.4 V was provided to the system to ensure that kinetics and mass transfer across the membrane were favorable while remaining below the 2.1 V threshold that would result in the formation of chlorine gas. A current density of 1,700 A m^{-2} was selected based on literature and a current efficiency of 70%.

Anode and cathode construction materials were selected based on work performed by Grageda et al. The selected CEM, Nafion 117, is highly selective towards lithium ions and will only let approximately 0.01 wt% of the total Na^+ ions entering the system to diffuse across the membrane. A majority of the sodium ions will remain on the anode side of the electrodialysis unit, where Fe^{2+} is oxidized to form Fe^{3+}. Solution from the anode side is then recycled back to the reactor block for the lithium deintercalation step; this solution contains high concentrations of Fe^{3+}, Na^+, and Cl^-.

Without implementing a purge stream, the amount of Na^+ will accumulate in the recycle stream to the reactor block over time, resulting in undesirable impurities building up within the system. In order to prevent Na^+ ions from building up, a purge stream will be introduced. Sodium ions will be allowed to build in the system until there is a 1:1 ratio between Li^+ and Na^+ by moles leaving the anode side of the electrodialysis unit for recycle back to the reactor block. Because lithium rich brine enters the anode at a molar ratio of 63:1 of Li^+ to Na^+, the purge rate will be set equal to 1/63 of the solution feed rate entering electrodialysis.

Because the concentration of sodium ions is low in the entering stream with the implementation of a purge, formation of NaOH at the cathode can be considered negligible. Assuming that 0.01% of the Na^+ ions traverse the CEM, only 0.0009 kg hr^{-1} of Na^+ will be present in the LiOH-rich stream, corresponding to 0.0016 kg hr^{-1} of NaOH. LiOH leaves the electrodialysis unit through the same exit stream at a rate of 579 kg hr^{-1} of LiOH. This equates to 0.00028 wt% NaOH in the exit stream leading to the crystallization unit, which falls far below the acceptable maximum impurity concentration of 0.05%.

The electrodialysis unit designed here is an approximation of what could be used industrially. Insufficient data was available to accurately predict reaction kinetics and mass transfer limitations across the electrodialysis unit. Further research is required to appropriately predict these parameters, which would ultimately impact the reactor's operating conditions and sizing. Future research guidelines are further described in Section 7.

Electrolysis Sizing & Operating Conditions

The electrodialysis unit was sized using a number of correlations. The total required current across the reactor was calculated from the mass flow rate of Li^+ ions and current efficiency, yielding a value of 1,290,000 A. This was then used to determine the volume of the unit and number of cells with values of 761 m^3 and 127 respectively (Fuller & Harb, 2018). Electrode size was determined based on industry standards.

Knowing that the total voltage across the cell is 2.0 V, multiplying the current by the cell voltage yielded the power needed to run the electrodialysis unit.

$$P = IV \tag{E 3.3.7}$$

It was estimated that 2.58 MW of power would be required to run this unit. Out of the 2.58 MW needed to power the plant, some will be lost to parasitic reactions that create heat. Hydronium ions present in the brine will be able to traverse the CEM, combining with hydroxide ions at the cathode to form water. This side reaction will generate a considerable amount of heat, which can be estimated by assuming that only 30% of current is used to produce water and that the heat of formation of water, $\Delta H_{form, water}$, is equal to -286 kJ mol^{-1} (NIST, 2021). Thus, the electrodialysis unit will lose 0.573 MW of power as heat. The design specifications of the electrodialysis unit are summarized in Table 3.2.1.

To remove excess heat generated by the formation of water, a cooling jacket will be installed about the electrodialysis unit. Water will be used as a cooling fluid and is assumed to enter the electrodialysis jacket at 25℃ at a flow rate of 2,062,800 kg hr^{-1}. This cooling water will leave at a temperature of 50℃ and keep the reactor running at the appropriate temperature to minimize salt leakage across the CEM.

Table 3.4.1

Electrodialysis Operating Conditions & Materials of Construction

Parameter	Value
Temperature	50°C
Pressure	1.01 bar
Cell Voltage	2.0 V
Current Density	1700 A m^{-2}
Current Efficiency	70%
Anode to Cathode Distance	2 m
Area per Electrode/Membrane	6 m^2
Number of Cells	127
Total Unit Volume	761 m^3
Power Consumption	2.58 MW
Cathode Material	Nickel
Anode Material	Graphite
CEM Material	Nafion 117

Fuel Cell Sizing and Operating Conditions

A significant amount of hydrogen gas (H_2) is produced as a side product of the electrolysis reaction, totaling around 48 kg hr^{-1}. H_2 has a high value, particularly in fuel cells, which produce electricity via a redox reaction be oxygen gas (O_2):

$$H_{2\,(g)} + \tfrac{1}{2}\, O_{2\,(g)} = H_2O_{(l)} \qquad \text{(R 3.3.3)}$$

Fuel cells are highly efficient at converting chemical energy into electrical energy when compared to heat engines as fuel cells facilitate the electron transfer in an external circuit, while heat engineers rely on the heat released during combustion; an energy transfer process which is much less direct. H_2 has a fuel energy density of 121 MJ kg^{-1} (DOE, n.d.). Thus, assuming a fuel cell system with 100% energy conversion efficiency, the H_2 produced has a potential power generating capacity of 1.62 MW. This is a significant amount of electricity that could be used to supply power to various equipment units, such as pumps, which would reduce the amount of electricity used from the power plant. Because the H_2 stream coming out of electrolysis is highly pure and would not require any treatment prior to use in a fuel cell, it was decided that including a fuel cell system was ideal rather than flaring the H_2 gas as waste.

Battelle, a non-profit research and development company, outlines the design specification for a 10 kW Proton Exchange Membrane (PEM) fuel cell stack (Battelle, 2016). The PEM fuel cell is loaded with a platinum catalyst and utilizes a perfluorinated sulfonic-acid (PFSA) and polytetrafluoroethylene (PTFE) membrane that conducts protons between the graphite electrodes. Each cell has an active membrane area of 400 cm^2, with a single stack containing 36 cells. In total, 162 stacks would be needed to consume all of the H_2 gas. The fuel cell system also needs a source of O_2, which the authors indicate can be sourced from ambient air. Air is approximately 21% O_2 and 79% nitrogen gas (N_2) on a molar basis. Assuming air is added to the fuel cell system so that it is in a stoichiometric ratio to hydrogen according to R 3.3.3, and that the gases behave ideally, the mass flowrate of air to the system is 1,646 kg hr^{-1}. Because all of the O_2 and H_2 is consumed in the fuel cell, the outlet stream is composed of only water and N_2. A typical fuel cell system operates at a pressure between 3 - 4 bar to facilitate mass transfer across the membrane (Hoeflinger & Hofmann, 2020), thus the upper end pressure of 4 bar was chosen. Both gases are initially at 1.01 bar, and thus need to be pressurized before entering the system. The specifications for the fuel cell system are summarized in Table 3.4.3.

Table 3.4.3

Fuel Cell Operating Conditions & Materials of Construction

Parameter	Value
Pressure	4 bar
Power Production	1.62 MW
Membrane Area per Cell	400 cm^2
Number of Cells per Stack	36
Total Number of Stacks	162
Catalyst Loading	0.15 mg cm^{-2}
Electrode Material	Graphite
PEM Material	PFSA/PTFE
Catalyst Material	Platinum

Auxiliary Equipment Sizing and Operating Conditions

There are total of five pumps surrounding the electrolysis unit: a pump for pumping lithium rich brine to the anode, a pump for feeding pure water to the cathode, two compressors for putting hydrogen gas and air into the fuel cell, and a pump to send lithium effluent stream to crystallization unit. All pumps aside from the lithium rich brine pump are constructed using stainless steel and the hydraulic power is calculated under 80% pump efficiency assumption. The brine pump will be constructed out of Monel instead and is estimated to require 0.49 kW of power to pump 47,744 kg hr^{-1} of brine from 0.7 bar to 1.01 bar. The recycle water stream has a flow rate of 10,200 kg hr^{-1} and to raise the pressure from 0.61 bar to 1.01 bar, the estimated hydraulic power is 0.67 kW. The hydrogen gas leaving the electrodialysis unit has a flow rate of 48 kg hr^{-1} at 1.01 bar and before entering the fuel cell, the pressure of the stream has to be raised to 4 bar. The power requirement for this pressure change is calculated to be 65.6 kW assuming compressible flow. Air also enters the fuel cell at 1,645 kg hr^{-1}, which requires 144 kW of power to raise the pressure from 1.01 bar to 4 bar. Lastly, the aqueous, $FeCl_3$ rich stream exiting the electrodialysis unit at 47,574 kg hr^{-1} needs a pressure change from 1.01 bar to 1.6 bar to compensate for friction loss in the piping, so it requires 0.2 kW of power (E 3.2.8).

3.5 CRYSTALLIZATION

Thermodynamics of Lithium Hydroxide Monohydrate Crystallization

After electrodialysis, the aqueous 2.54 M LiOH stream is fed to the crystallization block in order to separate and purify the final $LiOH \bullet H_2O$ product. Crystallization describes the precipitation of solid particles out of solution. Precipitation occurs when a solution becomes supersaturated, indicating that more solute is dissolved in the solvent than is thermodynamically favorable. Once supersaturation is reached, $LiOH \bullet H_2O$ will form in the following reaction:

$$Li^{+}_{(aq)} + OH^{-}_{(aq)} + H_2O_{(l)} = LiOH \bullet H_2O_{(s)} \qquad \text{(R 3.5.1)}$$

Supersaturation can be achieved either by increasing the concentration of solute through the removal of solvent with evaporation or by reducing the solubility of the solute with undercooling or by adding an anti-solvent. On a lab scale, $LiOH \bullet H_2O$ is typically crystallized using ethanol as an antisolvent (Taboada et al., 2007). However, we decided to employ evaporative crystallization due to its simple design and ease of scalability. Additionally, evaporative crystallization does not require any additional feed materials, nor does it require refrigeration, which could be cost prohibitive on the scale of this process.

Process Design of Continuous Crystallization

In this process, we will be using forced circulation crystallization (FCC). FCC is a method of continuous evaporative crystallization that is commonly used for the large-scale production of commodity crystalline solids such as sugar and table salt (GEA, n.d.). Aqueous LiOH at 50℃ and 2.64 M is fed from the electrodialysis unit to a heat exchanger, where steam is used to heat the stream to 100℃. This stream is then fed to the crystallizer, where it is flashed at atmospheric pressure to evaporate as much water as possible. As water is evaporated, $\text{LiOH}\bullet\text{H}_2\text{O}$ precipitates out of solution as solid particles. The process takes place at 107℃. Some of the effluent slurry is recirculated back into the crystallizer. The recirculation of slurry is used to promote growth of new crystals by acting as nucleation sites, while also increasing the size of smaller crystals called fines (McCabe, 2005). Vapor coming out of the crystallizer is condensed and recycled back to the electrodialysis unit.

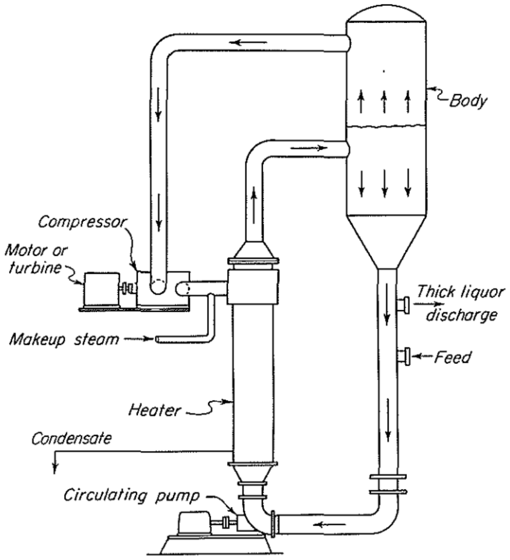

Figure 3.5.1: *Diagram of Forced Circulation Crystallization (McCabe, 1993)*

The remaining slurry is taken out of the crystallizer to be filtered using rotary drum filtration. In rotary drum filtration, slurry is fed to a trough, which a rotating drum is submerged in. The outer drum is covered in filter cloth, and a vacuum pump pulls solution through the cloth and out of the drum. The filtrate solution is still saturated with LiOH and is recycled back into the crystallizer to increase recovery. Some of the filtrate is taken out of the process as waste, called “bleed”, which prevents the build up of impurities. Wet cake is left on the surface of the filter cloth, which is then scraped off with a doctor blade. This wet cake is fed on a screen conveyor belt to a convection dryer, which circulates hot air around the wet cake in order to remove excess moisture left over from filtration. The final target specification of the product is 99.5 wt% $LiOH•H_2O$, which is battery-grade.

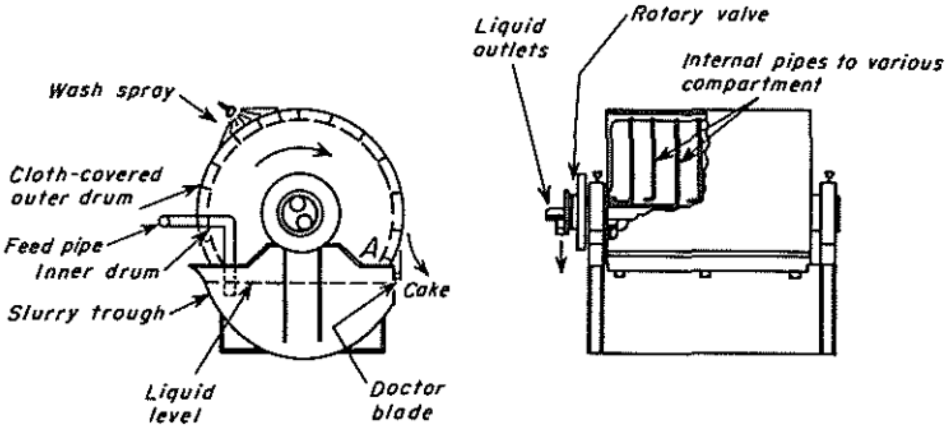

Figure 3.5.2: *Diagram of Continuous Rotary Drum Filtration (McCabe, 1993)*

Crystallizer Sizing and Operating Conditions

The crystallizer block in Aspen was used to model the FCC process. The component type of the $LiOH•H_2O$ was specified as solid, and the model was run with a base method of SOLIDS. This method allows Aspen to model the crystallization process. Nucleation, growth kinetics and particle size distribution were not accounted for as there was not enough data to comprehensively describe these parameters. Instead, solubility data was specified through the saturation concentration of $LiOH•H_2O$ from 255 K to 373 K (Monnin et al., 2005). To fully define the crystallizer block, the recirculation parameter was defined as 50% of the outlet slurry, which would be recycled back to the unit. In order to induce crystallization, the vaporization rate of water in the crystallizer was set to 95% of the total water fed to the crystallizer block.

Design of the crystallization unit was completed through the same method as the flash vessels in block 1. Once again, the minimum volume was found with the assumption that the holdup time would be 7.5 mins, an average time where the liquid level is assumed to be at half of the tank height (E 3.2.1). A volume of 3.96 m^3 was found and the L/D ratio of 3 was used in equation E 3.2.2 to find the diameter. This method was compared with a diameter found from permissible velocity equations (E 3.2.3 - E 3.2.7) to identify the most conservative estimate for the diameter of the crystallizer. Liquid and vapor mass flow rates and densities were used from the output steam and slurry streams exiting the crystallizer in this second method. Between these methods, the larger diameter is the conservative assumption and was found to be 0.93 m. Once the final diameter was established, length and final volume were calculated. The design of the crystallizer is detailed in Table 3.5.1.

Table 3.5.1
Design of Crystallization Unit

Parameter	Value
Temperature	107°C
Pressure	1.01 bar
Diameter	0.93 m
Length	2.83 m
Volume	3.96 m^3
Material of Construction	Stainless Steel

The crystallization of $LiOH•H_2O$ is an exothermic process and generates some of the heat necessary to promote crystallization. Here, we specifically tailored the inlet concentration from electrodialysis such that there would be no net heat duty for the crystallizer; in other words, every unit of heat generated from the crystallization reaction is used to vaporize the solvent. During start-up, there would need to be an initiation mechanism in order to get the reaction started. This could be accomplished by evaporating some of the initial feed or with seeding to create nucleation sites.

Rotary Drum Filtration Sizing and Operating Conditions

Material balances around the rotary drum filter were modeled using the filtration block in Aspen with the same methods used to model the crystallization unit. The fraction of solids to solids outlet was assumed to be 0.999, while the fraction of liquid to liquids outlet was assumed to be 0.998. The results of the material balance simulation were used to determine the filter area requirement using equations derived from McCabe. The filter area requirement, *A*, is:

$$A = m_{solid}\left(\frac{a_0\mu}{2c\Delta P^{1-s}fn}\right)^{0.5} \qquad \text{(E 3.5.1)}$$

Where m_{solid} is the mass flow rate of solid in the product slurry stream, a_0 is the specific cake resistance, assumed to be $1.95*10^{10}$ m kg^{-1}, μ is the viscosity of water at the operating temperature of the filtration unit, equal to 0.0002822 Pa-s, c is the mass of solid deposited on the filter per unit volume of filtrate in kg/m^3, ΔP is the differential pressure across the filter, equal to atmospheric pressure (101,325 Pa), s is the compressibility coefficient of the cake, assumed to be 0.2, f is the fraction of the drum that is submerged in the feed slurry, equal to 0.3725, and n is the rotational frequency of the drum, equal to 0.25 rev/s (Komline-Sanderson, n.d.). The value of c was calculated as:

$$c = \left(\frac{m_S}{V_S}\right)\left(1 - \left(\frac{m_F}{m_S} - 1\right)\frac{m_S}{V_S\rho}\right)^{-1} \qquad \text{(E 3.5.2)}$$

Where m_s is the mass flowrate of solid in the feed slurry, m_f is the total mass flowrate of the product wet cake, V_s is the volumetric flow rate of the feed slurry, and ρ is the density of the filtrate. All flow rate and density values were determined using Aspen simulation. The required filter area was calculated to be 0.591 m^2, or 6.356 ft^2. Komline-Sanderson sells industrial rotary drum filters that can accommodate this size at 9.4 ft^2. The pore size of the filter was assumed to be 75 μm (Graber et al., 2008). Additionally, while impurities are not considered in the simulation, it was assumed that the bleed rate would be 10% of the total filtration flow rate. At an operating differential pressure of 1.01 bar, and a total filtrate flow rate of 4.41E-4 m^3 s^{-1}, the hydraulic power requirement of the filter drum is 27 W.

Table 3.5.2

Design of Rotary Drum Filtration Unit

Parameter	Value
Filter Differential Pressure	1.01 bar
Hydraulic Power	27 W
Drum Diameter	3 ft
Drum Width	1 ft
Filter Area	9.4 ft^2
Filter Size	75 μm
Submerged Fraction of Drum	0.3725
Rotational Frequency	0.25 s^{-1}
Material of Construction	Stainless Steel

Dryer Sizing and Operating Conditions

The dryer was modeled using the FLASH2 block in Aspen with the same methods used to model the crystallization unit. The temperature of the flash was set to 150°C in order to evaporate off the majority of the water present in the wet cake. The resulting heat duty of the dryer is 22.7 kW, which yields a dry $LiOH•H_2O$ product with 99.9 wt% purity, meeting the 99.5 wt% product specification. Assuming hot air at 150°C would be used to evaporate the water, the required flow rate of air, m_{air}, is:

$$m_{air} = \frac{Q_{dry}}{H_{air}} \qquad \text{(E 3.5.3)}$$

Where Q_{dry} is the heat duty of the dryer, and H_{air} is the enthalpy of air at 150°C, equal to 151.02 kJ kg^{-1}. The resulting mass flow of air is 542.1 kg hr^{-1}. The dryer specifications are detailed in *Table 3.5.3*. The mechanical design of the dryer was not done in detail and does not account for its potential to absorb CO_2 as $LiOH \cdot H_2O$ will readily react with atmospheric CO_2 to form lithium carbonate (Li_2CO_3). The typical size range/operating times for screen conveyor dryers were listed (McCabe, 2001).

Table 3.5.3
Design of Screen Conveyor Dryer Unit

Parameter	Value
Heat Duty	22.74 kW
Dry Air Temperature	150°C
Air Flow Rate	542.1 kg hr^{-1}
Air Velocity	0.6 - 24 m s^{-1}
Drying Time	5 - 120 min
Dryer Length	4 - 150 m
Material of Construction	Stainless Steel

At the end of the process, the total production rate is 977 kg hr^{-1} of $LiOH \cdot H_2O$ product, which translates to a yearly production rate of 7,701 tonnes/yr for a plant uptime of 90%.

Auxiliary Equipment Sizing and Operating Conditions

To compensate for the pressure loss through elevation for the stream going into the crystallizer, a pump is used to bring pressure up to 2.29 bar with 0.5 kW of power. A secondary pump is used in this block to send filtrate back to the crystallizer as well with 0.029 kW of power

(E 3.2.8). Stainless steel is used to construct these pumps to prevent possible corrosion from the LiOH.

For the vapor coming off of the crystallizer, it is passed through a heat exchanger before recycling it back to the electrodialysis unit. The countercurrent shell and tube heat exchanger uses cooling water at 30ºC that exits at 45ºC to condense vapor from 107.8ºC to 50ºC. Heat transfer area of this heat exchanger is calculated with three stages: 107.8ºC to 100ºC in vapor phase, phase change at 100ºC, and 100ºC to 50ºC in liquid phase. The overall heat transfer coefficient is estimated similar to previous heat exchanger designs where coefficient for liquid and liquid heat transfer is 562.5 W m^{-2} K^{-1} and coefficient for liquid and steam is 1180 W m^{-2} K^{-1} (E 3.2.14). In total, the heat transfer area is calculated at 314 m^2 with 273 pipes made from stainless steel for corrosion resistivity. With overall heat duty of around 22 MW, the flow rate of cooling water is 114,784 kg hr^{-1}. The exiting stream drops 0.4 bar in pressure and is sent to electrolysis.

Once dry $LiOH{\bullet}H_2O$ comes out the dryer, it is sent to a storage tank before selling it as a product. Per heuristics, a typical storage tank has storage capacity of 30 days with tanks designed to hold 1.5 times the capacity (Peters et al., 2003). Based on the flow rate of $LiOH{\bullet}H_2O$, the tank volume is calculated to be 700 m^3, which is oriented vertically on a concrete foundation. The tank itself is made out of stainless steel with a diameter of 6.67 m and height of 20 m.

3.6 REVERSE OSMOSIS WATER TREATMENT

Water Recovery using Reverse Osmosis

Reverse osmosis is a water purification process that separates ions and other dissolved solids from water by applying pressure, which forces mass transport of water through a permeable membrane. The end result is two streams: the permeate, composed of purified water, and the retentate, which contains unrecovered water and waste ions. The goal of the reverse osmosis block is to offset the water usage in the electrolysis block by purifying the wash water from lithium reactors. The remaining water left over can be sold to make a profit. In order to reach the desired purity, the reverse osmosis system will be designed with 27 pressure vessels, each including 7 semi-permeable membranes. Water condensed from the three flashes in the power generation process will be moved into the lithium intercalation reactors and used as wash water. This water will then be put through reverse osmosis (RO) and purified to a level that can be sold for further processing or reused within the plant. The water exiting the power cycle as condensate will be at 103℃; after it is cooled and used as wash water at 80℃, it will exit the reactors with an average temperature of 72.95℃ and need to be cooled to a temperature of 25℃ for the RO process.

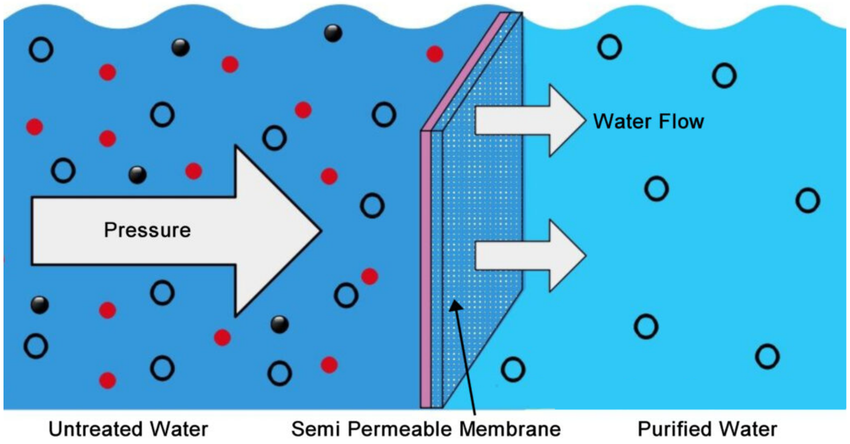

Figure 3.6.1: *Diagram of Reverse Osmosis Process (Chemical Engineering World, 2020)*

The inlet flow to the RO system comes from the wash water used in the intercalation reactors, which has a volumetric flow rate of 7,575,000 L day^{-1}. The volume of the reactors was used for calculating the volumetric flow rate of the wash water to ensure that at least two wash volumes were used. The reactors, modeled as cylinders, were found to have a volume of 345.4 m^3 for one set of primary and secondary reactors. The total volume of water leaving the washing step is the sum of the volume of brine remaining in the reactors and the total volume of the condensate collected from the power cycle in one day after it was cooled to 25℃; this was found to be 7,575,000 L. Since the RO system operates continuously every day, this volume is loaded into a tank and then emptied entirely in one day to provide a flow rate of 7,575,000 L day^{-1} into the RO system.

Estimating Ion Concentration of Wash Water Exiting the Reactors

The concentration of the wash water exiting the reactors was assumed to be dominated by the brine loaded into the reactors that the wash water "picks up" as it flows through the intercalation reactors. All of the wash water available is used in this system in order to lower the concentration of contaminants. Ultimately, the outlet, dirty wash water coming out of the intercalation reactors has a mass flow rate of 315,005 kg hr^{-1} and a concentration of 1.08 M of dissolved ions. All dissolved ions from the initial brine stream were accounted for.

Concentration assumptions were necessary in order to compute the osmotic pressure of the water entering and exiting the RO system. In order to generate flux across the membrane, there must be a positive difference between the pressure vessel that is housing the membranes and the osmotic pressure exiting the vessel. The osmotic pressure calculations are based on the following equation:

$$\Pi = iCRT \tag{E 3.6.1}$$

Where Π is the osmotic pressure, i is the Van't Hoff index, C is the molar concentration of the solute, R is the ideal gas constant and T is temperature in kelvin. A Van't Hoff index of 2 was used for these calculations. This value was selected because the i of sodium and chloride ions are both equal to 2, which make up the majority of the ions present in solution. The inlet wash water had an osmotic pressure of 53.7 bar and the retentate had an osmotic pressure of 80.5

bar with 50% recovery. A recovery of 50% was selected in order to lower the osmotic pressure and allow for the pressure vessels to operate at 82 bar. This is under the max pressure of 83 bar, allowing for a positive difference of 6 bar to create flux.

RO Equipment Sizing and Operating Conditions

Wash water must be transported and cooled using a large pump and heat exchanger before entering the RO pressure vessels. The wash water must be cooled from 79.2℃ to 25℃ in order to enter the membrane, and the feed needs to be increased in pressure up to 82 bar. The temperature of 25℃ was selected for operation because it is the average seawater temperature typically used in large scale applications for these membranes. It was assumed that this large pump had 80% efficiency and required a power input of 1,085 kW.

At 50% recovery, the permeate will have a flow rate of 3,788,000 L day^{-1}, or 158,000 kg hr^{-1} of pure water. RO systems are designed for a specified permeate flow, and the number of membranes required can be found from E 3.6.2.

$$\mathrm{N_E} = \frac{Q_T}{r_E Q_A} \qquad \text{(E 3.6.2)}$$

Where N_E is the number of membrane elements, Q_T is the total permeate flow, Q_A is the permeate flow per element, and r_E is the single element recovery rate. Membranes purchased from Lenntech (ID: FilmTecTM SW30HR-320) were selected because they are highly resistant to fouling and require less frequent replacement. These spiral wound membranes have specifications shown in Table 3.6.1.

Table 3.6.1
Specifications for FilmTecTM SW30HR-320 membrane element

Parameter	Value
Operating Pressure	82 bar
Outer Diamter	7.900 in
Inner Diameter	1.125 in
Single Element Length	40 in
Single Element Recovery Rate	8%
Exiting Flow Rate	23,000 L day^{-1}
Active Membrane Area	320 ft^2
Membranes per Vessel	7

The permeate flow per element, Q_A, was found from the single element recovery rate and the exiting flow rate of the membrane. Using E 3.6.1, the number of membrane elements, N_E, was found to be 179 membranes. The number of pressure vessels is then found by E 3.6.3.

$$N_v = \frac{N_E}{P_E} \qquad \text{(E 3.6.3)}$$

Where N_V is the number of pressure vessels and P_E is the number of elements per vessel. Literature indicates that 6 to 8 membranes is the most common configuration, so 7 membranes per vessel was chosen as an average (Fritzmann et al., 2007). With 179 membranes and 7 membranes per vessel, 25.5 vessels are required. Because the permeate is being sent to three different series of pressure vessels, N_V was rounded up to get 27 pressure vessels, which corresponds to 189 membranes total. Pressure vessels purchased from Lenntech (ID: 8-E-1200-1M-to-8M-R6) were selected because of their max operating pressure of 83 bar.

Auxiliary Equipment Sizing and Operating Conditions

From the lithium intercalation block, wash water is brought to the reverse osmosis unit where it first passes through the heat exchanger to lower the temperature of the stream from 79.2ºC to 25ºC. To achieve this temperature drop, a cooling water flowing at 1,006,965 kg/hr at 10ºC is used. The overall heat transfer coefficient is estimated at 562.5 W m^{-2} K^{-1} (E 3.2.14). The exit temperature of the cold stream is 25ºC with a heat transfer area of 1,195 m^2. The heat exchanger is made with stainless steel in a countercurrent shell and tube type with 1,040 pipes for cold water to flow (E 3.2.15). This heat exchanger is expected to drop the pressure of the stream by 0.4 bar according to heuristics, so a pump is required to pressurize it back to the operating pressure of 82 bar. Assuming 80% efficiency, a pump is constructed using stainless steel with hydraulic power of 1085 kW.

The reverse osmosis requires two tanks: one to hold the wash water before entering the pressure vessels and one to store the permeate before selling it as a product. We assumed the hold up time to be 1 day for the wash water tank because of the 24 hr reactor schedule and volume to be 1.5 times the actual capacity. Therefore with the flow rate of 315,005 kg hr^{-1}, the tank volume is calculated to be 11,363 m^3, which is rounded up to 11,400 m^3. For the permeate tank, the flow rate of the stream is 157,503 kg hr^{-1}, so the tank volume is calculated at 113,629 m^3 assuming 30 day storage, which is rounded up to 113,700 m^3. These tanks are constructed using stainless steel.

4. DESIGN

4.0 SILICATE TREATMENT & STEAM GENERATION

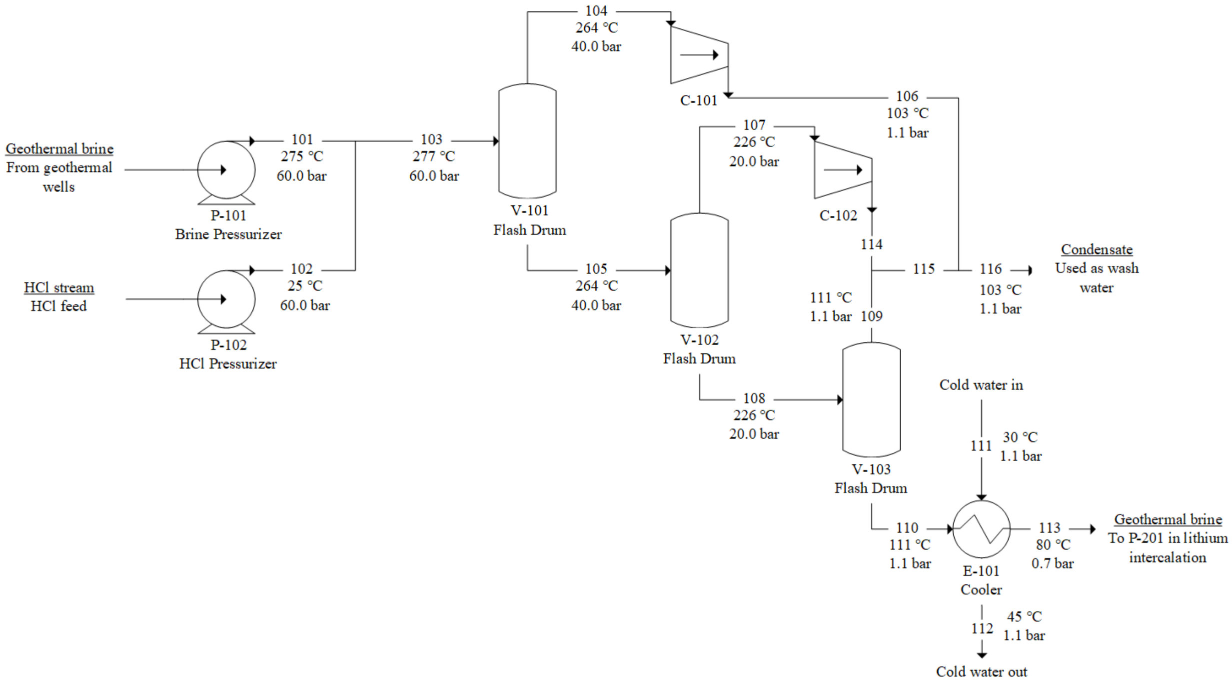

Figure 4.0.1: *Silicate Treatment and Steam Generation for Power Cycle Process Flow Diagram*

Silicate treatment is the first step in the process and is designed to prevent fouling of equipment and buildup of silica deposits. Liquid brine is brought to the surface at a flow rate of 1,242,589 kg hr^{-1} using pump P-101. The brine leaves the pump at a temperature and pressure of 275℃ and 60 bar. To ensure that silicates do not crash out of solution, 2,491 kg hr^{-1} of 9.6M HCl solution is mixed with stream 101 to lower the pH of the solution. Pump P-102 is a 1.45 kW pump with 80% efficiency that pressurizes the HCl to 60 bar so that it can be mixed with brine. Streams 101 and 102 are mixed without the use of process equipment since flow through the tubing is turbulent. The resulting stream, 103, has a pH of 2.36, temperature of 277℃, and pressure of 60 bar.

Stream 103 then enters flash vessel V-101 for the first of its flashes to generate steam. The first flash takes the brine at 60 bar and flashes it to 40 bar, reducing its temperature to 264°C. A total of 142,847 kg hr^{-1} of vapor is produced from the first flash, including trace amounts of HCl. Thorough heat integration of V-101 and subsequent flash vessels in this process was omitted as it is considered outside of the scope of our project. The flash vessel will be constructed out of Monel 400 to prevent corrosion from the highly acidic brine. To accommodate the large inlet flow, V-101 is designed to have a L/D ratio of 3 and mean residence time of 7.5 minutes, yielding vessel dimensions of 4.17 m diameter, 12.5 m height, and total volume of 342 m^3.

Vapor from V-101 is subsequently sent to a turbine to generate power for the geothermal plant. Design of C-101 and other turbines were considered to be outside of the scope of this project. Assuming an isentropic turbine with 100% mechanical efficiency, C-101 will generate 18.2 MW of electrical power for general use. The 40 bar, 264°C steam entering the turbine in stream 104 drops to a pressure of 1.1 bar and temperature 103℃ in stream 106.

The more concentrated brine, stream 105, leaving V-101 then flows to the second flash vessel, V-102. The flash drops the pressure and temperature of stream 105 from 40 bar and 264℃ to 20 bar and 226℃ in streams 107 and 108. This flash produces 96,113 kg hr^{-1} of a mixed water-HCl vapor. As with the V-101, V-102 will be constructed out of corrosion-resistant Monel 400 and follows the same design rationale. The flash vessel is 3.94 m in diameter, 11.8 m in height, and 288 m^3 in volume.

Stream 107 flows from V-102 to C-102, which generates 9.89 MW of electrical power using the same simulation assumptions as C-101. The 20 bar, 226°C steam entering the turbine in stream 107 drops to a pressure of 1.1 bar and temperature 103℃ in stream 114.

Stream 108 enters V-103 for the final flash in the series. The 226℃, 20 bar brine from stream 108 is flashed to 111℃ and 1.1 bar. The cylindrical vessel is once again constructed of Monel 400 with a diameter of 3.71 m, height of 11.1 m, and volume of 241 m^3. Because the vapor produced in this flash is at such low pressure, it is not useful for power generation in a turbine. The vapor from all three flash processes, including streams 106, 109, and 114, will be combined and sent to wash the lithium intercalation reactors. These vapors are condensed in the lithium intercalation block before the washing process.

From the final flash vessel, the concentrated brine at 111ºC and 1.1 bar then passes through heat exchanger E-101 to decrease temperature to 80℃. Frictional losses in the exchanger cause the pressure to drop from 1.1 bar to 0.7 bar in stream 113. Concentrated brine is cooled using cooling water, which enters from stream 111 at 30℃ and 1.1 bar and leaves from stream 112 at 45℃ and 1.1 bar.

Table 4.0.1A

Flow Summary of the Silicate Pretreatment and Steam Generation for Power Cycle Process

	Stream	101	102	103	104	105	106	107	108
	Temperature, °C	275	25	277	264	264	103	226	226
	Pressure, bar	60	60	60	40	40	1.1	20	20
	pH	6.72	-1.75	2.36	-	2.53	0.48	-	2.5
	Density, kg/m^3	915	1130	912	18.2	961	0.707	9.32	1050
	IN/OUT	IN	IN	MID	MID	MID	MID	MID	MID
	Phase	Liquid	Liquid	Liquid	Vapor	Liquid	Liquid/Vapor	Vapor	Liquid
	Mass flow, kg/hr	1,242,589	2,491	1,245,079	142,847	1,102,071	143,002	96,113	1,005,903
Component flow, kg/hr	H_2O	940,000	1,520	941,520	142,520	799,000	142,520	96,000	703,000
	HCl	0	0	0	327	0	13	113	0
	H_3O^+	0	339	339	0	169	164	0	110
	Li^+	252	0	252	0	252	0	0	252
	Na^+	65,100	0	65,100	0	65,100	0	0	65,100
	K^+	19,600	0	19,600	0	19,600	0	0	19,600
	Ca^{2+}	1,850	0	1,850	0	1,850	0	0	1,850
	Mn^{2+}	39,100	0	39,100	0	39,100	0	0	39,100
	Fe^{2+}	2,280	0	2,280	0	2,280	0	0	2,280
	Cl^-	174,000	632	174,632	0	174,314	305	0	174,205
	SiO_2	406	0	406	0	406	0	0	406

Table 4.0.1B

Flow Summary of the Silicate Pretreatment and Steam Generation for Power Cycle Process

	Stream	109	110	111	112	113	114	115	116
	Temperature, °C	105	111	30	45	80	103	103	103
	Pressure, bar	1.1	1.1	1.1	0.7	0.7	1.1	1.1	1.1
	pH	-	2.2	7.0	7.0	2.2	0.63	0.43	0.52
	Density, kg/m^3	0.625	1210	997	997	1210	0.692	0.657	0.690
	IN/OUT	MID	MID	IN	OUT	OUT	MID	MID	OUT
	Phase	Vapor	Liquid	Liquid	Liquid	Liquid	Liquid/Vapor	Liquid/Vapor	Liquid/Vapor
	Mass flow, kg/hr	41,003	964,696	1,393,871	1,393,871	964,696	96,166	137,169	280,173
Component flow, kg/hr	H_2O	41,000	662,000	1,393,871	1,393,871	662,000	96,000	137,000	279,520
	HCl	3	0	0	0	0	4	7	22
	H_3O^+	0	108	0	0	108	57	57	221
	Li^+	0	252	0	0	252	0	0	0
	Na^+	0	65,100	0	0	65,100	0	0	0
	K^+	0	19,600	0	0	19,600	0	0	0
	Ca^{2+}	0	1,850	0	0	1,850	0	0	0
	Mn^{2+}	0	39,100	0	0	39,100	0	0	0
	Fe^{2+}	0	2,280	0	0	2,280	0	0	0
	Cl^-	0	174,000	0	0	174,000	105	105	410
	SiO_2	0	406	0	0	406	0	0	0

Table 4.0.2

Equipment Summary of the Silicate Pretreatment and Steam Generation for Power Cycle Process

Equipment ID	Name	Equipment Type	Specifications
P-101	Brine Pressurizer	Pump	2.78 MW, centrifugal, Stainless Steel
P-102	HCl Pressurizer	Pump	4.5 kW, centrifugal, Monel
V-101	High Pressure Flash Drum	Vessel	Total volume of 342 m^3, Monel 400
V-102	Moderate Pressure Flash Drum	Vessel	Total volume of 288 m^3, Monel 400
V-103	Low Pressure Flash Drum	Vessel	Total volume of 241 m^3, Monel 400
C-101	High Pressure Turbine	Turbine	Isentropic, 100% efficiency, and 19 MW power generation
C-102	Moderate Pressure Turbine	Turbine	Isentropic, 100% efficiency, and 10 MW power generation
E-101	Brine Cooler	Heat Exchanger	Shell-and-tube exchanger, countercurrent, Monel, Area of 772 m^2

4.1 LITHIUM ION INTERCALATION

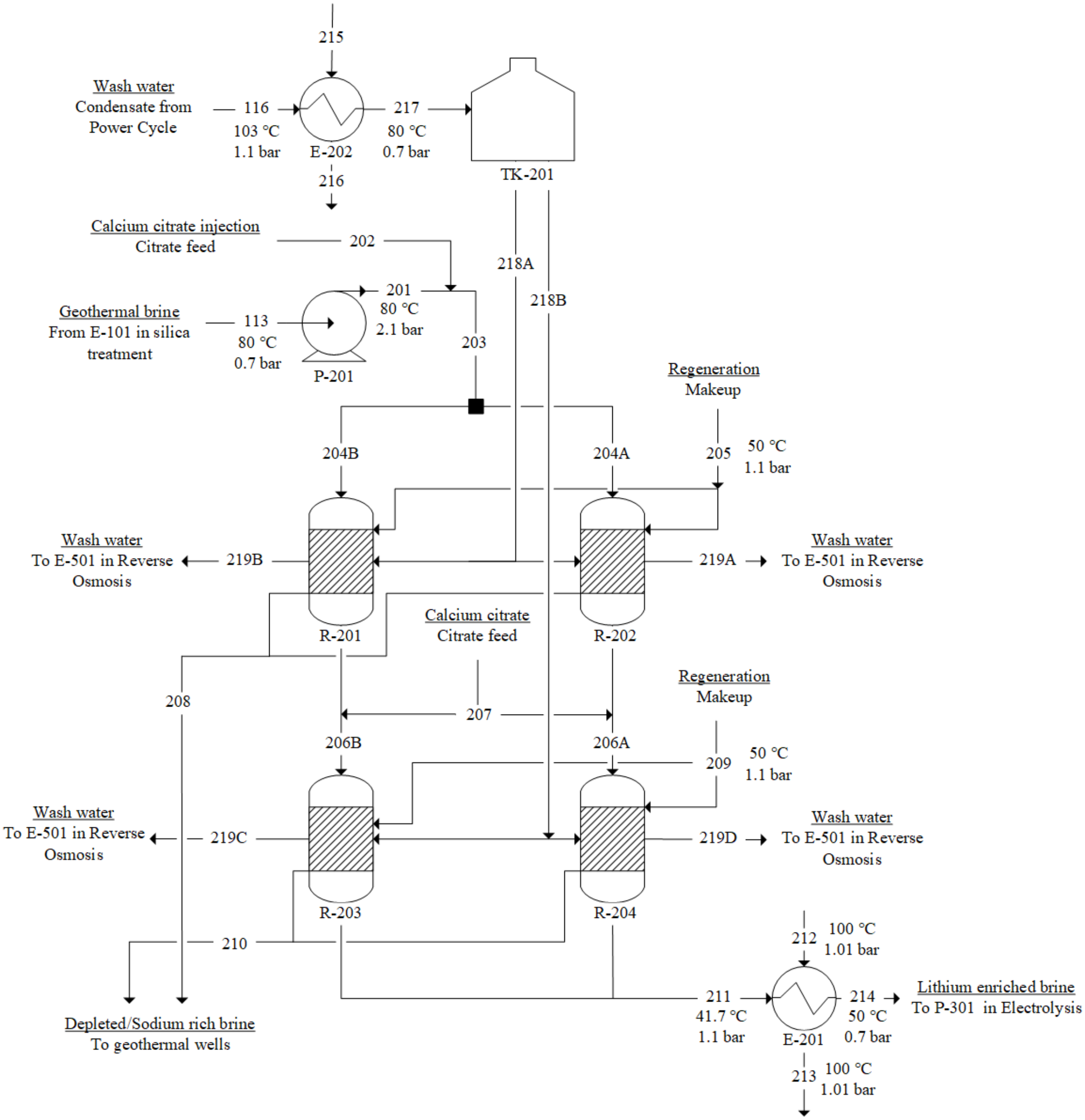

Figure 4.1.1: *Lithium Ion Intercalation Reactor Process Flow Diagram*

After the silicate pretreatment and power generation step, concentrated brine flows to the lithium ion capture/release reactors. Stream 113 from the previous block is repressurized from 0.7 bar to 1.1 bar using the 11.1 kW pump P-201 to account for frictional losses from heat exchanger E-101. A total of 39,300 kg hr^{-1} of solid calcium citrate is then added to stream 201, which mixes to form stream 203 at 80℃ and 1.1 bar. Stream 203 is then redirected as stream 204A or 204B to one of the primary reactors, which include R-201 and R-202. In primary lithium capture mode, the primary reactors operate at 80℃ and 1.1 bar. The reactors will be constructed of high density polyethylene (HDPE). Reactors are based on a packed shell and tube design where brine flows through the tubes and reacts with the iron phosphate pellets. The iron phosphate pellets have spherical geometry with a diameter of 2 mm.

The primary reactors each contain a total of 2,715 tubes with a diameter of 4” and length of 12 m. With a linear velocity of 1 cm s^{-1}, the average residence time of a fluid packet in the reactor is 20 minutes. This is estimated to capture 70% of Li^+ ions passing through the reactor. The bed is expected to reach 80% saturation after a span of 24 hours. This bed saturation also includes capture of Na^+ ions; there are approximately 0.6 moles of Li^+ ions for every 1 mol of Na+ ions after the first pass from the primary reactor to the secondary reactor. Excess brine is pumped back down the well in stream 208.

Once the primary bed reaches 80% saturation, flow from the current primary reactor is cut off and switched to a new primary reactor. To recover Li+ ions from the reactor, stream 205 is added at 50℃ and 1.1 bar. Stream 205 is a 500 mM $FeCl_3$ solution that enters with a flow rate of 134,271 kg hr^{-1}, which recovers Li^+ and Na^+ trapped within the iron phosphate sorbent. The $FeCl_3$ solution will enter the bed at a temperature of 50℃ and leave at 42.2℃. A total of 176 kg hr^{-1} of Li+ ions and 1,011 kg hr^{-1} of Na^+ ions are recovered from the primary reactor and fed to the secondary reactor. Stream 207 will be mixed with the exiting stream before entering the secondary reactor as streams 206A and 206B.

The secondary reactors, which include R-203 and R-204, are also constructed out of HDPE and are designed in a shell and tube style. The reactors are paired such that R-201 feeds

R-203 and R-202 feeds R-204. The secondary reactors each contain a total of 835 tubes with 4” diameter and 12 m length. During the capture step, these beds will trap 96% of Li^+ ions and reach a saturation of 99% after 24 hours. The linear velocity through the bed will be 0.572 cm s^{-1}. The secondary reactor will operate at approximately 50℃ with temperature fluctuations caused by the capture and release step. During lithium capture, brine enters at 42.2℃ and is expected to leave the bed is at 45℃. In this step, a majority of the sodium ions and a small fraction of lithium ions are not captured by the secondary reactor; they are pumped back down into the geothermal well in stream 210.

Following the lithium capture step in the secondary reactor, lithium ions and a small number of sodium ions are released using the same 500 mM $FeCl_3$ solution as mentioned for the primary reactor. Stream 209 is fed at 47,566 kg hr^{-1} and 50℃ to ensure that all ions are released from the bed. Stream 211 leaves the reactor at 41.7℃ and 1.1 bar and must then be heated using heat exchanger E-201.

Heat exchanger E-201 heats stream 211 to reach the desired temperature of 50℃ before electrodialysis. Stream 211 is heated using steam at 100℃ and 1.01 bar from stream 212. Stream 212 is condensed into water at 100℃. Stream 214 leaves the series of reactors at 50℃ and 0.7 bar, containing 170 kg hr^{-1} Li^+ ions.

Table 4.1.1A

Flow Summary and Material Balances of the Lithium Ion Intercalation Process

	Stream	113	116	201	202	203	204A-B	205	206A-B	207	208	209
	Temperature, °C	80	103	80	-	80	80	50	42.2	25	81.5	50
	Pressure, bar	0.7	1.1	2.1	-	1.1	1.1	1.1	1.1	-	1.1	1.1
	Density, kg/m^3	1210	0.69	1210	1630	-	-	1030	1070	1630	1230	1030
	IN/OUT	IN	IN	MID	IN	MID	MID	IN	MID	IN	OUT	IN
	Phase	Liquid	Liquid/Vapor	Liquid	Solid	Liquid	Liquid	Liquid	Liquid	Solid	Liquid	Liquid
	Mass flow, kg/hr	964,696	280,173	964,696	39,300	1,003,996	1,043,296	134,271	135,458	13,900	1,002,810	47,566
Component flow, kg/hr	H_2O	662,000	279,520	662,000	0	662,000	662,000	123,071	123,070	0	662,000	44,960
	H_3O^+	108	221	108	0	108	108	0	0	0	108	0
	Li^+	252	0	252	0	252	252	0	176	0	77	0
	Na^+	65,100	0	65,100	0	65,100	65,100	0	1,011	0	64,089	0
	K^+	19,600	0	19,600	0	19,600	19,600	0	0	0	19,600	0
	Ca^{2+}	1,850	0	1,850	0	1,850	1,850	0	0	0	1,850	0
	$Mn2^+$	39,100	0	39,100	0	39,100	39,100	0	0	0	39,100	0
	Fe^{2+}	2,280	0	2,280	0	2,280	2,280	0	3,860	0	2,280	0
	Fe^{3+}	0	0	0	0	0	0	3,860	0	0	0	1,366
	Cl^-	174,000	410	174,000	0	174,000	174,000	7,340	7,340	0	174,000	2,606
	SiO_2	406	0	406	0	406	406	0	0	0	406	0
	$Ca_3(C_6H_5O_7)_2$	0	0	0	39,300	39,300	39,300	0	0	13,900	39,300	0

Table 4.1.1B

Flow Summary and Material Balances of the Lithium Ion Intercalation Process

	Stream	210	211	212	213	214	215	216	217	218A-B	219A-D
	Temperature, °C	45	41.7	100	100	50	30	45	80	80	72.95
	Pressure, bar	1.1	1.1	1.01	0.61	0.7	1.01	0.61	0.7	0.7	0.7
	Density, kg/m^3	1018	1012	0.598	997	1012	997	997	972	972	-
	IN/OUT	OUT	MID	IN	OUT	OUT	IN	OUT	MID	MID	OUT
	Phase	Liquid	Liquid	Vapor	Liquid	Liquid	Liquid	Liquid	Liquid	Liquid	Liquid
	Mass flow, kg/hr	149,180	47,744	38,706	38,706	47,744	10,456,351	10,456,351	280,173	280,173	315,005
Component flow, kg/hr	H_2O	123,070	43,593	38,706	38,706	43,593	10,456,351	10,456,351	279,520	279,520	302,487
	HC1	0	0	0	0	0	0	0	22	22	22
	H_3O^+	0	0	0	0	0	0	0	221	221	225
	Li^+	8	170	0	0	170	0	0	0	0	9
	Na^+	1,002	9	0	0	9	0	0	0	0	2,259
	K^+	0	0	0	0	0	0	0	0	0	680
	Ca^{2+}	0	0	0	0	0	0	0	0	0	64
	$Mn2^+$	0	0	0	0	0	0	0	0	0	1,357
	Fe^{2+}	3,860	1,366	0	0	1,366	0	0	0	0	79
	Fe^{3+}	0	0	0	0	0	0	0	0	0	0
	Cl^-	7,340	2,606	0	0	2,606	0	0	410	410	6,447
	SiO_2	0	0	0	0	0	0	0	0	0	14
	$Ca_3(C_6H_5O_7)_2$	13,900	0	0	0	0	0	0	0	0	1,363

Table 4.1.2

Equipment Summary in the Lithium Ion Intercalation Process

Equipment ID	Name	Equipment Type	Specifications
P-201	Pressurizer	Pump	38.8 kW, centrifugal, Monel
R-201	Primary Reactor 1	Reactor	Shell-and-tube reactor, HDPE, and paired to R-203
R-202	Primary Reactor 2	Reactor	Shell-and-tube reactor, HDPE, and paired to R-204
R-203	Secondary Reactor 1	Reactor	Shell-and-tube reactor, HDPE, and paired to R-201
R-204	Secondary Reactor 2	Reactor	Shell-and-tube reactor, HDPE, and paired to R-202
TK-201	Condensate Tank	Tank	11,500 m^3 volume
E-201	Preheater	Heat Exchanger	Shell-and-tube exchanger, countercurrent, Stainless Steel, Area of 62 m^2
E-202	Condesate Cooler	Heat Exchanger	Shell-and-tube exchanger, countercurrent, Stainless Steel, Area of 2,618 m^2

4.2 ELECTRODIALYSIS

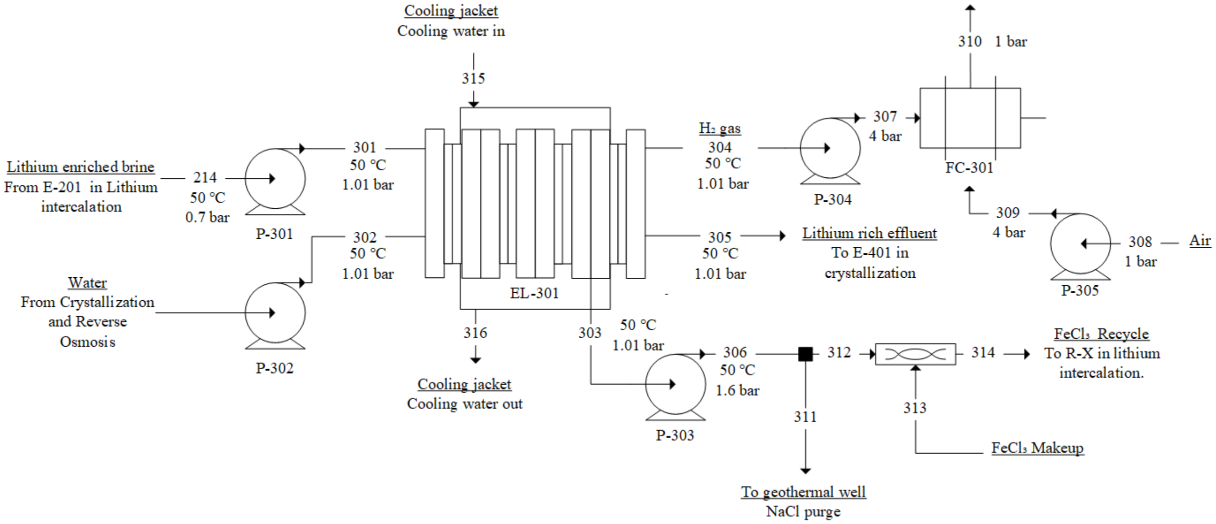

Figure 4.2.1: *Electrodialysis Process Flow Diagram*

The electrodialysis process is designed to convert aqueous LiCl from the Li^+ intercalation process into LiOH. In the electrodialysis process block, the lithium-rich brine from the secondary reactors in the lithium ion capture/release process is pumped to the anodes at 50℃. The solution first passes through P-301 to make up pressure from frictional losses. Water from the RO process is pumped to the cathodes using P-302, also at 50℃. Streams 301 and 302 will need to be split into 127 streams to provide equal flow to each cell in EL-301, resulting in flow rates of 376 kg hr^{-1} of lithium-rich liquid to each anode and 80.3 kg hr^{-1} of water to each cathode.

EL-301 is a 127 cell electrodialysis unit. Each electrode has an area of 6 m^2 and is separated by a distance of 2 m. A Nafion 117 membrane of thickness 0.25" bisects each cell. The total volume of the unit is 761 m^3. The anode and cathode are constructed of graphite and nickel respectively. The current density across each cell is 1,700 A m^{-2} with an applied voltage of 2.0 V. EL-301 consumes 2.59 MW of electrical power assuming 70% current efficiency.

Aqueous Li^+, Na^+, Cl^-, and Fe^{2+} enter on the anode side of each cell. Due to lack of kinetic and mass transfer data, it is assumed that 99% of Li^+ ions entering EL-301, 170 kg hr^{-1}, will diffuse across the CEM. The same rationale was used to justify complete oxidation of 1,366 kg hr^{-1} Fe^{2+} to 1,366 kg hr^{-1} Fe^{3+}. The Na^+ entering the anode side is ultimately rejected by the CEM, as Nafion 117 is highly selective towards small, monovalent cations. A total of 9 kg hr^{-1} of Na^+ enters the electrodialysis process block, effectively all of which leaves the system through stream 303.

To prevent accumulation of sodium within the recycle stream, a purge stream will be introduced. It was assumed that Na^+ and Li^+ would leave the system in a 1:1 mole ratio. As the ratio of Li^+/Na is 63:1 in the feed to electrodialysis, the purge was designed to operate at a flow rate of 1/63rd the inlet to the electrodialysis unit. Stream 311 is taken off the recycle stream and sent back down the geothermal well at a rate of 755 kg hr^{-1}. As $FeCl_3$ is lost in the purge, a makeup stream is necessary to replenish lost reagents for the intercalation reactors. Stream 313 is mixed with stream 312 at a rate of 755 kg hr^{-1} to make up for lost iron and water, which is then recycled to the reactors.

Pure water in excess enters the cathode from stream 302, where it is split into 409 kg hr^{-1} of OH^- anions and 48.1 kg hr^{-1} of hydrogen gas. Hydroxide anions coordinate with Li^+ ions that have diffused across the CEM to form aqueous LiOH at 2.64 M. Stream 305 containing the LiOH then flows to the crystallization unit. In addition to Li^+ diffusing across the CEM, hydronium cations can move from the anode to cathode side of the electrodialysis unit due to its small size. Hydronium can coordinate with hydroxide on the cathode side and to produce water and waste heat. To handle this, a cooling jacket will be used to remove excess heat. Stream 315, the inlet to the cooling jacket, requires 2,062,800 kg hr^{-1} of 25℃. Cooling water leaves in stream 316 at a temperature of 50℃.

The hydrogen gas produced at the cathode leaves in stream 304 and will be utilized to produce energy in a fuel cell. Compressor P-304 pressurizes the hydrogen gas to the desired 4 bar pressure, requiring 66.6 kW of power. Ambient air is pumped directly to the cell at 25℃ and 4 bar at a rate of 1,646 kg hr^{-1} using P-305, which uses 147 kW of power. Fuel cell FC-301 will generate a total of 1.62 MW to be sold or used within the plant. Detailed design of the cell was considered outside of the scope of this project.

Table 4.2.1A

Flow Summary and Material Balances of the Electrodialysis Process

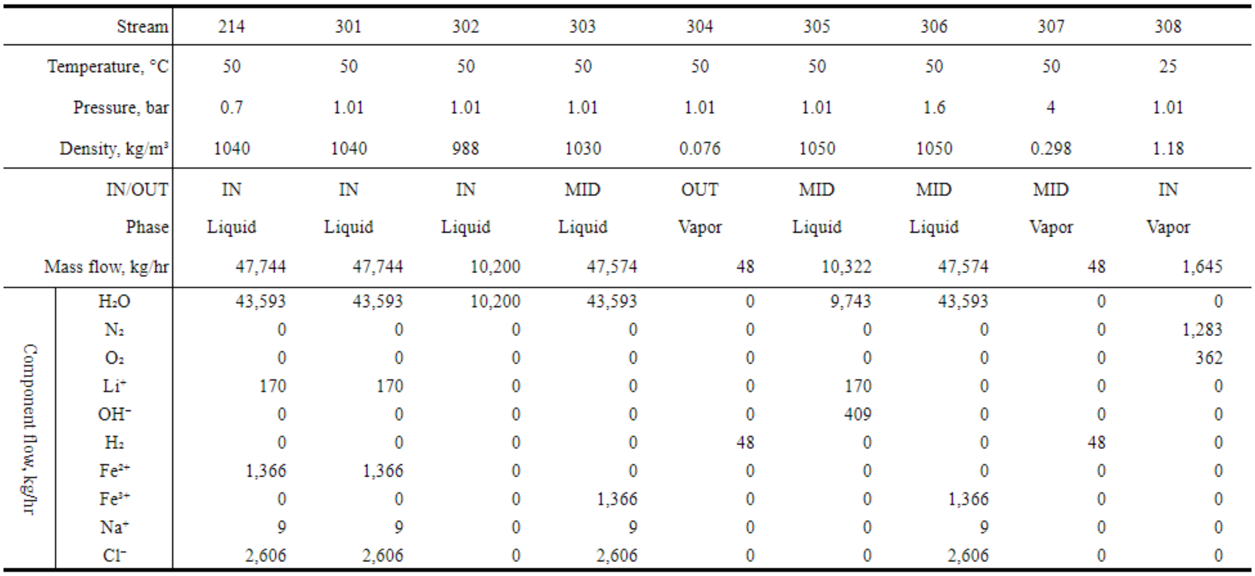

	Stream	214	301	302	303	304	305	306	307	308
	Temperature, °C	50	50	50	50	50	50	50	50	25
	Pressure, bar	0.7	1.01	1.01	1.01	1.01	1.01	1.6	4	1.01
	Density, kg/m³	1040	1040	988	1030	0.076	1050	1050	0.298	1.18
	IN/OUT	IN	IN	IN	MID	OUT	MID	MID	MID	IN
	Phase	Liquid	Liquid	Liquid	Liquid	Vapor	Liquid	Liquid	Vapor	Vapor
	Mass flow, kg/hr	47,744	47,744	10,200	47,574	48	10,322	47,574	48	1,645
Component flow, kg/hr	H_2O	43,593	43,593	10,200	43,593	0	9,743	43,593	0	0
	N_2	0	0	0	0	0	0	0	0	1,283
	O_2	0	0	0	0	0	0	0	0	362
	Li^+	170	170	0	0	0	170	0	0	0
	OH^-	0	0	0	0	0	409	0	0	0
	H_2	0	0	0	0	48	0	0	48	0
	Fe^{2+}	1,366	1,366	0	0	0	0	0	0	0
	Fe^{3+}	0	0	0	1,366	0	0	1,366	0	0
	Na^+	9	9	0	9	0	0	9	0	0
	Cl^-	2,606	2,606	0	2,606	0	0	2,606	0	0

Table 4.2.1B

Flow Summary and Material Balances of the Electrodialysis Process

	Stream	309	310	311	312	313	314	315	316
	Temperature, °C	25	50	50	50	50	50	25	50
	Pressure, bar	4	4	1.01	1.01	1.01	1.01	1.01	1.01
	Density, kg/m^3	4.68	4.31	1050	1050	1050	1050	997	988
	IN/OUT	MID	OUT	OUT	MID	IN	OUT	IN	OUT
	Phase	Vapor	Vapor	Liquid	Liquid	Liquid	Liquid	Liquid	Liquid
	Mass flow, kg/hr	1,645	1,645	755.08	46,819	755	47,574	2,062,800	2,062,800
Component flow, kg/hr	H_2O	0	410	692	42,901	692	43,593	2,062,800	2,062,800
	N_2	1,283	1,283	0	0	0	0	0	0
	O_2	362	0	0	0	0	0	0	0
	Li^+	0	0	0.04	0	0	0	0	0
	OH^-	0	0	0	0	0	0	0	0
	H_2	0	0	0	0	0	0	0	0
	Fe^{2+}	0	0	0	0	0	0	0	0
	Fe^{3+}	0	0	22	1,344	22	1,366	0	0
	Na^+	0	0	0.04	9	0	9	0	0
	Cl^-	0	0	41	2561	41	2,606	0	0

Table 4.2.2

Equipment Summary in the Electrodialysis Process

Equipment ID	Name	Equipment Type	Specifications
P-301	Brine Pressurizer	Pump	0.49 kW, centrifugal, Monel
P-302	Water Pressurizer	Pump	0.11 kW, centrifugal, Stainless steel
P-303	Recycle Pressurizer	Pump	0.2 kW, centrifugal, Stainless steel
P-304	H2 Compressor	Compressor	66.6 kW, centrifugal, Stainless steel
P-305	Air Compressor	Compressor	146.7 kW, centrifugal, Stainless steel
FC-301	Hydrogen Fuel Cell	Fuel Cell	1.62 MW power generation, Graphite electrode, PFSA/PTFE PEM, Platinum catalyst
EL-301	Electrodialysis Unit	Electrodialysis	2.58 MW, Graphite anode, Nickel aathode, Nafion 117 CEM, 6 m^2 electrode area, 127 cells, and total volume of 761 m^3

4.3 CRYSTALLIZATION

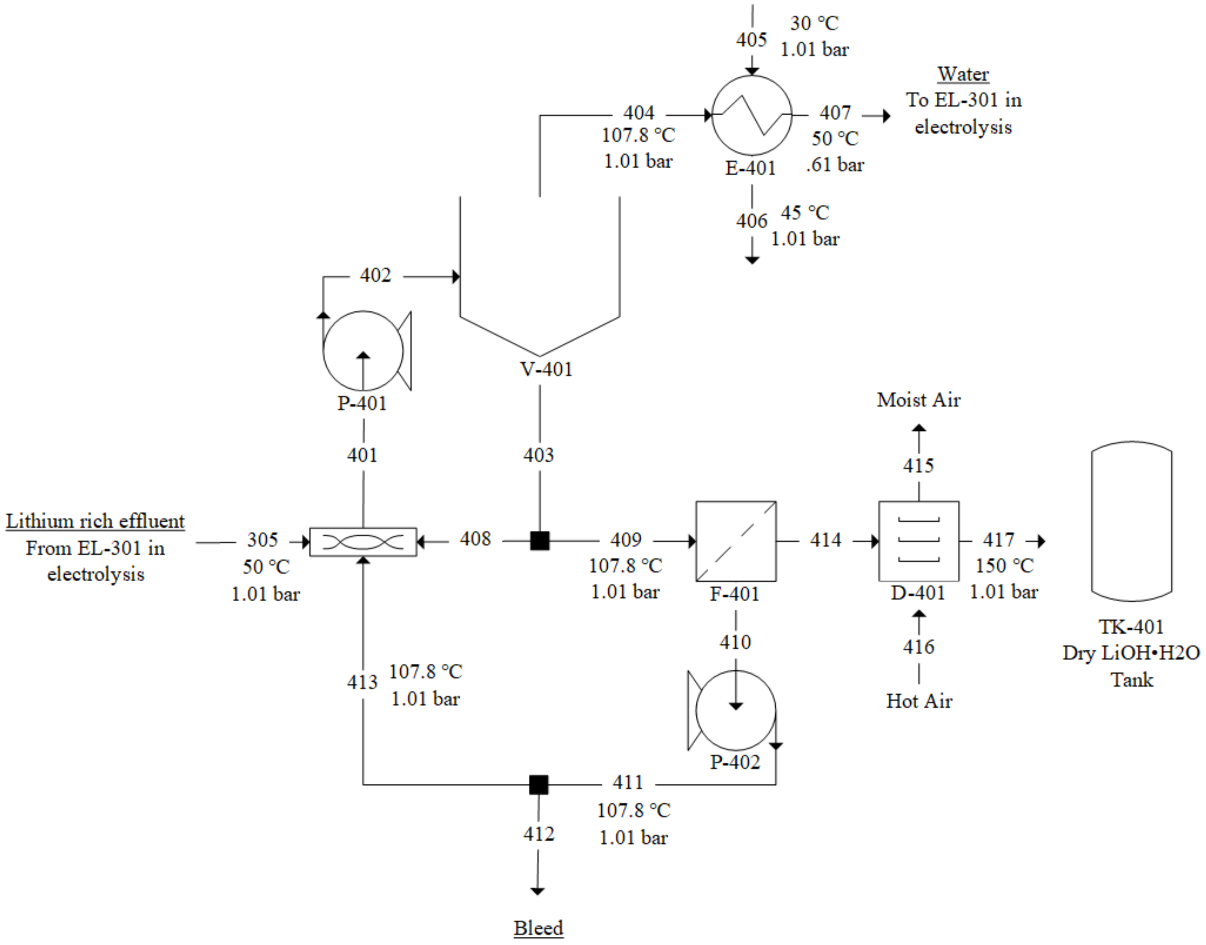

Figure 4.3.1: *Crystallization Process Flow Diagram*

The crystallization process is designed to separate and purify the final LiOH•H_2O product. LiOH solution coming from the electrodialysis process (stream 305) enters the crystallization process at 50°C and 1.01 bar. This stream is mixed with recycle streams 408 and 413 to yield the stream 401, which is then fed to the crystallization unit V-401. Here, water from the feed is vaporized, resulting in the crystallization of LiOH•H_2O. The crystallization unit operates at 1.01 bar and has a total volume of 3.96 m^3, with a length of 2.93 m and diameter of 0.93 m. During steady state operation, this unit operates with a net heat duty of 0 MW as the heat generated during the crystallization reaction is used to vaporize the water. Steam coming out of the top of TK-401 is condensed and cooled 50°C and 1.01 bar using shell and tube heat exchanger E-401. Cooling water at 30ºC is used to remove 6.71 MW of heat. Coming out of the bottom of V-401 (stream 403) is a slurry stream containing solid LiOH•H_2O and saturated LiOH solution. This stream is equally split into streams 408 and 409, which is recycled back into the crystallizer and filtration unit F-401 respectively.

F-401 is a rotary drum filter obtained from Komline-Sanderson with an outer drum diameter of 3 ft and a drum width of 1 ft, resulting in a total filter area of 9.4 ft^2. The drum rotates at a frequency of 0.25 s^{-1}, and 37.25% of the drum volume is submerged in the feed slurry. Additionally, the drum operates with a differential pressure of 1.01 bar, which requires a hydraulic power of 27 W. Filtrate containing saturated LiOH solution comes out of the center of the drum in stream 408; this stream is then split into streams 410 and 414, with 90% of stream 410 going into stream 413, which is recycled back into the crystallizer. Stream 412 is referred to as bleed and is reinjected back into the well, which helps prevent the build up of impurities. After filtration, the wet LiOH•H_2O is scraped off of the filter cloth and sent to a screen conveyor dryer, D-401, which circulates hot, dry air at 150°C counter-current to the wet-cake in order to remove excess moisture. Moist air is vented into the atmosphere as waste. The final, dry LiOH•H_2O product has a mass-based purity of 99.9% and is sent to silo TK-401 for storage.

Table 4.3.1A

Flow Summary and Material Balances of the Crystallization Process

	Stream	305	401	402	403	404	405	406	407	408
	Temperature, °C	50	50.3	50.3	108	108	30	45	50	108
	Pressure, bar	1.01	1.01	2.29	1.01	1.01	1.01	1.01	1.01	1.01
	Density, kg/m^3	1050	1051	1051	1300	0.6	997	997	984	1300
	IN/OUT	IN	MID	MID	MID	MID	IN	OUT	OUT	MID
	Phase	Liquid	Liquid/Vapor	Liquid/Vapor	Liquid	Vapor	Liquid	Liquid	Liquid	Liquid
	Mass flow, kg/hr	10,785	11,755	11,755	4,116	9,698	114,784	114,784	9,698	2,058
Component flow, kg/hr	H_2O	10,209	11,011	11,011	1788	9,698	114,784	114,784	9,698	894
	Li^+	167	215	215	108	0	0	0	0	54
	OH^-	409	528	528	264	0	0	0	0	132
	$LiOH \cdot H_2O$	0	0.9	0.9	1956	0	0	0	0	978
	Air	0	0	0	0	0	0	0	0	0

Table 4.3.1B

Flow Summary and Material Balances of the Crystallization Process

	Stream	409	410	411	412	413	414	415	416	417
	Temperature, °C	108	108	108	108	108	108	150	150	150
	Pressure, bar	1.01	0.01	1.01	1.01	1.01	1.01	1.01	1.01	1.01
	Density, kg/m^3	1300	1150	1150	1150	1150	1509	0.8	0.8	1510
	IN/OUT	MID	MID	MID	OUT	MID	MID	IN	OUT	OUT
	Phase	Liquid	Liquid	Liquid	Liquid	Liquid	Liquid	Vapor	Vapor	Solid
	Mass flow, kg/hr	2,058	1,079	1,079	107	970	979	542	544	978
Component flow, kg/hr	H_2O	894	892	892	89	803	1.8	0	1.6	0.2
	Li^+	54	54	54	5	48	0.1	0	0	0.1
	OH^-	132	132	132	13	118	0.2	0	0	0.3
	$LiOH \cdot H_2O$	978	1	1	0.1	1	977	0	0	977
	Air	0	0	0	0	0	0	542	542	0

Table 4.3.2

Equipment Summary in the Crystallization Process

Equipment ID	Name	Equipment Type	Specifications
P-401	Crystallizer Feed Pressurizer	Pump	0.5 kW, centrifugal, Stainless Steel
P-402	Filtrate Pressurizer	Pump	0.029 kW, centrifugal, Stainless Steel
V-401	Crystallizer	Vessel	Total volume of 3.96 m^3
F-401	Rotary Drum Filter	Filter	26.4 W, outer diameter of 3 ft, width of 1 ft
D-401	Dryer	Dryer	Screen conveyor system, dried with hot air at 150C, and countercurrent
TK-401	Dry $LiOH*H_2O$ Silo	Silo	700 m^3 volume
E-401	Steam Condenser/Cooler	Heat Exchanger	Shell-and-tube exchanger, countercurrent flow, Area of 314 m^2

4.4 REVERSE OSMOSIS WATER TREATMENT

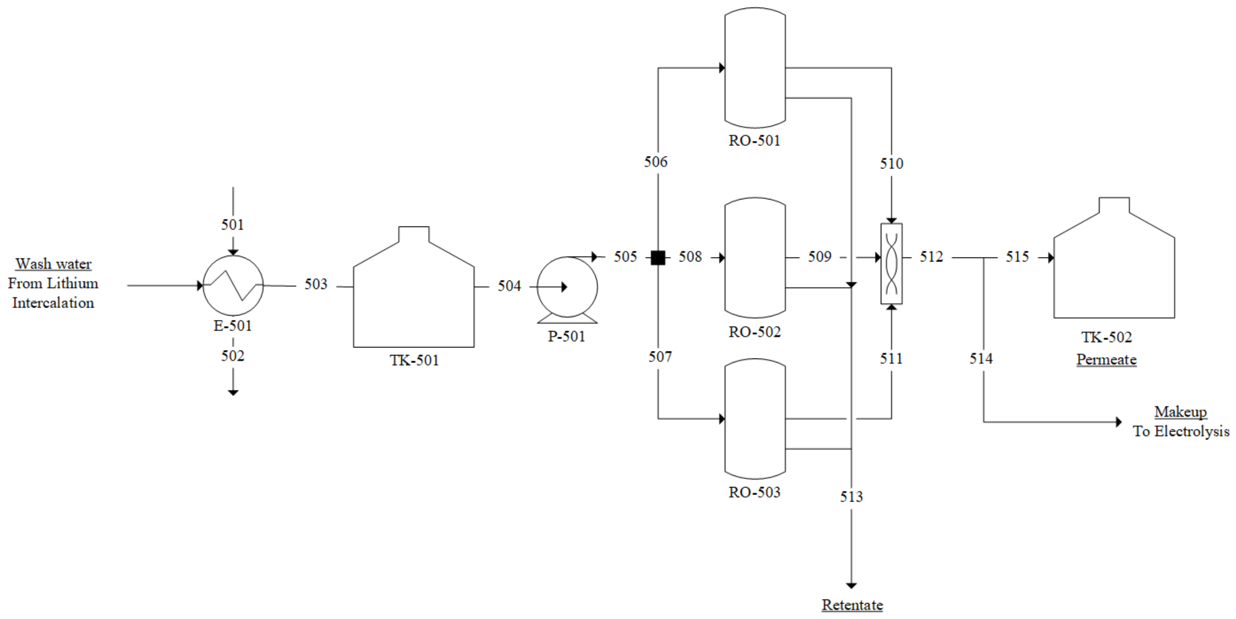

Figure 4.4.1: *Reverse Osmosis Process Flow Diagram*

The reverse osmosis process is designed to purify the wash water used in the lithium intercalation reactors to a level that allows it to be sold as potable water. The wash water exits the reactors at 79.2℃ and is cooled to 25℃ and 0.61 bar using shell and tube heat exchanger E-501. Tank TK-501, with a volume of 11,400 m^3, allows the reverse osmosis system to run continuously by storing the water from the 10 minute daily wash cycle. Stream 504 is pressurized up to 82 bar through pump P-501, requiring 1085 kW, before it enters the reverse osmosis pressure vessels. Each reverse osmosis vessel shown in Figure 4.5.1 represents 9 pressure vessels in series for a total of 27 pressure vessels. Pressure vessels were purchased from Lenntech (ID: 8-E-1200-1M-to-8M-R6) and have a max operating pressure of 83 bar. Within each pressure vessel, there are 7 membranes purchased from Lenntech (ID: FilmTecTM SW30HR-320). After the contaminated wash water stream exits the RO vessels, the purified permeate streams are mixed together and stored in tank TK-502, which has a volume of 113,700 m^3. Stream 513 is the higher concentrated retentate stream and is disposed of by reinjecting it back into the well.

Table 4.4.1

Flow Summary and Material Balances of the Reverse Osmosis Water Treatment Process

	Stream	219A-D	501	502	503	504	505	506	507	508
	Temperature, C	79.2	10	25	25	25	25	25	25	25
	Pressure, bar	0.7	1.01	1.01	0.3	0.3	82	82	82	82
	Density, kg/m^3	-	998	998	998	998	998	998	998	998
	IN/OUT	IN	IN	OUT	MID	MID	MID	MID	MID	MID
	Phase	Liquid	Liquid	Liquid	Liquid	Liquid	Liquid	Liquid	Liquid	Liquid
	Mass flow, kg/hr	315,005	1,006,965	1,006,965	315,005	315,005	315,005	105,002	105,735	105,735
Component flow, kg/hr	H_2O	302,487	1,006,965	1,006,965	302,487	302,487	302,487	100,829	100,829	100,830
	HCl	22	0	0	22	22	22	7	7	7
	H_3O^+	225	0	0	225	225	225	75	75	75
	Li^+	9	0	0	9	9	9	3	3	3
	Na^+	2,259	0	0	2,259	2,259	2,259	753	753	753
	K^+	680	0	0	680	680	680	227	227	227
	Ca^{2+}	64	0	0	64	64	64	21	21	21
	Mn2+	1,357	0	0	1,357	1,357	1,357	452	452	452
	Fe^{2+}	79	0	0	79	79	79	26	26	26
	Fe^{3+}	0	0	0	0	0	0	0	0	0
	Cl^-	6,447	0	0	6,447	6,447	6,447	2,149	2,149	2,149
	SiO_2	14	0	0	14	14	14	5	5	5
	$Ca_3(C_6H_5O_7)_2$	1,363	0	0	1,363	1,363	1,363	454	454	454

Table 4.4.1B

Flow Summary and Material Balances of the Reverse Osmosis Water Treatment Process

	Stream	509	510	511	512	513	514	515
	Temperature, C	25	25	25	25	25	25	25
	Pressure, bar	82	82	82	82	82	82	82
	Density, kg/m^3	998	998	998	998	998	998	998
	IN/OUT	MID	MID	MID	MID	OUT	OUT	OUT
	Phase	Liquid	Liquid	Liquid	Liquid	Liquid	Liquid	Liquid
	Mass flow, kg/hr	105,735	105,735	105,735	157,503	157,503	502	157,001
Component flow, kg/hr	H_2O	52,501	52,501	52,501	157,503	144,984	502	157,001
	HCl	0	0	0	0	22	0	0
	H_3O^+	0	0	0	0	225	0	0
	Li^+	0	0	0	0	9	0	0
	Na^+	0	0	0	0	2,259	0	0
	K^+	0	0	0	0	680	0	0
	Ca^{2+}	0	0	0	0	64	0	0
	$Mn2^+$	0	0	0	0	1,357	0	0
	Fe^{2+}	0	0	0	0	79	0	0
	Fe^{3+}	0	0	0	0	0	0	0
	Cl^-	0	0	0	0	6,447	0	0
	SiO_2	0	0	0	0	14	0	0
	$Ca_3(C_6H_5O_7)_2$	0	0	0	0	1,363	0	0

Table 4.5.2

Equipment Summary in the Reverse Osmosis Water Treatment Process

Equipment ID	Name	Equipment Type	Specifications
P-501	Water Pressurizer	Pump	1085 kW, centrifugal, Stainless Steel
RO-501	RO Pressure Vessel Series 1	Vessel	Represents 9 pressure vessels in series, each with 7 membranes, individual volume of 2.1 m^3
RO-502	RO Pressure Vessel Series 2	Vessel	Represents 9 pressure vessels in series, each with 7 membranes, individual volume of 2.1 m^3
RO-503	RO Pressure Vessel Series 3	Vessel	Represents 9 pressure vessels in series, each with 7 membranes, individual volume of 2.1 m^3
E-501	Cooler	Heat Exchanger	Shell-and-tube exchanger, countercurrent flow, Stainless Steel, Area of 1219 m^2
TK-501	Post Wash Holding Tank	Tank	11,400 m^3 volume, Stainless Steel
TK-502	Permeate Tank	Tank	113,700 m^3 volume, Stainless Steel

5. PROCESS ECONOMICS

The economic feasibility of this process was analyzed through a cash flow analysis, which was used to calculate an internal rate of return (IRR). IRR value is used to judge whether the project should be invested in or not. Performing a cash flow analysis requires fixed costs, operating costs, and revenue to be estimated. Many of the calculations done in this section involve the use of the Chemical Engineering Plant Cost Index (CEPCI), which accounts for monetary inflation and deflation effects for the capital costs of a chemical plant. For this analysis, the CEPCI was set to the 2022 value of 800.

Fixed costs are primarily associated with equipment capital costs, costs of land, and working capital. The majority of the purchased equipment costs were estimated using CAPCOST, a pre-made Microsoft Excel spreadsheet that uses macros to perform economic calculations (Turton, 2018). The cost of equipment that could not be accurately predicted using CAPCOST was estimated manually. After purchased equipment costs were estimated, they were multiplied by a Lang Factor, which increases the total capital cost by taking into account indirect expenses, such as labor, transportation, taxes, insurances, administration, and utilities that are needed to fully install the equipment onsite. A Lang Factor of 3.63 for a "mixed fluids-solids processing plant" was used in these calculations (Towler and Sinnott, 2013). Working capital and land costs were estimated to be 20% and 2% of the total equipment capital costs, respectively.

Operating costs are primarily associated with the cost of feedstocks, utilities, and labor, while revenue is associated with the value of material products and other marketable commodities. Feedstocks and material products were priced using market prices from various sources. Utilities, including steam, cooling water, and air, were priced using correlations based on the CEPCI and natural gas prices in California. Costs and revenue from materials was calculated on the basis of 90% plant uptime, or 7,884 operating hours per year. Electricity prices and labor costs were provided from industry advisors from Team TELEPORT. The operational lifetime of the plant was chosen as 20 years, and thus the IRR was calculated based on this lifespan.

5.0. SILICATE PRETREATMENT AND STEAM GENERATION FOR POWER CYCLE

With this process, it is assumed that the lithium extraction plant would be retrofitted to an existing geothermal power plant. Therefore, the economic costs and revenue associated with already existing equipment and feedstocks were not considered in this analysis. This results in much of the silicate pretreatment and steam generation block being excluded, including the flash vessels, turbines, and pumps. Additionally, this means that the revenue from the electricity generated in this block was ignored. The only equipment that was considered was the heat exchanger used to cool the post-flash brine (E-101), which was priced using CAPCOST. The equipment capital costs for this block are summarized in Table 5.0.1.

Table 5.0.1

Costs of Equipment for Silicate Pretreatment and Steam Generation for Power Cycle Process

Equipment ID	Name	Specifications	Material of Construction	Purchaced Equipment Cost, $	
E-101	Brine Cooler	772 m^2	Monel	$	131,000.00
			Total, $	$	131,000.00
			Lang Factor Total, $	$	475,530.00

Table 5.1.2 summarizes the utility costs. Cooling water is used in E-101 to lower the brine temperature. Cooling water was priced using correlations developed by Ulrich et al. (2006).

Table 5.0.2

Costs of Utilities for Silicate Pretreatment and Steam Generation for Power Cycle Process

Stream	Utility Type	Unit Price, \$ kg^{-1}	Feed Rate, kg hr^{-1}	Cost, \$ yr^{-1}
111	Cooling Water	0.00015	1,393,871	\$ 1,674,194.15
			Total, \$	\$ 1,674,194.15

5.1. LITHIUM ION INTERCALATION

All of the equipment in this block, including the lithium intercalation reactors, pumps, heat exchangers, and holding tanks, were priced using CAPCOST. Approximately 827 tonnes of iron (III) phosphate is needed for the four intercalation reactors. Using the market price for $FePO_4$, this comes out to \$3.3 million, which was included in the capital cost for the equipment. Additionally, it was assumed that the iron (III) phosphate would be replaced yearly, which adds \$3.3 million per year to operating cost for raw materials. The equipment capital costs for the lithium intercalation process are summarized in Table 5.1.1.

Table 5.1.1

Costs of Equipment for Lithium Ion Intercalation Process

Equipment ID	Name	Specifications	Material of Construction	Purchaced Equipment Cost, \$	
P-201	Pressurizer	38.76 kW, 2.1 bar	Monel	\$	13,000.00
R-201	Primary Reactor 1	264.2 m^3	HDPE	\$	7,180,000.00
R-202	Primary Reactor 2	264.2 m^3	HDPE	\$	7,180,000.00
R-203	Secondary Reactor 1	81.2 m^3	HDPE	\$	2,210,000.00
R-204	Secondary Reactor 2	81.2 m^3	HDPE	\$	2,210,000.00
-	Iron (III) Phosphate	827 tonnes	-	\$	3,308,000.00
E-201	Preheater	62 m^2	Stainless Steel	\$	40,800.00
E-202	Condensate Cooler	2,618 m^2	Stainless Steel	\$	425,000.00
TK-201	Condensate Tank	10,100 m^3	Stainless Steel	\$	761,000.00
			Total, \$	\$	23,327,800.00
			Lang Factor Total, \$	\$	84,679,914.00

Table 5.1.2 summarizes the total operating costs associated with feedstocks for the lithium ion intercalation block, which were priced using market prices for the materials. The feedstock for this block includes calcium citrate, iron (III) chloride, and iron (III) phosphate. The projected cost of the calcium citrate feed was excluded from the cash flow analysis as including it would guarantee the process would be economically unviable.

Table 5.1.2
Costs of Raw Materials for Lithium Ion Intercalation Process

Stream	Raw Material	Unit Price, \$ kg^{-1}	Feed Rate, kg hr^{-1}	Cost, \$ yr^{-1}
202/207	Calcium Citrate	1.30	53,200	\$ 545,257,440.00
205/209	Iron (III) Chloride	0.55	11,200	\$ 48,565,440.00
-	Iron (III) Phosphate	4.00	105	\$ 3,308,000.00
			Total, \$	\$ 597,130,880.00

Table 5.1.3 summarizes the utility costs for the lithium ion intercalation block. Low pressure steam is fed to E-201 in order to heat the lithium rich solution entering electrodialysis. Additionally, cooling water is fed to E-202 to cool the condensate from the power cycle in preparation for washing. Like the cooling water, the steam was priced using correlations developed by Ulrich et al. (2006).

Table 5.1.3
Costs of Utilities for Lithium Ion Intercalation Process

Stream	Utility Type	Unit Price, \$ kg^{-1}	Feed Rate, kg hr^{-1}	Cost, \$ yr^{-1}
212	LP Steam	0.06134	38,706	\$ 18,716,993.65
215	Cooling Water	0.00015	10,456,351	\$ 12,559,240.92
			Total, \$	\$ 18,716,993.65

Table 5.1.4 summarizes electricity costs for the lithium ion intercalation block. Here, the only unit that uses electricity is P-201, which pumps the brine from the pretreatment block to the intercalation reactors. Electricity prices were obtained from a Team TELEPORT industry advisor, priced at \$0.03 per kWh.

Table 5.1.4
Costs of Electricity for Lithium Ion Intercalation Process

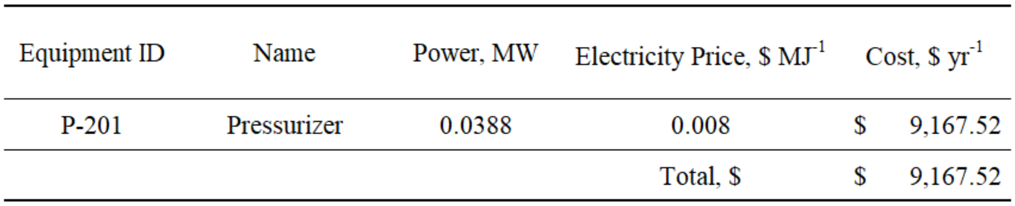

Equipment ID	Name	Power, MW	Electricity Price, \$ MJ^{-1}	Cost, \$ yr^{-1}
P-201	Pressurizer	0.0388	0.008	\$ 9,167.52
			Total, \$	\$ 9,167.52

5.2. ELECTRODIALYSIS

Because CAPCOST is unable to predict the costs associated with constructing and maintaining an electrolysis unit, calculations for the cost of the electrodialysis block were performed manually. The cost of construction materials for EL-301, summarized in Table 5.2.1, was estimated by creating correlations between geometries of plates of necessary materials available online and cost. This was then used to compute the cost for larger plates. The cost of raw materials needed to build the unit is presented in Table 5.2.1, which totaled approximately \$2.8 million. All electrodes and CEM membranes will be replaced on a yearly basis.

Table 5.2.1

Costs of Materials for Electrodialysis Unit

Material	Unit Price, $ per unit	Number of Units	Purchaed Materials Cost, $
Graphite Electrodes	$ 1,303.26	127	$ 165,514.00
Nickel Electrodes	$ 3,833.90	127	$ 486,905.00
Nafion 117 Membrane	$ 16,770.00	127	$ 2,129,790.00
HPDE Casing	$ 36,773.00	1	$ 36,773.00
		Total, $	$ 2,818,982.00

Battelle estimates that the equipment cost of a 10 kW fuel cell stack as $1,320 (Battelle, 2016). The fuel cell system used here utilizes 162 10 kW stacks, thus the total purchased equipment cost of the unit is approximately $213,000. The remainder of the equipment for this block, including all of the pumps, were priced using CAPCOST. The equipment capital costs for the electrodialysis process are summarized in Table 5.2.2.

Table 5.2.2

Costs of Equipment for Electrodialysis Process

Equipment ID	Name	Specifications	Material of Construction	Purchaced Equipment Cost, $
P-301	Brine Pressurizer	0.49 kW, 1.01 bar	Stainless Steel	$ 4,940.00
P-302	Water Pressurizer	0.67 kW, 1.01 bar	Stainless Steel	$ 4,940.00
P-303	Recycle Pressurizer	0.2 kW, 1.6 bar	Stainless Steel	$ 4,940.00
P-304	H2 Pressurizer	66.6 kW, 4 bar	Stainless Steel	$ 17,600.00
P-305	Air Pressurizer	146.65 kW, 4 bar	Stainless Steel	$ 29,000.00
EL-301	Electrodialysis Unit	127 cells	Graphite, Nickel, Nafion 117	$ 2,818,982.00
FC-301	Hydrogen Fuel Cell	162 cells	PFSA/PTFE, Platinum, Graphite, Aluminum	$ 212,889.60
			Total, $	$ 3,093,291.60
			Lang Factor Total, $	$ 11,228,648.51

Table 5.1.3 summarizes the utility costs for the electrolysis block. Cooling water is fed to the electrodialysis unit to counteract the waste heat generated from water formation. Again, the cooling water was priced using correlations developed by Ulrich et al. (2006).

Table 5.2.3

Costs of Utilities for Electrodialysis Process

Stream	Utility Type	Unit Price, \$ kg^{-1}	Feed Rate, kg hr^{-1}	Cost, \$ yr^{-1}
315	Cooling Water	0.00015	2,062,800	\$ 2,477,652.31
			Total, \$	\$ 2,477,652.31

Table 5.2.4 summarizes electricity costs for the electrodialysis block. The electrodialysis unit requires the application of voltage and current. The power requirement for the process is 2.54 MW, accounting for approximately 8.75% of the total power produced by the geothermal plant. Additional power requirements for this block are attributed to the five pumps that are used.

Table 5.2.4

Costs of Electricity for Electrodialysis Process

Equipment ID	Name	Power, MW	Electricity Price, \$ MJ^{-1}	Cost, \$ yr^{-1}
P-301	Brine Pressurizer	0.0005	0.008	\$ 115.89
P-302	Water Pressurizer	0.0007	0.008	\$ 158.47
P-303	Recycle Pressurizer	0.0002	0.008	\$ 47.30
P-304	H2 Compressor	0.0666	0.008	\$ 15,752.23
P-305	Air Compressor	0.1467	0.008	\$ 34,685.66
EL-301	Electrodialysis Unit	2.5800	0.008	\$ 610,221.60
			Total, \$	\$ 660,981.16

Because the fuel cell unit in this block produces electricity, it generates revenue. While the electricity generated here would not be sold, the fuel cell effectively generates revenue by reducing the amount of electricity consumed from the power plant. Because of this, the same unit price for consumed electricity was used to calculate the revenue. Table 5.2.5 summarizes the effective revenue from the fuel cell electricity.

Table 5.2.5

Revenue from Electricity for Electrodialysis Process

Equipment ID	Name	Power, MW	Electricity Price, $ MJ^{-1}	Revenue, $ yr^{-1}
FC-301	Hydrogen Fuel Cell	1.6128	0.008	$ 381,459.46
			Total, $	$ 381,459.46

5.3. CRYSTALLIZATION

Because pricing information for the rotary drum filter was not readily available from Komline-Sanderson, the unit was priced manually using sizing correlations from Towler and Sinnott (2013). The purchased equipment cost of the filtration unit can be estimated with:

$$C_e = a + bS^n \tag{E 5.3.1}$$

Where a and b are cost coefficients, n is an equipment specific exponent, and S is the size parameter, equal to the primary size dimension for equipment. In this case, the size parameter is equal to the filter area (0.87 m^2). The remainder of the equipment for this block, including the dryer unit, crystallizer, holding tanks, condenser, and pumps were priced using CAPCOST. The equipment capital costs for the crystallization process are summarized in Table 5.3.1.

Table 5.3.1

Costs of Equipment for Crystallization Process

Equipment ID	Name	Specifications	Material of Construction	Purchaced Equipment Cost, $	
P-401	Crystallizer Feed Pressurizer	0.5 kW, 2.29 bar	Stainless Steel	$	4,940.00
P-402	Filtrate Pressurizer	0.029 kW, 1.01 bar	Stainless Steel	$	4,940.00
V-401	Crystallizer	341 m^3	Stainless Steel	$	8,660.00
F-401	Rotary Drum Filter	26.4 W, 3 ft diamter, 1 ft width	Stainless Steel	$	16,366.00
D-401	Dryer	0.181 m^3/s, 1.01 bar	Stainless Steel	$	7,000.00
TK-401	Dry LiOH•H2O Tank	700 m^3	Stainless Steel	$	156,000.00
E-401	Steam Condenser/Cooler	314 m^2	Stainless Steel	$	77,800.00
			Total, $	$	275,706.00
			Lang Factor Total, $	$	1,000,812.78

Table 5.3.2 summarizes the cost of raw materials for the crystallization block, which only consists of the dry air fed to the dryer. Unlike the ambient air used for the fuel cell unit in the electrolysis block, which does not have an associated cost, the air used in the dryer unit does have an associated cost. This is because the air used in the dryer must be dry air, and thus must be pre-processed before being used in this system. Dry air was priced using correlations developed by Ulrich et al. (2006), similar to the methods used to price cooling water and low pressure steam.

Table 5.3.2

Cost of Raw Materials for Crystallization Process

Stream	Raw Material	Unit Price, $/kg	Feed Rate, kg/hr	Cost, $/yr	
416	Dry Air	0.05	542.1	$	203,322.51
			Total, $	$	203,322.51

Table 5.3.3 summarizes the utility costs for the crystallization block. Cooling water is used in E-401 to condense and cool the steam coming out of the crystallizer. Again, cooling water was priced using correlations developed by Ulrich et al. (2006).

Table 5.3.3

Costs of Utilities for Crystallization Process

Stream	Utility Type	Unit Price, $ kg^{-1}	Feed Rate, kg hr^{-1}	Cost, $ yr^{-1}
405	Cooling Water	0.00015	114,784	$ 137,868.35
			Total, $	$ 137,868.35

Table 5.3.4 summarizes the revenue associated with the main lithium hydroxide monohydrate product from the crystallization block. The market price used in these calculations was for lithium hydroxide monohydrate at the minimum purity specification to be considered battery-grade (56.5 wt%).

Table 5.3.4

Revenue from Products for Crystallization Process

Stream	Product	Unit Price, $ kg^{-1}	Production Rate, kg hr^{-1}	Revenue, $ yr^{-1}
417	LiOH•H2O	61.5	977	$ 473,714,082.00
			Total, $	$ 473,714,082.00

Table 5.3.5 summarizes electricity costs for the crystallization block. Electricity costs are associated with the two centrifugal pumps used to circulate the crystal slurry and the filtrate recycle, the hydraulic vacuum pump built into the rotary drum filter unit, and the dryer unit. Cost to heat the dryer air was excluded.

Table 5.3.5

Cost of Electricity for Crystallization Process

Equipment ID	Name	Power, MW	Electricity Price, $ MJ^{-1}	Cost, $ yr^{-1}
P-401	Crystallizer Feed Pressurizer	0.00050	0.008	$ 118.26
P-402	Filtrate Pressurizer	0.00003	0.008	$ 6.86
F-401	Rotary Drum Filter	0.00003	0.008	$ 6.24
D-401	Dryer	0.02500	0.008	$ 5,913.00
			Total, $	$ 6,044.36

5.4. REVERSE OSMOSIS WATER TREATMENT

Because pricing for the FilmTecTM SW30HR-320 membranes and 8-E-1200-1M-to-8M-R6 pressure vessels was not readily available, pricing for the RO units was done by using the total unit pricing calculated from a previous project which used the same equipment at a larger scale. This project involved using reverse osmosis to desalinate sea water and used 733 RO units (1 RO unit = 1 pressure vessel + 7 membranes) for a total equipment price of $65 million. In our process, we are only using 27 RO units, thus the total purchased equipment price for the RO units is around $2.4 million, or $270,000 for each 9 unit series. The remainder of the equipment for this block, including the holding tanks, pumps, and coolers were priced using CAPCOST. The equipment capital costs for the reverse osmosis process are summarized in Table 5.4.1.

Table 5.4.1

Costs of Equipment for Reverse Osmosis Water Treatment Process

Equipment ID	Name	Specifications	Material of Construction	Purchaced Equipment Cost, $
P-501	Water Pressurizer	1085 kW, 82 bar	Stainless Steel	$ 217,000.00
RO-501	RO Pressure Vessel Series 1	9 RO units, 82 bar	Stainless Steel, Polyamide Membrane	$ 266,030.01
RO-502	RO Pressure Vessel Series 2	9 RO units, 82 bar	Stainless Steel, Polyamide Membrane	$ 266,030.01
RO-503	RO Pressure Vessel Series 3	9 RO units, 82 bar	Stainless Steel, Polyamide Membrane	$ 266,030.01
TK-501	Post-Wash Holding Tank	11,400 m^3	Stainless Steel	$ 835,000.00
TK-502	Permeate Tank	113,700 m^3	Stainless Steel	$ 7,104,366.37
E-501	Wash Cooler	1,219 m^2	Stainless Steel	$ 226,000.00
			Total, $	$ 9,180,456.41
			Lang Factor Total, $	$ 33,325,056.77

Table 5.4.2 summarizes the utility costs for the reverse osmosis block. Cooling water is used in E-501 to cool the dirty wash water coming out of the lithium intercalation reactors. Again, cooling water was priced using correlations developed by Ulrich et al. (2006).

Table 5.4.2

Costs of Utilities for Reverse Osmosis Water Treatment Process

Stream	Utility Type	Unit Price, $ kg^{-1}	Feed Rate, kg hr^{-1}	Cost, $ yr^{-1}
501	Cooling Water	0.00015	1,139,307	$ 1,368,434.47
			Total ($)	$ 1,368,434.47

Table 5.3.4 summarizes the revenue associated with the permeate product, which is sold as deionized water, a precursor for potable drinking water. The market price used in these calculations was derived from Turton et al. (2018).

Table 5.4.3

Revenue from Products for Reverse Osmosis Water Treatment Process

Stream	Product	Unit Price, $ kg^{-1}	Production Rate, kg hr^{-1}	Revenue, $ yr^{-1}
512	DI Water	0.00053	157,503	$ 658,129.44
			Total, $	$ 658,129.44

Table 5.4.4 summarizes electricity costs for the reverse osmosis block. Electricity costs are associated with the large centrifugal pump used to pressurize the dirty wash water going into the RO units from 0.6 bar to 82 bar.

Table 5.4.4

Cost of Electricity for Reverse Osmosis Water Treatment Process

Equipment ID	Name	Power, MW	Electricity Price, $ MJ^{-1}	Cost, $ yr^{-1}
P-501	Water Pressurizer	1.08500	0.008	$ 256,624.20
			Total, $	$ 256,624.20

5.5. MISCELLANEOUS

Land

The price of land was estimated by taking 2% of the total equipment capital cost, yielding a one-time payment of $2.61 million (Anderson, personal communication, 2023).

Labor

Labor costs were taken from an OPEX cost template provided by industrial partners of Team TELEPORT. This document details the salaries and positions that the implementation of the lithium extraction plant would introduce. Each plant employee is expected to work 2,080 hours per year, resulting in a total yearly cost of labor of $5,310,240.

Depreciation

As equipment ages, it begins to lose its value as it undergoes wear and tear from use. Depreciation charges are a form of tax allowance that accounts for this loss of value in fixed capital investments including process equipment (Towler & Sinnott, 2013). Depreciation rates can be calculated in a number of ways, including straight-line and declining-balance methods. A double declining-balance depreciation calculation was used here to help account for higher cash flows in the startup and early operation of the lithium extraction plant. Double declining balance can be modeled using the following equation:

$$D_m = C(1 - F_d)^{m-1} F_d \qquad \text{(E 5.3.1)}$$

Where D_i is the depreciation charge in year *m*, *C* is the depreciable value after 20 years, and F_d represents the fixed annual depreciation charge. In the case of double declining-balance, F_d will be equal to *2*/*n*, or 0.1 based on a plant lifespan of 20 years. It was assumed that all process equipment will be worth nothing and scrapped at the end of the 20 year cycle, yielding a *C* value of $130,709,962.

Working Capital

Working capital is “the amount of capital required to start up the plant and finance the first few months of operation before revenues from the process starts” (Turton, 2018). For this plant, it was estimated to be 20% of the total equipment capital costs, which is $26.1 million.

Taxes

As of 2023, the federal corporate tax rate on profits is 21%. The California state corporate tax rate for 2023 is 8.84%. This results in a total tax rate of 29.84% on the plant’s annual profits. Despite revenue of the plant being constant, the yearly amount of owed taxes increases over time due to the varying levels of depreciation during the lifetime of the plant.

5.6. SUMMARY

Table 5.6.1 summarizes the total fixed costs, operating costs, and revenue for each process block, as well as miscellaneous sections. If the cost of the calcium citrate feed is included, our total operating costs exceed our revenue, meaning that the plant will never become profitable. If this cost is excluded, the operating cost of the lithium intercalation block is reduced to $70.6 million per year, which reduces the total plant operating cost to $82,694,962. This operating cost value is used in the following section for the cash flow analysis.

Table 5.6.1

Economic Summary of Geothermal Lithium Extraction Plant

Section	Fixed Costs. $	Operating Costs, $\$\ \text{yr}^{-1}$	Revenue, $\$\ \text{yr}^{-1}$
Silicate Treatment & Power Cycle	$ (475,530.00)	$ (1,674,194.15)	$ -
Lithium Ion Intercalation	$ (84,679,914.00)	$ (615,857,041.16)	$ -
Electrodialysis	$ (11,228,648.51)	$ (3,138,633.46)	$ 381,459.46
Crystallization	$ (1,000,812.78)	$ (347,235.23)	$ 473,714,082.00
Reverse Osmosis Water Treatment	$ (33,325,056.77)	$ (1,625,058.67)	$ 658,129.44
Land	$ (2,614,199.24)	$ -	$ -
Labor	$ -	$ (5,310,240.00)	$ -
Working Capital	$ (26,141,992.41)	$ -	$ -
Total	$ (159,466,153.71)	$ (627,952,402.68)	$ 474,753,670.89

5.7. ECONOMIC ANALYSIS

To decide whether the plant is economically viable without the use of citrate, the IRR must be calculated. First, discrete cash flows, summarized in Table 5.7.1, were calculated for each year of the 20 year operating life of the plant.

Table 5.7.1

20-year Discrete Cash Flow of Geothermal Lithium Extraction Plant

Year	Expenses	Depreciation	Revenue	Profit	Taxes	Cash Flow
0	$ (159,466,153.71)	$ -	$ -	$ (159,466,153.71)		$ (159,466,153.71)
1	$ (82,694,962.68)	$ (13,070,996.21)	$ 474,753,670.89	$ 378,987,712.01	$ (113,089,933.26)	$ 278,968,774.95
2	$ (82,694,962.68)	$ (10,587,506.93)	$ 474,753,670.89	$ 381,471,201.29	$ (113,831,006.46)	$ 278,227,701.75
3	$ (82,694,962.68)	$ (7,718,292.55)	$ 474,753,670.89	$ 384,340,415.66	$ (114,687,180.03)	$ 277,371,528.18
4	$ (82,694,962.68)	$ (5,063,971.74)	$ 474,753,670.89	$ 386,994,736.47	$ (115,479,229.36)	$ 276,579,478.85
5	$ (82,694,962.68)	$ (2,990,224.67)	$ 474,753,670.89	$ 389,068,483.54	$ (116,098,035.49)	$ 275,960,672.73
6	$ (82,694,962.68)	$ (1,589,127.99)	$ 474,753,670.89	$ 390,469,580.22	$ (116,516,122.74)	$ 275,542,585.48
7	$ (82,694,962.68)	$ (760,074.99)	$ 474,753,670.89	$ 391,298,633.22	$ (116,763,512.15)	$ 275,295,196.06
8	$ (82,694,962.68)	$ (327,187.36)	$ 474,753,670.89	$ 391,731,520.85	$ (116,892,685.82)	$ 275,166,022.39
9	$ (82,694,962.68)	$ (126,759.09)	$ 474,753,670.89	$ 391,931,949.13	$ (116,952,493.62)	$ 275,106,214.60
10	$ (82,694,962.68)	$ (44,198.16)	$ 474,753,670.89	$ 392,014,510.05	$ (116,977,129.80)	$ 275,081,578.41
11	$ (82,694,962.68)	$ (13,869.85)	$ 474,753,670.89	$ 392,044,838.36	$ (116,986,179.77)	$ 275,072,528.45
12	$ (82,694,962.68)	$ (3,917.26)	$ 474,753,670.89	$ 392,054,790.96	$ (116,989,149.62)	$ 275,069,558.59
13	$ (82,694,962.68)	$ (995.71)	$ 474,753,670.89	$ 392,057,712.50	$ (116,990,021.41)	$ 275,068,686.80
14	$ (82,694,962.68)	$ (227.79)	$ 474,753,670.89	$ 392,058,480.43	$ (116,990,250.56)	$ 275,068,457.66
15	$ (82,694,962.68)	$ (46.90)	$ 474,753,670.89	$ 392,058,661.32	$ (116,990,304.54)	$ 275,068,403.68
16	$ (82,694,962.68)	$ (8.69)	$ 474,753,670.89	$ 392,058,699.52	$ (116,990,315.94)	$ 275,068,392.28
17	$ (82,694,962.68)	$ (1.45)	$ 474,753,670.89	$ 392,058,706.77	$ (116,990,318.10)	$ 275,068,390.12
18	$ (82,694,962.68)	$ (0.22)	$ 474,753,670.89	$ 392,058,708.00	$ (116,990,318.47)	$ 275,068,389.75
19	$ (82,694,962.68)	$ (0.03)	$ 474,753,670.89	$ 392,058,708.19	$ (116,990,318.52)	$ 275,068,389.69
20	$ (82,694,962.68)	$ (0.00)	$ 474,753,670.89	$ 392,058,708.21	$ (116,990,318.53)	$ 275,068,389.68

Figure 5.7.1 shows a plot of the discrete cash flows from Table 5.7.1.

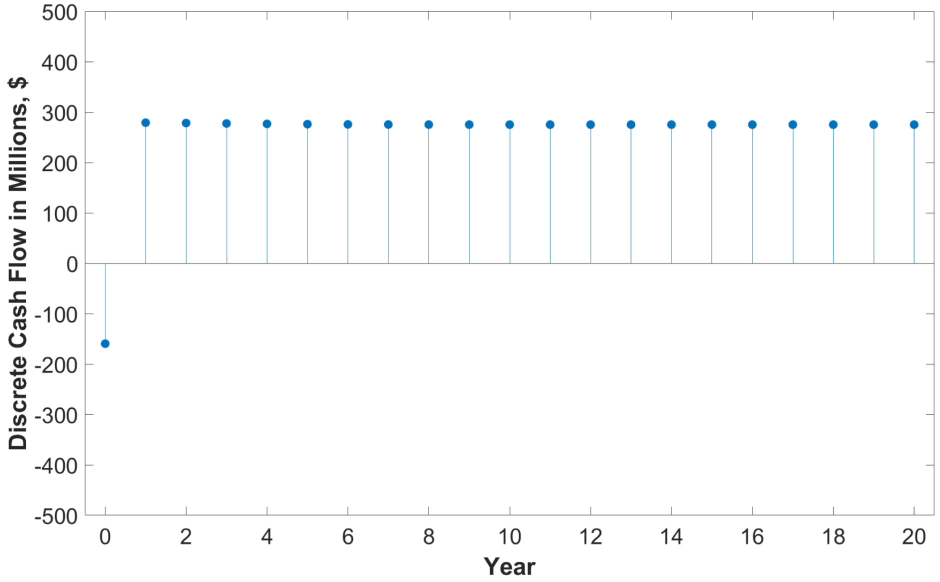

Figure 5.7.1: *20-year Discrete Cash Flow Diagram*

Figure 5.7.2 shows a plot of the cumulative cash flows, which sums the discrete cash flows for the current and all previous years. The plot shows that the plant is expected to break even after 1 operating year.

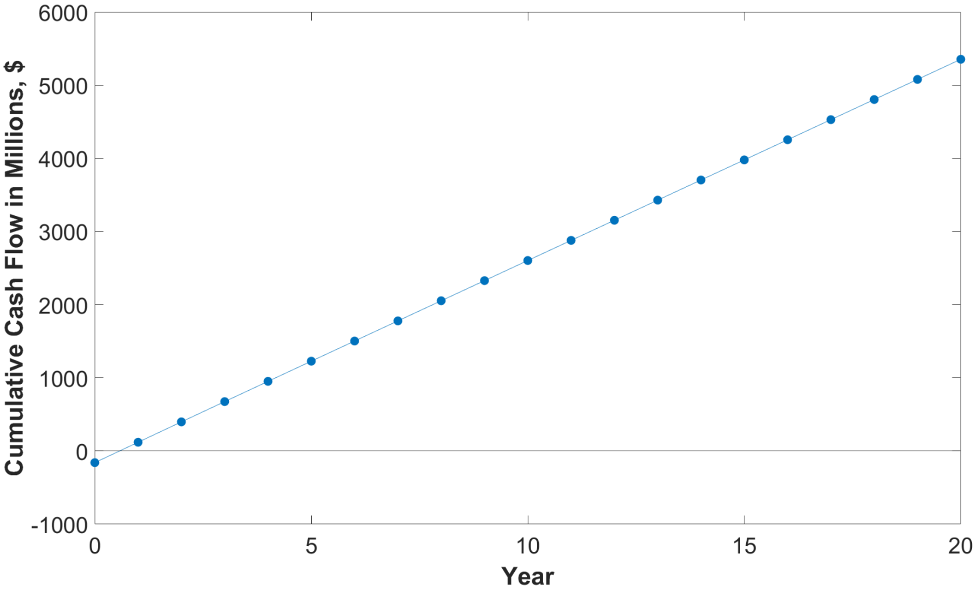

Figure 5.7.2: *20-year Cumulative Cash Flow Diagram*

Finally, using the theory of net present value (NPV) of money, the IRR can be calculated with:

$$NPV = \frac{CF}{(1-r)^n} \tag{E 5.7.1}$$

Where r is the IRR, n is the number of years, and CF is the corresponding discrete cash flow at year n. In order to calculate the IRR, the NPV of all the discrete cash flows over the 20-year period must sum to \$0. Using Microsoft Excel's Goal Seek function, the IRR was calculated to be 175%, which is considered a good investment. However, it is important to recognize that this analysis excludes the cost of the calcium citrate feed, which in this design would result in the operating costs exceeding the operating revenue from the plant. Therefore, in order for this process to be economically viable, it is important that research is done to either 1) lower the amount of calcium citrate needed to facilitate the lithium intercalation process, 2) recover the calcium citrate so that it can be recycled, or 3) find other materials with a lower cost that could substitute calcium citrate.

6. ENVIRONMENTAL, SAFETY, AND SOCIAL CONSIDERATIONS

6.0 ENVIRONMENTAL

As the United States modernizes the electric grid, battery storage in the form of lithium-ion batteries is crucial to making the innovation sustainable. In order to store renewable energy at sites where wind and solar energy production is high and prepare it for redistribution, it is necessary to continue accelerating battery storage technology (Polsky & Layke, 2022). According to the International Energy Agency (IEA), lithium-ion batteries are the preferred choice for grid-scale storage, and the price of these batteries will be largely influenced by the cost of lithium production (IEA, 2022). Additionally, for the application of lithium-ion batteries in the transportation sector through electric vehicles, there are additional environmental benefits. Electric vehicles, powered by lithium-ion batteries, have zero direct emissions from their tailpipes and overall have lower carbon emissions in their lifetimes compared to conventionally powered vehicles (U.S. Department of Energy, Energy Efficiency & Renewable Energy, n.d.). All of these factors outline the environmental motivation for the novel lithium extraction process described above.

The environmental impact of the geothermal power plant and the lithium extraction process is a concern despite the relatively clean process of producing geothermal energy. Throughout the process, steps with higher levels of environmental concern are scrutinized below to ensure as minimal negative impact as possible.

Water usage is a high priority of the system since the geothermal power plant will be situated in the desert in the Salton Sea region of California. The reverse osmosis system included in the process will help purify water to a level that can be sold as well as recycled back to the system for use in other process steps, potentially in the electrodialysis block and the wash water for the lithium intercalation reactors. Condensed water coming from the power generation step could also be used for the wash water needed for the reactors or sold off directly as long as the levels of HCl are appropriate. Since the design is conscious of water usage, it is not expected for the plant to consume extreme amounts of water from the surrounding area. Typically, the water usage in geothermal plants does have a negative impact on farmers and other local communities, but with careful monitoring and design choices, much of this environmental consequence can be mitigated.

Depleted sodium rich brine will be reinjected into the geothermal well after it moves through the lithium intercalation reactors. Analysis of aquifers have shown that a minimum of 50% of spent brine is required to be reinjected in order to maintain plant viability and prevent land subsidence in the area (Sanyal & Enedy, 2011). Since only 30% of the brine will be vaporized in the power generation process, around 70% of the brine will be reinjected into the well, preventing any negative environmental impacts from the health of the well.

6.1 SAFETY CONCERNS

Although the geothermal power plants this process is designed to work with are already established, there are several hazards associated with geothermal energy. One of the most prominent risks comes with the installation of pipes and pumps used to bring the brine up to the surface. During installation and drilling, unsupported structures and soil are prone to collapse, which can cause damage to equipment and fatalities (OSHA, n.d.). Another common hazard is associated with the hot geothermal brine and production of high pressure steam. Accidental releases can result in severe burns and even fatalities to unprotected workers.

There are a multitude of chemical hazards specific to this process design. HCl used in silica pretreatment is highly corrosive and can cause severe chemical burns to an exposed person.

Additionally, HCl can corrode metal pipes and pump seals, which can result in loss of containment. LiOH is highly caustic and also causes severe chemical burns to exposed persons. Additionally, the production of dry LiOH•H_2O can pose a dust hazard if the particles are small enough. Dusts are hazardous as they can cause lung irritation if inhaled. Side products produced in the electrodialysis reactor are also hazardous, including H_2, which is flammable and potentially explosive. $FePO_4$ and calcium citrate are mild irritants and can pose a significant threat after long-term exposure.

Beyond chemical hazards, there are also block specific hazards, particularly in the electrodialysis block. Electrical current being passed through the electrodialysis cells present an electrocution hazard to workers. Short circuits can lead to electrical fires and potentially explosions. Flash vessels used in the steam generation can become overpressurized and rupture. Finally, the crystallization reaction that occurs in the crystallization block is extremely exothermic and, if uncontrolled, can lead to hot spot generation and potentially loss of containment due to overpressurization.

6.2 SOCIAL IMPACT

The addition of a lithium extraction unit to a geothermal plant has the potential to generate economic benefits such as job creation and stimulation of related business and support services. It is estimated that the plant would create approximately 63 jobs. These jobs created by the lithium extraction plant are not limited to direct personnel working at the field but also involve service related jobs necessary for site management. The addition of a lithium recovery process within the scope of a geothermal power plant has potential to increase the attractiveness of renewable energy as well. With the ongoing transition towards cleaner energy sources and increasing demand for electric vehicles, this project can contribute to the competitiveness of the renewable energy industry as a whole. This can in turn help to promote a low-carbon economy and reduce dependence on fossil fuels.

7. CONCLUSIONS AND RECOMMENDATIONS

7.0 CONCLUSIONS

After assessing the economic, environmental, and social impacts of a retrofitted lithium extraction plant in the Salton Sea, California, we believe that the technology developed by team TELEPORT has great promise, but there are currently too many uncertainties to recommend immediate construction of the facility. Though initial analysis suggests that the plant could be profitable, we do not believe that construction should begin until further research is performed on citrate. Future *go/no go* decisions will hinge upon the development of new methods to replace or reduce citrate needs to cut down plant material costs. Potential payoffs are high enough to warrant further research and development of this process.

When calcium citrate is not accounted for in the economic analysis, an IRR of 175% was found, suggesting that building this plant is a good investment. Projected profits from lithium hydroxide monohydrate, potable water, and fuel cell electricity are estimated to be $474 million, $658,000, and $318,000 respectively. Each of these processes contribute to the plant's profits with 99.8% stemming from the extraction of lithium from brine. With increasing demand for energy-dense materials, our plant would help fill in gaps in lithium supply. We recommend that further research be conducted so that we can better assess the feasibility of implementing a lithium extraction process in the Salton Sea.

7.1 RESEARCH RECOMMENDATIONS

Further research is required to validate assumptions and provide a more accurate prediction of how the plant will operate. Firstly, alternatives to calcium citrate must be explored to reduce costs. The addition of this non-recoverable oxidizing agent in bulk would prove unprofitable, and a cheaper alternative must be found. Accounting for the use of a different oxidizing agent or recovery of calcium citrate between cycles would provide a better economic analysis of the plant and could impact the *go/no go* decision. Further research is also required to determine the influence of temperature and pH on the intercalation step; currently, data is only provided at 25℃. Cooling the brine to this temperature would be both costly and energy intensive, and higher temperatures of sorption are desirable. Selectivity of the intercalation material also must be studied to provide better estimates for lithium production. Current studies only provide selectivity information based on a brine composed of 50% Na^+ and 50% Li^+. This is not an acceptable substitute for the brine composition, where Na^+ concentration greatly outweighs the Li^+ concentration. It is imperative that these factors be further investigated so that more realistic models can be produced to estimate Na^+ to Li^+ ratios in the intercalation step. Electrodialysis kinetics and mass transfer should be studied in greater detail to provide better predictions of how the process may work; membranes must be analyzed over different concentration and temperature ranges to gauge CEM performance. Further research recommendations are summarized in the bullet points below:

- Find alternatives to or recycle/reduce citrate
- Study pH and temperature ranges for the lithium intercalation step
- Provide more data regarding mass transfer and kinetics for the lithium intercalation step
- Study selectivity of Li/Na based on more realistic brine concentrations
- Further research electrodialysis kinetics and mass transfer
- Study concentration and temperature data for the electrodialysis step

7.2 PROJECT RECOMMENDATIONS

There are a number of processes that could potentially improve the economics of the system. Though $LiOH•H_2O$ is currently in higher demand than lithium carbonate, Li_2CO_3, the addition of a process unit to convert LiOH into the alternative product may be profitable as battery technologies change over time. It may also prove to be worthwhile to collect other products from the brine, such as rubidium or cesium, to sell as coproducts. These materials might be removed through extraction techniques using 4-*tert*-butyl-2-(α-methylbenzyl)phenol (t-BAMBP) as a solvent, which can be readily synthesized with t-butyl phenol (tBP) and styrene (Zhang et al., 2014). Though these species are present in minute amounts, their high market prices could make up for relatively small yields. Other products present in high amounts with lower values could also be extracted, including zinc, manganese, or potassium. To reduce $FeCl_3$ costs and produce an additional product, it may be advantageous to add another electrodialysis block to process waste brine leaving the secondary reactor as the primary reactor is unloaded. This electrolysis block would create NaOH rather than LiOH and regenerate the $FeCl_3$ for reuse in the system, which could reduce makeup iron costs. The NaOH solution could then be processed further or sent back down the geothermal well depending on economic viability. Another alternative is to integrate more recycle streams into the process; for example, a small recycle stream from brine leaving the primary reactor can be cycled back upstream. Considering the significant cooling requirements for the RO inlet, distillation could be studied as an alternative to separate ions from water, ultimately allowing for the comparison of their economics.

ACKNOWLEDGEMENTS

We would like to thank Professors Geoffrey Geise, Gaurav Giri, and Gary Koenig of the University of Virginia Chemical Engineering Department, along with team TELEPORT for sponsoring this project and assisting with the design of the lithium intercalation reactors as well as the electrodialysis units. We would also like to thank Professor Eric Anderson for guidance throughout this project.

REFERENCES

Ambrose, H., Kendall, A. (2020). Understanding the future of lithium: Part 1, resource model. *Journal of Industrial Ecology*. *24*(1)80–89. https://doi.org/10.1111/jiec.12949.

Arim, A. L., Neves, K., Quina, M. J., & Gando-Ferreira, L. M. (2018). Experimental and mathematical modelling of Cr(III) sorption in fixed-bed column using modified pine bark. *Journal of Cleaner Production*, *183*, 272–281. https://doi.org/10.1016/j.jclepro.2018.02.094

Azevedo, M., Baczynska, M., Hoffman, K., & Krauze, A. (2022). *How lithium mining is fueling the EV revolution | McKinsey*. Retrieved January 30, 2023, from https://www.mckinsey.com/industries/metals-and-mining/our-insights/lithium-mining-how-new-production-technologies-could-fuel-the-global-ev-revolution

Battelle (2016, October). *Manufacturing Cost Analysis of PEM Fuel Cell Systems for 5- and 10-kW Backup Power Applications*. Energy.gov. https://www.energy.gov/eere/fuelcells/articles/manufacturing-cost-analysis-pem-fuel-cell-systems-5-and-10-kw-backup-power

Carta, G. (2021). *Heat and Mass Transfer for Chemical Engineers: Principles and Applications*. McGraw-Hill .

Chemical Engineering World (2020, November). *Reverse Osmosis Process Principle*. https://chemicalengineeringworld.com/reverse-osmosis-process-principle/

Davis, Mark E. and Davis, Robert J. (2003) *Fundamentals of chemical reaction engineering.* McGraw-Hill , New York, NY. ISBN 007245007X.

Dupont. (2019, November). FilmTecTM SW30XLE-440i Element. Dupont.

Phan, A. T., Gheribi, A. E., & Chartrand, P. (2019). Modelling of phase equilibria of $LiFePO_4$ ‑$FePO_4$ olivine join for cathode material. *The Canadian Journal of Chemical Engineering*, *97*(8), 2224–2233. https://doi.org/10.1002/cjce.23416

Emissions from Electric Vehicles. Alternative Fuels Data Center. N.d. https://afdc.energy.gov/vehicles/electric_emissions.html

Fogler, H. S. (1986). *Elements of Chemical Reaction Engineering* (6th ed.). Prentice-Hall.

Fritzmann, C., Löwenberg, J., Wintgens, T., Melin, T. (2007). State-of-the-art of reverse osmosis desalination, *Desalination*, *216*(1-3), 1-76. https://doi.org/10.1016/j.desal.2006.12.009

Fuller, Thomas F. Harb, John N.. (2018). *Electrochemical Engineering - 14.1 Overview of Industrial Electrolysis.* John Wiley & Sons. Retrieved from https://app.knovel.com/hotlink/pdf/id:kt011IBAH1/electrochemical-engineering/overview-industrial-electrolysis

GEA. (n.d.). *Forced circulation crystallizers*. GEA Engineering for a Better World. Retrieved March 2, 2023, from https://www.gea.com/en/products/evaporators-crystallizers/solution-crystallization-plants/forced-crystallization-crystallizer.jsp

Geothermal energy. (n.d.). Retrieved April 11, 2023, from https://wiki.aapg.org/Geothermal_energy

Graber, T. A., Morales, J. W., Robles, P. A., Galleguillos, H. R., & Taboada, M. E. (2008). Behavior of LiOH·H2O crystals obtained by evaporation and by drowning out. *Crystal Research and Technology*, *43*(6), 616–625. https://doi.org/10.1002/crat.200711110

Grageda, M., Gonzalez, A., Quispe, A., & Ushak, S. (2020). Analysis of a Process for Producing Battery Grade Lithium Hydroxide by Membrane Electrodialysis. *Membranes*, *10*(9), Article 9. https://doi.org/10.3390/membranes10090198

Guerra, C., & Jacobo, P. (2012, March). PH Modifications for Silica Control in Geothermal Fluids. *Short Course on Geothermal Development and Geothermal Wells*. United Nations University Geothermal Training Programme, Santa Tecla, El Salvador. https://orkustofnun.is/gogn/unu-gtp-sc/UNU-GTP-SC-14-39.pdf

Gupta, D., Zhang, Y., Nie, Z., Wang, J., & Koenig Jr, G. M. (2022). Chemical redox of lithium-ion solid electroactive material in a packed bed flow reactor. *Chemical Engineering Science*, *251*, 117443. https://doi.org/10.1016/j.ces.2022.117443

Hoeflinger, J., & Hofmann, P. (2020). Air mass flow and pressure optimisation of a PEM fuel cell range extender system. *International Journal of Hydrogen Energy*, *45*(53), 29246–29258. https://doi.org/10.1016/j.ijhydene.2020.07.176

IEA (2022), *Grid-Scale Storage*, IEA, Paris https://www.iea.org/reports/grid-scale-storage

Komline-Sanderson. (n.d.). Rotary Drum Vacuum Filter. *Komline-Sanderson*. Retrieved March 2, 2023, from https://www.komline.com/products/rotary-drum-vacuum-filter/

LennTech. (2017). 8-E-1200-1M-to-8M-R6. LennTech.

McCabe, Warren L., 1899-1982. (2001). *Unit operations of chemical engineering*. Boston: McGraw Hill

McCabe, W. L., Smith, J. C., & Harriot, P. (1993). *Unit Operations of Chemical Engineering* (5th ed.). McGraw-Hill.

McManamay, J. (2022, August 11). *UVA team to compete in final round of Doe's clean-energy technology competition*. University of Virginia School of Engineering and Applied Science. Retrieved March 20, 2023, from https://engineering.virginia.edu/uva-team-compete-final-round-doe%E2%80%99s-clean-energy-technology-competition

Monnin, C., & Dubois, M. (2005). Thermodynamics of the LiOH + H2O System. *Journal of Chemical & Engineering Data*, *50*(4), 1109–1113. https://doi.org/10.1021/je0495482

NIST. (2021). *Water.* https://webbook.nist.gov/cgi/cbook.cgi?ID=C7732185&Mask=2

O'Brien, T., Bommaraju, T., & Hine, F. (2005). *Handbook of Chlor-Alkali Technology* (Vol. 1). Springer. https://virginia.app.box.com/file/1139175500121

Occupational Safety and Health Administration (OSHA) (n.d.). *Geo-thermal Energy*. Green Job Hazards. https://www.osha.gov/green-jobs/geo-thermal

Peters, M. S., Timmerhaus, K. D., & West, R. E. (2006). Heuristics for Process Equipment Design. In *Plant Design and Economics for Chemical Engineers* (pp. 974–981). essay, McGraw-Hill.

Polsky, M., & Layke, J. (2022). What's needed to modernize America's electricity grid? Retrieved from https://www.wri.org/insights/whats-needed-modernize-us-electricity-grid

Sanyal, S., & Enedy, S. (2011). Fifty years of power generation at the Geysers geothermal field, California - the lessons learned. Retrieved from https://es.stanford.edu/ERE/pdf/IGAstandard/SGW/2011/sanyal3.pdf

Taboada, M. E., Graber, T. A., Cisternas, L. A., Cheng, Y. S., & Ng, K. M. (2007). Process Design for Drowning-Out Crystallization of Lithium Hydroxide Monohydrate. *Chemical Engineering Research and Design*, *85*(9), 1325–1330. https://doi.org/10.1205/cherd06251

Towler, G. P., & Sinnott, R. K. (2013). *Chemical engineering design: Principles, practice and economics of plant and process design, second edition* (2nd ed.). Butterworth-Heinemann.

Tremaine, P., & Xiao, C. (1999). *Enthalpies of formation and heat capacity functions for maricite, NaFePO4(cr), and sodium iron(III) hydroxy phosphate, Na3Fe(PO4)2·(Na4/3H2/3O)(cr)* -. https://www.sciencedirect.com/science/article/abs/pii/S0021961499905426

Turton, R. (2012). *Analysis, Synthesis, and Design of Chemical Processes* (5th ed.). Pearson.

Ulrich, G. D., & Vasudevan, P. T. (2006, April 15). How to Estimate Utility Costs. *Chemical Engineering*. https://terpconnect.umd.edu/~nsw/chbe446/HowToEstimateUtilityCosts-UlrichVasudevan2006.pdf

U.S. Department of Energy, Energy Efficiency & Renewable Energy. (n.d.). *Emissions from electric vehicles*. Alternative Fuels Data Center: Emissions from Electric Vehicles. Retrieved March 24, 2023, from https://afdc.energy.gov/vehicles/electric_emissions.html

U.S. Department of Energy. (n.d.). *Hydrogen Storage*. Energy.gov. Retrieved April 11, 2023, from https://www.energy.gov/eere/fuelcells/hydrogen-storage

Ventura, S., Bhamidi, S., Hornbostel, M., Nagar, A., & Perea, E. (2016). *Selective Recovery of Metals from Geothermal Brines* (DOE-SRI-6747). SRI International, Menlo Park, CA (United States). https://doi.org/10.2172/1336270

Warren, I. (2021). *Techno-Economic Analysis of Lithium Extraction from Geothermal Brines* (NREL/TP-5700-79178). National Renewable Energy Lab. (NREL), Golden, CO (United States). https://doi.org/10.2172/1782801

Zhang, N., Gao, D. L., Liu, M. M., & Deng, T. L. (2014). Rubidium and Cesium Recovery from Brine Resources. *Advanced Materials Research*, *1015*, 417–420. https://doi.org/10.4028/www.scientific.net/AMR.1015.417.

APPENDIX A - SUPPLEMENTARY FIGURES & TABLES

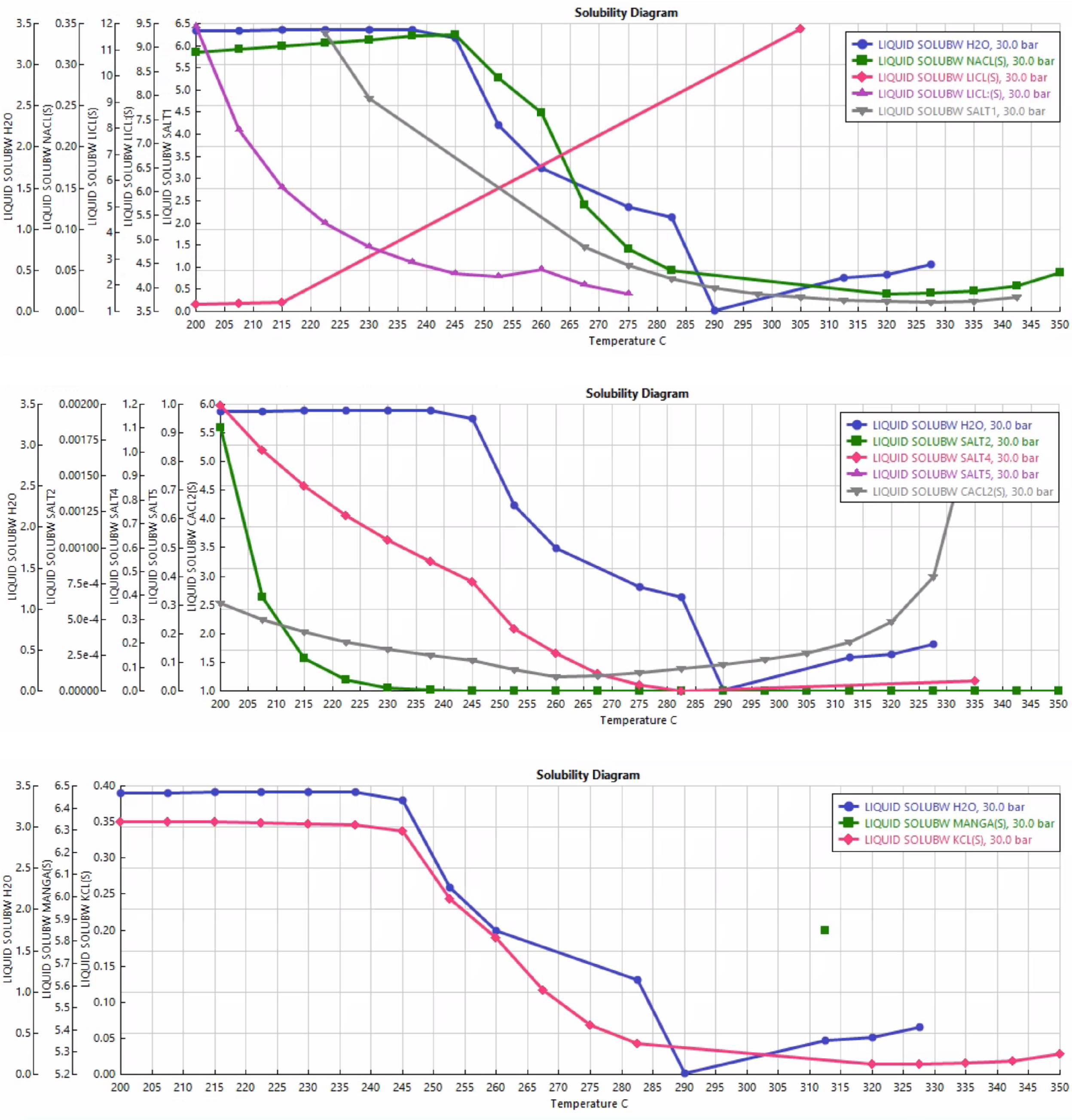

Figure A.0: *Solubility Curves for Brine Components, generated by Aspen*

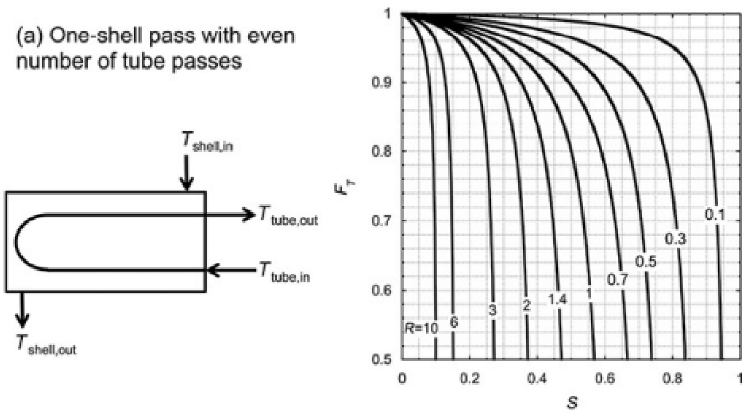

Figure A.1: *Plot from Carta (2021) used to find Heat Exchanger Correction Factor*

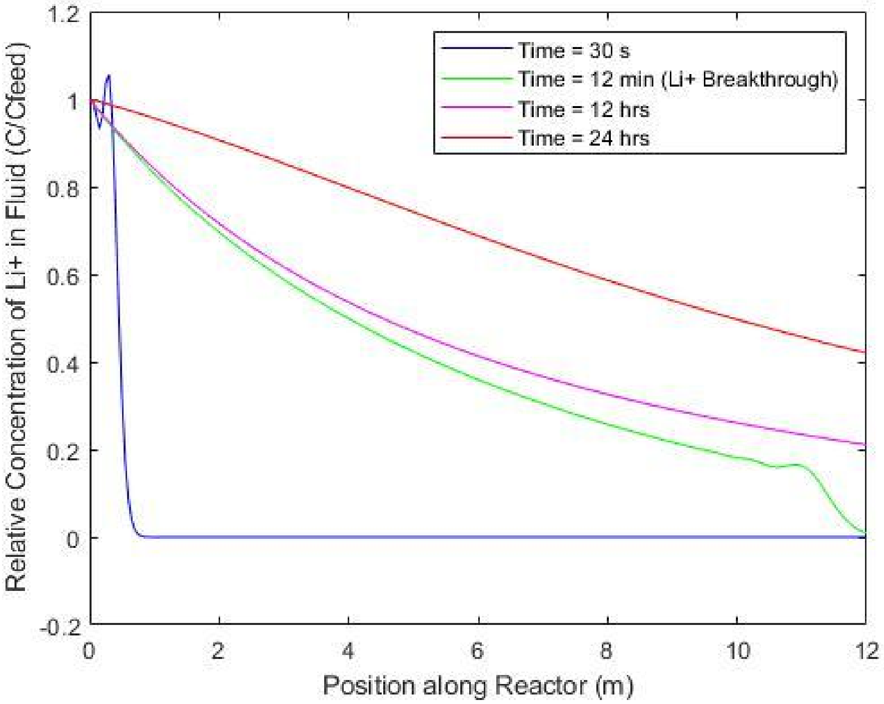

Figure A.2: *Breakthrough Curves of Li^+ in Primary Intercalation Reactor*

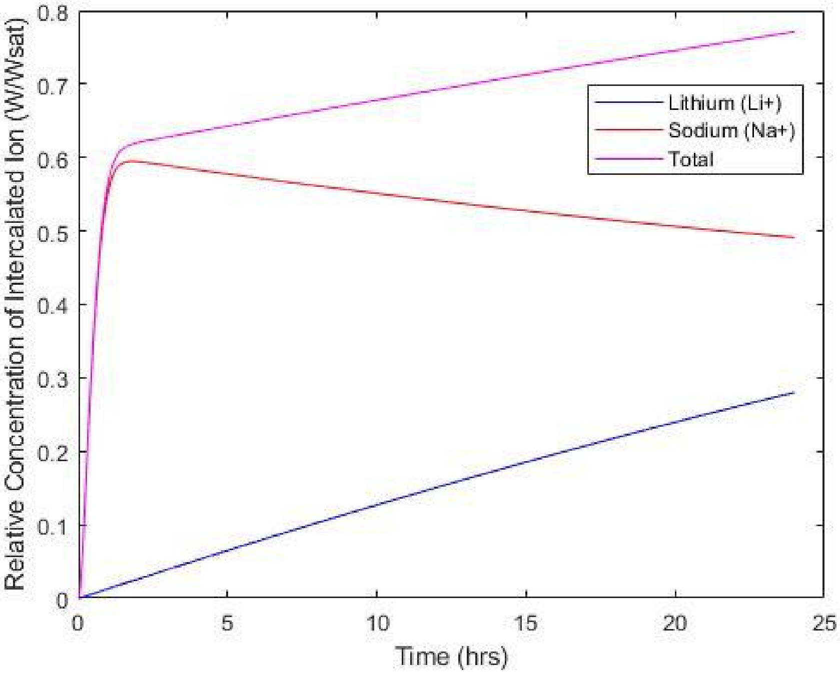

Figure A.3: *Bed Saturation Curves for Li*$^+$ *and Na*$^+$ *in Primary Intercalation Reactor*

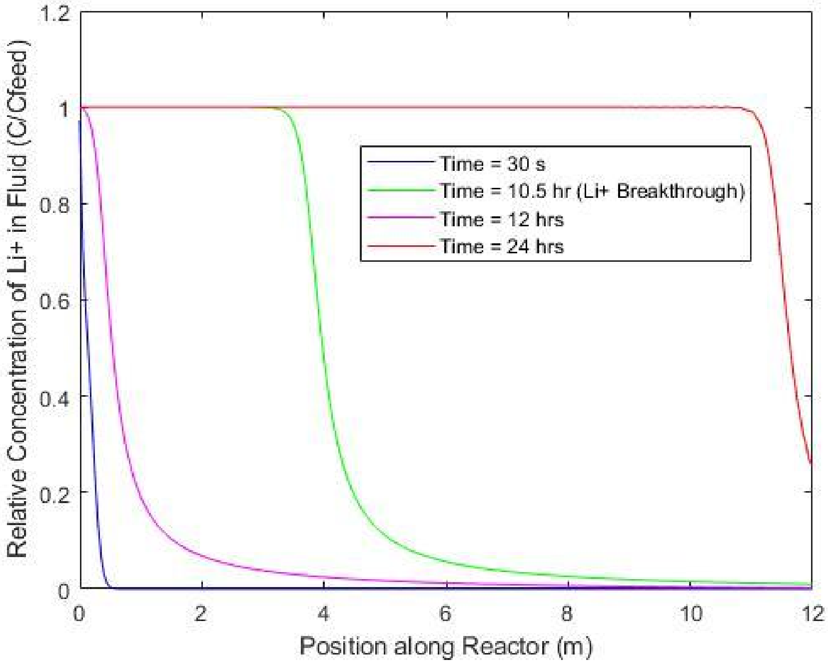

Figure A.4: *Breakthrough Curves of Li*$^+$ *in Secondary Intercalation Reactor*

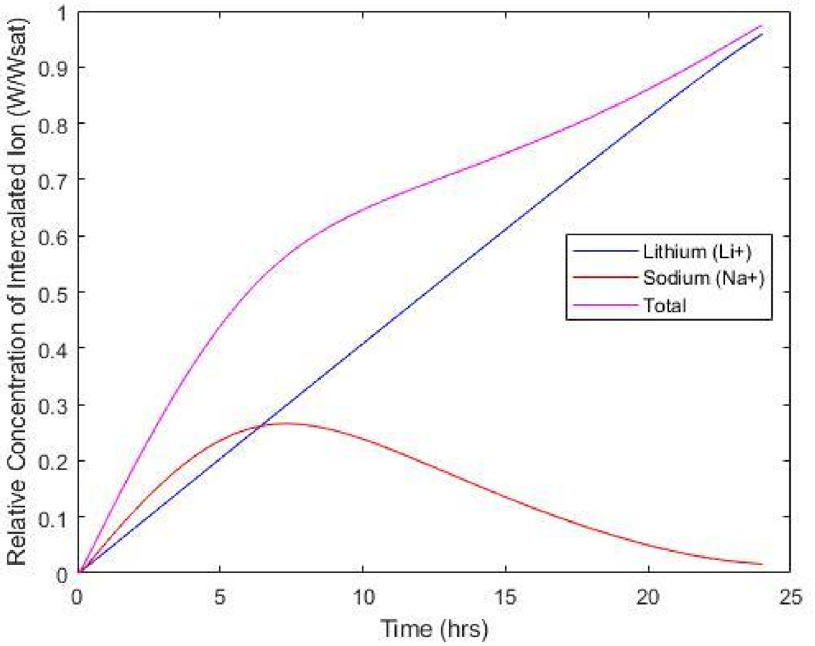

Figure A.5: *Bed Saturation Curves for* Li^+ *and* Na^+ *in Primary Intercalation Reactor*

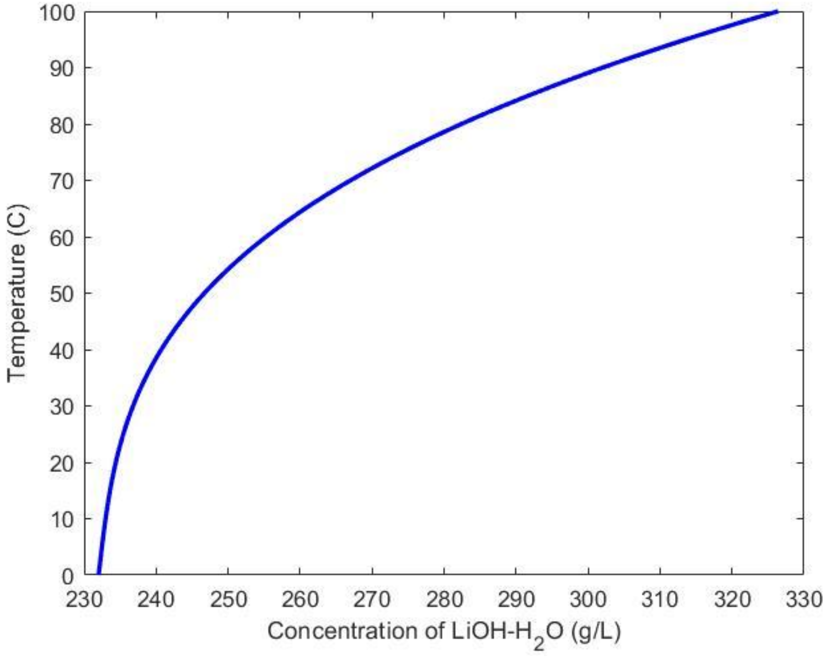

Figure A.6: *Solubility Curve for Lithium Hydroxide Monohydrate*

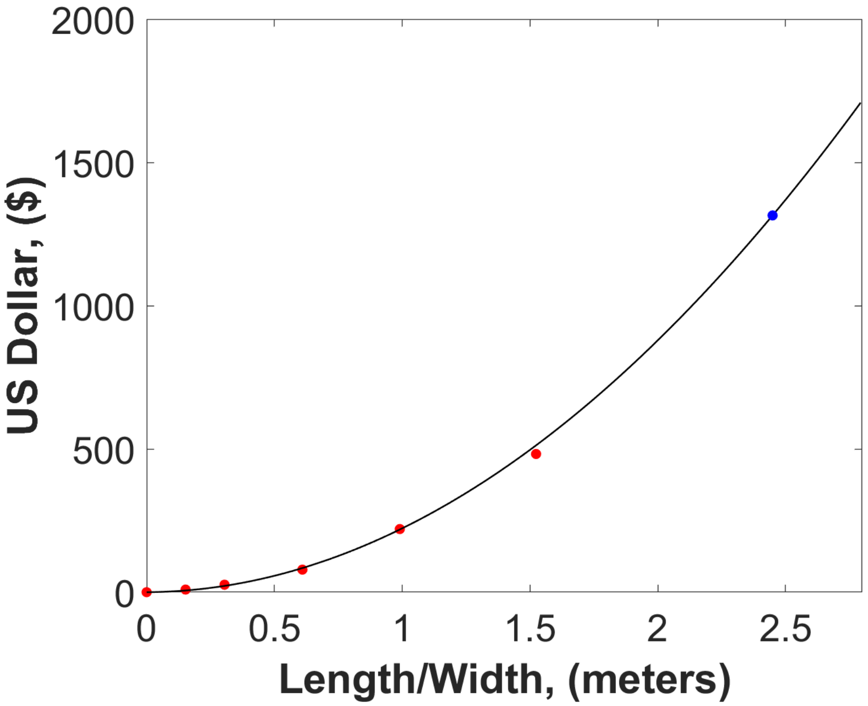

Figure A.7: *Sample Graphite Cost Correlation for Electrodialysis Materials Cost Estimation*

Table A.0

Species and Streams used in the calculation of Molar Concentration for Reverse Osmosis

Component	Mass Flowrate, kg hr^{-1}	Molar Mass, g mol^{-1}	Molar Flow Rate, mol hr^{-1}
HCL	22.00	36.46	603.40
H_3O^+	224.75	19	11828.79
Li^+	8.74	7	1248.97
Na^+	2,258.56	23	98198.35
K^+	680.00	39	17435.83
Ca^{2+}	64.18	40.1	1600.58
$Mn2^+$	1,356.53	54.94	24691.03
Fe^{2+}	79.10	55.85	1416.32
Cl^-	6,446.71	35.45	181853.59
SiO_2	14.09	60.08	234.45
$Ca_3(C_6H_5O_7)_2$	1,363.46	498.5	2735.13
		Total, mol hr^{-1}	341846.45
		Volumetric Flowrate, L hr^{-1}	315637
		Concentration, mol L^{-1}	1.08

Table A.1

Pricing Sources of Materials

Material	Unit Price, \$ kg^{-1}	Source
Calcium Citrate	1.3	Made-in-China
Iron (III) Chloride	0.45	Made-in-China
Iron (III) Phosphate	4.00	Alibaba
Lihtium Hydroxide Monohydrate	61.5	London Metal Exchange
Deionized Water	0.00053	Turton et al.
Cooling Water	0.000152	Ulrich et al.
Low Pressure Steam	0.0613	Ulrich et al.
Dry Air	0.0476	Ulrich et al.

APPENDIX B - SAMPLE CALCULATIONS

B.0 EQUIPMENT SIZING/OPERATING CONDITIONS CALCULATIONS

Hydraulic Power Used by a Pump

m = 964,694 kg hr^{-1}	Total mass flowrate of stream 201
ρ = 1,210 kg m^{-3}	Density of stream 201
ΔP = 1.4 bar	Pressure differential across pump P-201
η = 0.8	Pump efficiency

$$p = \frac{m}{\rho}\Delta P\eta^{-1} = \frac{964{,}694\,\frac{kg}{hr}}{1{,}210\,\frac{kg}{m^3}}(\frac{1\,hr}{3{,}600\,s})(1.4\,bar)(\frac{10^5\,Pa}{1\,bar})(0.8)^{-1}(\frac{1\,kW}{1{,}000\,W}) = 38.76\ \text{kW}$$

Contact Area between Hot and Cold Streams in a Heat Exchanger

Q_t = 17,660,488 W	Total heat duty
$T_{in,h}$=$T_{shell,in}$= 72.95 ºC	Hot inlet temperature
$T_{in,c}$=$T_{tube,in}$= 10 ºC	Cold inlet temperature
$T_{out,h}$=$T_{shell,out}$= 25 ºC	Hot outlet temperature
$T_{out,c}$=$T_{tube,out}$= 25 ºC	Cold outlet temperature
U_o= 2750 W m^{-2} K^{-1}	Overall heat transfer coefficient
$h_{d,i}$= 4000 W m^{-2} K^{-1}	Tube side fouling coefficient
$h_{d,o}$= 4000 W m^{-2} K^{-1}	Shell side fouling coefficient
r_o= 0.025 m	Outer radius of pipe
L= 7.32 m	Pipe Length

$$U_{o,d} = (\frac{1}{U_o} + \frac{1}{h_{d,i}}\frac{r_o}{r_i} + \frac{1}{h_{d,o}})^{-1} = (\frac{1}{2750\,\frac{W}{m^2\cdot K}} + \frac{1}{4000\,\frac{W}{m^2\cdot K}}\frac{.025\,m}{.025\,m} + \frac{1}{4000\,\frac{W}{m^2\cdot K}})^{-1}$$

$= 562.5$ W m^{-2} K^{-1}

$$\Delta T_{lm} = \frac{(T_h^{in} - T_c^{out}) - (T_h^{out} - T_c^{in})}{ln\frac{T_h^{in} - T_c^{out}}{T_h^{out} - T_c^{in}}} = \frac{(72.95^oC - 25^oC) - (25^oC - 10^oC)}{ln\frac{(72.95^oC - 25^oC)}{(25^oC - 10^oC)}} = 28.35\text{ K}$$

$$S = \frac{T_{tube,out} - T_{tube,in}}{T_{shell,in} - T_{tube,in}} = \frac{25^oC - 10^oC}{72.95^oC - 10^oC} = 0.238$$

$$R = \frac{T_{shell,in} - T_{shell,out}}{T_{tube,out} - T_{tube,in}} = \frac{72.95^oC - 25^oC}{25^oC - 10^oC} = 3.2$$

$$F(S, R) \rightarrow 0.92$$

$$A_o = \frac{Q}{U_{o,d}\Delta T_{lm}F(S,R)} = \frac{17660488\, W}{(562.5\, \frac{W}{m^2 \cdot K})(28.35\, K)(0.92)} = 1203.6\text{ m}^2$$

Holding Tank/Silo Sizing

V = 6,744,385 L	Maximum volume of collected wash water
V_{tank} = ? m^3	Total tank volume

$$V_{tank} = 1.5V = 1.5(6,744,385\, L)(\frac{1\, m^3}{1000\, L}) = 10,117\text{ m}^3$$

Flash Vessel/Crystallizer Sizing

t= 0.125 hr	Hold up time
m= 1,252,580 kg hr^{-1}	Mass flow rate of stream 103
ρ= 912 kg m^{-3}	Density of stream 103
ρ_l= 961 kg m^{-3}	Density of stream 105
ρ_v= 18.2 kg m^{-3}	Density of stream 104
m_l= 1,102,071 kg hr^{-1}	Mass flow rate of stream 105
m_v= 142,847 kg hr^{-1}	Mass flow rate of stream 104

$$V = 2 \times \frac{m \times t}{\rho} = 342\, m^3$$

$$D_{tank} = \sqrt[3]{\frac{2V}{3\pi}} = \sqrt[3]{\frac{2(342\, m^3)}{3\pi}} = 4.17\, m$$

$$F_{lv} = \frac{\dot{m}_L}{\dot{m}_V}\sqrt{\frac{\rho_V}{\rho_L}} = \frac{(1{,}102{,}071\, kg\, hr^{-1})}{(142{,}847\, kg\, hr^{-1})}\sqrt{\frac{(18.2\, kg\, m^{-3})}{(961\, kg\, m^{-3})}} = 1.0635$$

$$K = e^{-1.877 - 0.814 lnF_{lv} - 0.187(lnF_{lv})^2 - 0.0145(lnF_{lv})^3 - 0.00102(lnF_{lv})^4} =.1454\, m/s$$

$$\mu = K\sqrt{\frac{\rho_L - \rho_V}{\rho_V}} = (.1454)\sqrt{\frac{(961\, kg\, m^{-3} - 18.2\, kg\, m^{-3})}{(18.2\, kg\, m^{-3})}} = 3{,}761\, m\, hr^{-1}$$

$$A = \frac{\dot{m}_V}{\rho_V \times \mu} = \frac{(142{,}847\, kg\, hr^{-1})}{(18.2\, kg\, m^{-3})(3{,}761\, m\, hr^{-1})} = 2.08\, m^2$$

$$D = \sqrt{\frac{4A}{\pi}} = \sqrt{\frac{4(2.08\, m^2)}{\pi}} = 1.63\, m$$

Diffusion Parameters used in the Modeling of the Lithium Intercalation Reactors

u_0 = 0.01 m s^{-1}	Superficial velocity of brine moving through primary reactor
d_s = 0.002 m	Radius of iron (III) phosphate particles
ρ_f = 1,080 kg m^{-3}	Density of brine moving through primary reactor
μ_f = 0.0019 Pa s	Dynamic viscosity of brine moving through primary reactor
Re = ?	Reynold's number of brine moving through primary reactor
D_{ax} = ? m^2 s^{-1}	Axial dispersion coefficient
d_{pore} = 500 nm	Pore diameter of iron (III) phosphate particles
T = 353 K	Reactor operating temperature
$M_{W, L}$ = 6.941 g mol^{-1}	Molar mass of Li^+
$D_{k, L}$ = 1.03*10^{-9} m^2 s^{-1}	Knudsen diffusivity of Li^+

$D_{H2O,\,L} = 1.03*10^{-9}$ m^2 s^{-1}	Diffusivity of Li^+ in water
$D_{pore,\,L}$ = ? m^2 s^{-1}	Pore diffusivity of Li^+
$\phi = 0.5$	Porosity of iron (III) phosphate particles
$\tau = 4$	Tortuosity of iron (III) phosphate particles
$D_{eff,\,L}$ = ? m^2 s^{-1}	Effective diffusivity of Li^+ in iron (III) phosphate particles

$$Re = \frac{u_0 d_s \rho_f}{\mu_f} = \frac{(0.01\,\frac{m}{s})(0.002\,m)(1{,}080\,\frac{kg}{m^3})}{(0.0019\,Pa\,s)} = 12.77$$

$$D_{ax} = u_0 d_s (0.11 Re^{0.4} + 0.2)^{-1} = (0.01\,\frac{m}{s})(0.002\,m)(0.11(12.77)^{0.4} + 0.2)^{-1}$$

$$= 3.49 * 10^{-5} \text{ m}^2 \text{ s}^{-1}$$

$$D_{k,L} = 4.85 * 10^{-8}(d_{pore})(\frac{T}{M_{w,\,i}})^{0.5} = 4.85 * 10^{-8}(500\,nm)(\frac{353\,K}{6.941\,\frac{g}{mol}})^{0.5}$$

$$= 1.73 * 10^{-4} \text{ m}^2 \text{ s}^{-1}$$

$$D_{pore.\,L} = (\frac{1}{D_{k,L}} + \frac{1}{D_{H2O,\,L}})^{-1} = (\frac{1}{3.49*10^{-5}\,\frac{m^2}{s}} + \frac{1}{1.73*10^{-4}\,\frac{m^2}{s}})^{-1} = 1.03 * 10^{-9} \text{ m}^2 \text{ s}^{-1}$$

$$D_{eff.\,L} = \frac{\phi}{\tau} D_{pore,L} = \frac{0.5}{4}(1.03 * 10^{-9}\,\frac{m^2}{s}) = 1.29 * 10^{-10} \text{ m}^2 \text{ s}^{-1}$$

Redox Equilibrium Parameters used in the Modeling of the Lithium Intercalation Reactors

E^o_{red} = 0.410 V	Standard reduction potential of $Fe^{3+}PO_4$ to $LiFe^{2+}PO_4$
E^o_{ox} = 0.244 V	Standard reduction potential of Fe^{2+} to Fe^{3+} in the presence of citrate ions
E^o_{cell} = ? V	Standard cell potential
$\frac{[Fe^{3+}]}{[Fe^{2+}]} = 99$	Molar ratio of Fe^{3+} to Fe^{2+} ions in solution

R = 8.314 J mol^{-1} K^{-1}	Ideal gas constant
T = 353 K	Reactor operating temperature
n = 1	Molar ratio of electrons transferred in redox reaction
F = 96,485 C mol^{-1}	Faraday's constant
E_{cell} = ? V	Nernst cell potential
ΔG = ? J mol^{-1}	Gibbs free energy change of the redox reaction
$K_{eq,\,L}$ = ?	Equilibrium constant for Li^+ capture in iron (III) phosphate
S = 0.0082	Capture selectivity of Na^+ relative to Li^+
$K_{eq,\,N}$ = ?	Equilibrium constant for Na^+ capture in iron (III) phosphate

$$E^{o}_{cell} = E^{o}_{red} - E^{o}_{ox} = 0.410\,V - 0.244\,V = 0.166\,V$$

$$E_{cell} = E^{o}_{cell} - \frac{RT}{nF} ln(\frac{[Fe^{3+}]}{[Fe^{2+}]}) = 0.166\,V - \frac{(8.314\frac{J}{mol\,K})(353\,K)}{(1)(96{,}485\frac{C}{mol})} ln(\frac{1}{99}) = 0.306\ \text{V}$$

$$\Delta G = -\,nFE_{cell} = -\,(1)(96,485\frac{C}{mol})(0.306\,V) = -\,29,502\ \text{J mol}^{-1}$$

$$K_{eq,\,L} = exp(\frac{-\Delta G}{RT}) = exp(\frac{-(-29{,}502\,\frac{J}{mol})}{(8.314\frac{J}{mol\,K})(353\,K)}) = 23,210$$

$$K_{eq,\,N} = \frac{S}{1-S} K_{eq,\,L} = \frac{0.0082}{1-0.0082}(23,210) = 192$$

Lithium Intercalation Outlet Temperature Prediction (Primary Capture)

$\dot{m}_{in}$ = 964,696 kg hr^{-1}	Inlet mass flow rate of brine to primary reactor
$\dot{n}_{in}$ = 1,100,000 kmol day^{-1}	Inlet mole flow rate of brine to primary reactor per cycle
$\dot{m}_{Li,cap}$ = 175.5 kg hr^{-1}	Captured lithium in the primary reactor
$\dot{n}_{Li,int}$ = 601.7 kmol day^{-1}	Captured lithium in primary reactor per cycle in moles
$\dot{m}_{Na,cap}$ = 1011 kg hr^{-1}	Captured sodium in the primary reactor

$\dot{n}_{Na,int}$ = 1055 kmol day^{-1}	Captured sodium in primary reactor per cycle in moles
$\dot{m}_{out}$ = 963,510 kg hr^{-1}	Outlet mass flow rate of brine from primary reactor (to well)
$\dot{n}_{out}$ = 1,098,343 kmol day^{-1}	Outlet mole flow rate of brine from primary reactor per cycle
$C_{p,brine}$ = 60.72 kJ kmol^{-1} K^{-1}	Heat capacity of brine estimated within Aspen v11 (constant)
$\Delta_f H^{\theta}_{LiFePO_4}$ = -1616 kJ mol^{-1}	Heat of formation of the capture of lithium
$\Delta_f H^{\theta}_{FePO_4}$ = -1279 kJ mol^{-1}	Heat of formation of intercalation material
$\Delta_f H^{\theta}_{Li^+}$ = -279 kJ mol^{-1}	Heat of formation of aqueous lithium ion
$\Delta_f H^{\theta}_{NaFePO_4}$ = -1572 kJ mol^{-1}	Heat of formation of the capture of sodium
$\Delta_f H^{\theta}_{Na^+}$ = -240 kJ mol^{-1}	Heat of formation of aqueous sodium ion

$$\Delta_r H^{\theta} = \sum_{prod} v_i \, \Delta_f H^{\theta}_i - \sum_{rxt} v_i \Delta_f H^{\theta}_i$$

$$\Delta_r H^{\theta}_{Li,cap} = -1616 - (-279 - 1279) = -58 \text{ kJ mol}^{-1}$$

$$\Delta_r H^{\theta}_{Na,cap} = -1572 - (-240 - 1279) = -53 \text{ kJ mol}^{-1}$$

$$Q_{in} = Q_{out}$$

$$\dot{n}_{in} C_{p,brine} (T_{in} - T_{ref}) = \dot{n}_{out} C_{p,brine} (T_{out} - T_{ref}) + \dot{n}_{Li,cap} \Delta_R H^{\theta}_{Li,cap} + \dot{n}_{Na,cap} \Delta_R H^{\theta}_{Na,cap}$$

$$1,100,000 * 60.72 * (80 - 25) + 602 * 1000\,(58) + 1055 * 1000 * (53)$$

$$= 1,098,343 * 60.72 * (T_{out} - 25)$$

$$T_{out} = 81.5 \text{ °C}$$

Lithium Intercalation Reactor Sizing

$V_{tot} = 0.22\ \mathrm{m^3\ s^{-1}}$	Total volumetric flowrate of brine to primary reactor
$u_0 = 0.01\ \mathrm{m\ s^{-1}}$	Superficial velocity of brine moving through primary reactor
$d_t = 4\ \mathrm{in} = 0.1016\ \mathrm{m}$	Tube diameter
$n_{tubes} = ?$	Number of tubes for primary reactor
$L = 12\ \mathrm{m}$	Length of primary reactor
$\varepsilon = 0.6$	Void fraction of primary reactor bed
$d_s = 0.002\ \mathrm{m}$	Radius of iron (III) phosphate particles
$Re = 12.77$	Reynold's number of brine moving through primary reactor
$\Delta P = ?\ \mathrm{bar}$	Pressure differential across primary reactor
$V_R = ?\ \mathrm{m^3}$	Total volume of primary reactor
$\rho_s = 3{,}056\ \mathrm{kg\ m^{-3}}$	Density of iron (III) phosphate
$m_s = ?$ tonnes	Total mass of iron (III) phosphate in primary reactor

$$n_{tubes} = \frac{4V_{tot}}{\pi u_0 d_t^2} = \frac{4(0.22\ \frac{m^3}{s})}{\pi(0.01\ \frac{m}{s})\ (0.1016\ m)^2} = 2,715$$

$$\Delta P = L(\frac{1-\varepsilon}{\varepsilon^3})(1 + \frac{2d_s}{3(1-\varepsilon)d_t})^2(\frac{1.75}{1+\frac{2d_s}{3(1-\varepsilon)d_t}} + 150\frac{1-\varepsilon}{Re})$$

$$= (12\ m)(\frac{1-0.6}{0.6^3})(1 + \frac{2(0.002\ m)}{3(1-0.6)(0.1016\ m)})^2(\frac{1.75}{1+\frac{2(0.002\ m)}{3(1-0.6)(0.1016\ m)}} + 150\frac{1-0.6}{12.77})(\frac{1\ bar}{10^5\ Pa})$$

$$= 0.0015\ \text{bar}$$

$$V_R = n_{tubes}L(\frac{\pi}{4}u_0 d_t^2) = (2,715)(12\ m)(\frac{\pi}{4}(0.01\ \frac{m}{s})\ (0.1016\ m)^2) = 264.17\ \mathrm{m^3}$$

$$m_s = \rho_s(1-\varepsilon)V_R = (3,056\ \frac{kg}{m^3})(1-0.6)(264.17\ m^3)(\frac{1\ tonne}{1000\ kg}) = 322.9\ \text{tonnes}$$

Electrodialysis Unit Sizing

$\dot{m}$ = 24,063 mol hr^{-1}	Total molar flowrate of lithium in stream 214
n = 2	Molar ratio of electrons transferred in electrolysis reaction
F = 96,485 C mol^{-1}	Faraday's constant
I = ? A	Total current required for electrolysis reaction
i = 1,700 A mol^{-2}	Current density
A_T = ? m^2	Total electrode area
A_c = 6 m^2	Total area of a single electrode in a cell
n_c = ?	Number of cells
C_p = ? m^{-1}	Cell pitch
A_{lab} = 24 cm^2	Total area of an electrode
Δ_{lab} = 4 cm	Center to center distance between electrodes of same charge in a lab scale cell
$\Delta_{industry}$ = ? m	Center to center distance between electrodes of same charge in a industrial scale cell
a_r = ? m^{-1}	Electrode area per unit volume of cell
V_t = ? m^3	Total volume of electrodialysis unit

$$I = n\dot{m}F = (2)(24,063\frac{mol}{hr})(\frac{1\ hr}{3600\ s})(96,485\frac{C}{mol}) = 1.29 * 10^6 \text{ A}$$

$$A_T = \frac{I}{i} = \frac{1.29*10^6\ A}{1,700\frac{A}{m^2}} = 761 \text{ m}^2$$

$$n_c = \frac{AT}{A_c} = \frac{761\ m^2}{6\ m^2} = 127 \text{ cells}$$

$$\frac{A_{lab}}{\Delta_{lab}^2} = \frac{A_c}{\Delta_{industry}^2} \rightarrow \frac{24\ cm^2}{(4\ cm)^2} = \frac{5\ m^2}{\Delta_{industry}^2} \rightarrow \Delta_{industry} = 2 \text{ m}$$

$$C_P = (\Delta_{industry})^{-1} = (2\ m)^{-1} = 0.5\ \mathrm{m}^{-1}$$

$$\mathrm{a_r} = 2(0.5\ \mathrm{m}^{-1}) = 1\ \mathrm{m}^{-1}$$

$$V_t = \frac{\dot{\mathrm{m}}}{\eta_f \times \frac{ia_r}{nF}} = \frac{24{,}063\ mol\ hr^{-1} \times \frac{1\ hr}{3{,}600\ s}}{1 \times \frac{1{,}700\ C\ s^{-1}\ m^{-2} * 1\ m^{-1}}{2(96{,}485\ C\ mol^{-1})}} = 761\ \mathrm{m}^3$$

Rotary Drum Filtration Unit Sizing

$m_s = 0.2715$ kg s^{-1}	Mass flowrate of LiOH•H_2O in stream 409
$V_s = 4.41*10^{-4}$ m^3 s^{-1}	Volumetric flowrate of stream 409
$m_F = 0.2718$ kg s^{-11}	Total mass flowrate of stream 414
$\rho = 1{,}149.24$ kg m^{-3}	Density of stream 410
c = ? kg m^{-3}	Mass of LiOH•H_2O deposited on filter cloth per unit volume of filtrate
$m_{solid} = 0.2713$ kg s^{-1}	Mass flowrate of LiOH•H_2O in stream 414
a_o = 6 m kg^{-1}	Specific cake resistance
$\mu = 0.2882*10^{-3}$ Pa s	Viscosity of water at 100°C
ΔP = 101,325 Pa	Pressure difference across filter cloth
$s = 0.2$	Compressibility coefficient
$f = 0.3725$	Submerged fraction of filter drum
$n = 0.25$ s^{-1}	Rotational frequency of filter drum
A = ?	Area of filter cloth required to achieve desired recovery of solid

$$c = \left(\frac{m_s}{V_s}\right)\left(1 - \left(\frac{m_F}{m_s} - 1\right)\frac{m_s}{V_s \rho}\right)^{-1}$$

$$= (\frac{0.2715\ \frac{kg}{s}}{4.41*10^{-4}\ \frac{m^3}{s}})(1\ -\ (\ \frac{0.2718}{0.2715\ \frac{kg}{s}}\ -\ \ 1)\frac{0.2715\ \frac{kg}{s}}{(4.41*10^{-4}\ \frac{m^3}{s})(1{,}149.24\frac{kg}{m^3}\ )})^{-1}\ =\ 616.53\ \text{kg m}^{-3}$$

$$A\ = m_{solid}(\frac{a_0\mu}{2c\Delta P^{1-s}fn})^{0.5}\ =\ (0.2713\ \frac{kg}{s})(\frac{(1.95*10^{10}\ \frac{m}{kg})(0.2822*10^{-3}\ Pa\ s)}{2(616.53\frac{kg}{m^3})(101{,}325\ Pa)^{1-0.2}(0.3725)(0.25\frac{1}{s})})^{0.5}$$

$$=\ 0.591\ \text{m}^2 = 6.356\ \text{ft}^2 \rightarrow 9.4\ \text{ft}^2\ \text{(nearest filter size)}$$

Dryer Unit Sizing

Q_{ary} = 22.74 kW	Heat duty of dryer
H_{air}= 151.02 kJ kg^{-1}	Enthalpy of air at 150°C
m_{air} = 0.2715 kg s^{-1}	Mass flowrate of air required

$$m_{air}\ =\ \frac{Q_{dry}}{H_{air}}\ =\ \frac{22.74\ kW}{151.02\ \frac{kJ}{kg}}\ (\frac{3600\ s}{1\ hr})\ =\ 542.07\ \text{kg hr}^{-1}$$

Lithium Intercalation Wash Water Outlet Temperature Prediction

m_{R1} = 639,369 kg	Mass of brine in primary reactors
m_{R2}= 196,614 kg	Mass of brine in secondary reactors
m_W = 6,724,152 kg	Mass of wash water in secondary reactors
C_P = 4,184 J kg^{-1} °C^{-1}	Heat capacity of water
T_{R1} = 80°C	Initial temperature of streams in primary reactors and wash water
T_{R2} = 50°C	Initial temperature of streams in secondary reactors
T_F = ?	Final temperature of wash stream exiting reactors

$$m_{R1}C_p(T_F - T_{R1})\ +\ m_{R2}C_P(T_F - T_{R2})\ +\ m_wC_p(T_F - T_{R1})\ =\ 0$$

$$(639,369\ kg)(4,184\ \frac{J}{kg\ °C})(T_F - 80\ °C) + (196,614\ kg)(4,184\ \frac{J}{kg\ °C})(T_F - 50\ °C) + (6,724,152\ kg)(4,184\ \frac{J}{kg\ °C})(T_F - 80\ °C) = 0$$

Using Microsoft Excel Goal Seek → T_F = 79.2°C

---

*Reverse Osmos*is *Unit Sizing*

$r = 0.5$	Total permeate recovery rate for RO system
$i = 2$	Van't Hoff index
$C = 1.08$ mol L^{-1}	Molar concentration of solute in stream 505
$R = 8.314$ J mol^{-1} K^{-1}	Ideal gas constant
$T = 298$ K	Operating temperature of RO units
$\Pi = ?$ bar	Maximum operating pressure of RO units
$Q_T = 3,787,640$ L day^{-1}	Total volumetric flowrate of permeate (stream 512)
$Q_A = 23,000$ L day^{-1}	Single element exiting volumetric flowrate
$r_E = 0.08$	Single element recovery rate
$N_E = ?$	Total number of RO elements
$P_E = 7$	Number of RO elements per pressure vessel
$N_v = ?$	Total number of pressure vessels

$$\Pi = (1 + r)iCRT = (1 + 0.5)(2)(1.08\ \frac{mol}{L})(8.314 \frac{J}{mol\ K})(298\ K)(\frac{1000\ L}{1\ m^3})(\frac{1\ bar}{10^5\ Pa})$$

$$= 80.5\ \text{bar}$$

$$N_E = \frac{Q_T}{(1-r_E)Q_A} = \frac{3.787,640\ \frac{L}{day}}{(1-0.08)(23,000)\ \frac{L}{day}} = 179\ \text{elements}$$

$$N_v = \frac{N_E}{P_E} = \frac{179}{7} = 26\ \text{vessels}$$

B.1 ECONOMIC ANALYSIS CALCULATIONS

Cooling Water Pricing using CEPCI and Fuel Cost Correlation

$m = 1{,}508{,}655$ kg hr^{-1}	Total mass flowrate of cooling water used in the entire process
$\rho = 995.65$ kg m^{-3}	Density of water at 30°C
$V = ?$ m^3 s^{-1}	Total volumetric flowrate of cooling water used in the entire process
$a = ?$	Utility cost coefficient for cooling water as describe by Ulrich et al. (2006)
$b = 0.003$	Utility cost coefficient for cooling water as describe by Ulrich et al. (2006)
$CEPCI = 800$	Chemical Engineering Plant Cost Index for 2022
$S_f = 16.05$ \$ GJ^{-1}	Specific price of natural gas in Southern California (EIA, 2023)
$C_V = ?$	Specific price of cooling water on a volume basis
$C_m = ?$	Specific price of cooling water on a mass basis

$$V = \frac{m}{\rho} = \frac{1{,}508{,}655\,\frac{kg}{hr}}{995.65\,\frac{kg}{m^3}}\left(\frac{1\,hr}{3600\,s}\right) = 0.421\ \mathrm{m^3\,s^{-1}}$$

$$a = 0.00007 + (2.5 * 10^{-5})V^{-1} = 0.00007 + (2.5 * 10^{-5})\left(0.421\frac{m^3}{s}\right)^{-1} = 0.000129$$

$$C_V = a(CEPCI) + b(S_f) = (0.000129)(800) + (0.003)\left(16.05\frac{\$}{GJ}\right) = 0.1516\ \$\ \mathrm{m^{-3}}$$

$$C_m = \frac{C_V}{\rho} = \frac{0.1516\,\frac{\$}{m^3}}{995.65\,\frac{kg}{m^3}} = 0.000152\ \$\ \mathrm{kg^{-1}}$$

Low Pressure Steam Pricing using CEPCI and Fuel Cost Correlation

$m = 38{,}706$ kg hr^{-1}	Total mass flowrate of LP steam used in the entire process
$P = 5$ bar	Minimum steam pressure for steam price correlation

a = ?	Utility cost coefficient for steam as describe by Ulrich et al. (2006)
b = ?	Utility cost coefficient for steam as describe by Ulrich et al. (2006)
$CEPCI$ = 800	Chemical Engineering Plant Cost Index for 2022
S_f = 16.05 \$ GJ^{-1}	Specific price of natural gas in Southern California (EIA, 2023)
C_m = ?	Specific price of steam on a mass basis

$$a = (2.3 * 10^{-5})m^{-0.9} = (2.3 * 10^{-5})(38,706\ \frac{kg}{hr})^{-0.9} = 2.71 * 10^{-6}$$

$$b = 0.0034 * P^{0.05} = 0.0034 * (5\ bar)^{0.05} = 0.00368$$

$$C_m = a(CEPCI) + b(S_f) = (2.71 * 10^{-6})(800) + (0.00368)(16.05) = 0.0613\ \$\ \mathrm{kg}^{-1}$$

Dry Air Pricing using CEPCI and Fuel Cost Correlation

m = 542.1 kg hr^{-1}	Total mass flowrate of dry air used in the entire process
M = 0.02896 kg mol^{-1}	Molar mass of air
P_s = 101,325 Pa	Pressure at standard conditions
T = 298 K	Temperature at standard conditions
R = 8.314 J mol^{-1} K^{-1}	Ideal gas constant
V = ? Nm^3 s^{-1}	Total volumetric flowrate of dry air used in the entire process
P = 2 bar	Minimum air pressure for dry air price correlation
a = ?	Utility cost coefficient for dry air as describe by Ulrich et al. (2006)
b = ?	Utility cost coefficient for dry air as describe by Ulrich et al. (2006)
$CEPCI$ = 800	Chemical Engineering Plant Cost Index for 2022

S_f = 16.05 \$ GJ^{-1}	Specific price of natural gas in Southern California (EIA, 2023)
C_V = ?	Specific price of dry air on a normal volume basis
C_m = ?	Specific price of dry air on a mass basis

$$V = \left(\frac{m}{M}\right)\frac{RT}{P_s} = \left(\frac{542.1\,\frac{kg}{hr}}{0.02896\,\frac{kg}{mol}}\right)\left(\frac{1\,hr}{3600\,s}\right)\frac{(8.314\,\frac{J}{mol\,K})(298\,K)}{(101325\,Pa)} = 0.127\ \mathrm{Nm^3\,s^{-1}}$$

$$a = (4.5 * 10^{-5})V^{-0.3}ln(P) = (4.5 * 10^{-5})\left(0.127\,\frac{Nm^3}{s}\right)^{-0.3} ln(2\,bar) = 5.79 * 10^{-5}$$

$$b = (9 * 10^{-4})ln(P) = (9 * 10^{-4})ln(5\,bar) = 0.000623$$

$$C_V = a(CEPCI) + b(S_f) = (5.79 * 10^{-5})(800) + (0.000623)\left(16.05\frac{\$}{GJ}\right)$$

$$= 0.0563\ \$\ \mathrm{Nm^{-3}}$$

$$C_m = C_V\frac{V}{m} = \left(0.0563\frac{\$}{Nm^3}\right)\left(\frac{0.127\,\frac{Nm^3}{s}}{542.1\,\frac{kg}{hr}}\right) = 0.0476\ \$\ \mathrm{kg^{-1}}$$

Rotary Drum Filtration Unit Cost Estimation using Sizing Correlations

a = -73,000	Pricing coefficient for rotary drum filter from Towler and Sinnott (2013)
b = 93,000	Pricing coefficient for rotary drum filter from Towler and Sinnott (2013)
n = 0.3	Pricing exponent for rotary drum filter from Towler and Sinnott (2013)
S = 0.867 mol^2	Filter area

$$C_e = a + bS^n = (-\ 73,000) + (93,000)(0.876)^{0.3} = \$16,366.19$$

Cost of Feedstocks

$\dot{m}$ = 11,200 kg hr^{-1}	Combined mass flowrate of streams 205 and 209
S_P = 0.45 \$ kg^{-1}	Specific price of iron (III) chloride
τ = 7,884 hr yr^{-1}	Operating hours per year
C = ? \$ yr^{-1}	Yearly cost of feed

$$C = \dot{m}S_p\tau = (11,200\ \frac{kg}{hr})(0.45\ \frac{\$}{kg})(7,884\frac{hr}{yr}) = 39,735,360.00\ \$\ yr^{-1}$$

Cost of Utilities

$\dot{m}$ = 1,393,871 kg hr^{-1}	Mass flowrate of stream 111
S_P = 0.000152 \$ kg^{-1}	Specific price of cooling water
τ = 7,884 hr yr^{-1}	Operating hours per year
C = ? \$ yr^{-1}	Yearly cost of utility stream

$$C = \dot{m}S_p\tau = (1,393,871\ \frac{kg}{hr})(0.000152\ \frac{\$}{kg})(7,884\frac{hr}{yr}) = 1,674,194.00\ \$\ yr^{-1}$$

Cost of Electricity

P = 0.0388 MW	Power consumed by pump P-201
S_P = 0.00833 \$ MJ^{-1}	Specific price of electricity
τ = 7,884 hr yr^{-1}	Operating hours per year
C = ? \$ yr^{-1}	Yearly cost of electricity

$$C = PS_p\tau = (0.0388\ \frac{MJ}{s})(0.00833\ \frac{\$}{MJ})(\frac{3600\ s}{1\ hr})(7,884\frac{hr}{yr}) = 9,167.52\ \$\ yr^{-1}$$

Revenue from Products

$\dot{m}$ = 977 kg hr^{-1}	Mass flowrate of stream 414
S_P = 61.5 \$ kg^{-1}	Specific price of lithium hydroxide monohydrate
τ = 7,884 hr yr^{-1}	Operating hours per year
R = ? \$ yr^{-1}	Yearly revenue of product

$$R = \dot{m}S_p\tau = (977\,\frac{kg}{hr})(61.5\,\frac{\$}{kg})(7,884\,\frac{hr}{yr}) = 473,714,082.00\ \$\ \mathrm{yr}^{-1}$$

Revenue from Electricity

P = 1.6128 MW	Power produced by pump FC-301
S_P = 0.00833 \$ MJ^{-1}	Specific price of electricity
τ = 7,884 hr yr^{-1}	Operating hours per year
R = ? \$ yr^{-1}	Yearly revenue of electricity

$$R = PS_p\tau = (1.6128\,\frac{MJ}{s})(0.00833\,\frac{\$}{MJ})(\frac{3600\ s}{1\ hr})(7,884\,\frac{hr}{yr}) = 381,459.46\ \$\ \mathrm{yr}^{-1}$$

APPENDIX C - SUPPLEMENTARY FILES

File Name	Type	Description
heatexchanger_design.xlsx	MS Excel	Heat exchanger sizing
RO Concentration.xlsx	MS Excel	RO inlet concentration
Electrodialysis Cost.xlsx	MS Excel	Electrodialysis cost correlations
Econ Analysis.xlsx	MS Excel	General economic analyis & cash flow
CAPCOST.xls	MS Excel	Equipment pricing
pump_power.m	MATLAB Script	Pump sizing
LNreactorVT1.m	MATLAB Script	Primary lithium reactor modeling
LNreactorVT2.m	MATLAB Script	Secondary lithium reactor modeling
filter.m	MATLAB Script	Rotary drum filter sizing
Capstone Brine Simulation.bkp	ASPEN Simulation	Electrolyte brine simualtion
Silicate & Power Cycle.nkp	ASPEN Simulation	Flash vaporization simulation
Lcryst.bkp	ASPEN Simulation	LiOH crystallization simulation

A Care Ethics Analysis of BP and its Role in the Texas City Isomerization Unit Explosion

A Research Paper submitted to the Department of Engineering and Society

Presented to the Faculty of the School of Engineering and Applied Science
University of Virginia • Charlottesville, Virginia

In Partial Fulfillment of the Requirements for the Degree
Bachelor of Science, School of Engineering

Hailey Elizabeth Hall
Spring 2023

On my honor as a University Student, I have neither given nor received unauthorized aid on this assignment as defined by the Honor Guidelines for Thesis-Related Assignments

Advisor
Benjamin Laugelli, Department of Engineering and Society

Introduction

The Texas City refinery operated by British Petroleum (BP) was once a top producer of oil and gas in the United States, accounting for 2.5% of total domestic supply. On March 23rd, 2005, production came to a sharp halt as boiling hydrocarbons erupted from process equipment in the plant's isomerization (ISOM) unit during start-up, causing an explosion that killed 15 contractors, injured 180 others, and led to immense economic and environmental damages. The U.S. Chemical Safety Board (CSB) identified the incident as the worst refining accident in the United States in 15 years (USCSB, 2008).

The Texas City ISOM explosion was a wake-up call for the chemical engineering industry, bringing about sweeping changes to safety programs across the United States. Scholars and industry professionals alike point to poor safety culture, malfunctional safety interlocks, and numerous physical and managerial process deficiencies as the root causes of the incident (USCSB, 2007). However, these previous analyses fail to assess BP's moral responsibility and the level of care it provided to its employees leading up to the tragedy. By continuously overlooking the relationships and power dynamics between BP and its employees, students may miss the opportunity to learn the importance of adopting both attitudes and actions of care in the workplace.

The lens of care ethics provides a means to assess power dynamics along with attitudes and actions of care between two or more parties. Using the frame of care ethics, I will evaluate the morality of BP as a company leading up to the Texas City ISOM explosion. Specifically, I will highlight the failure of BP to practice responsibility, competence, and reflection on responsiveness towards those who depended on it. BP's failure to responsively, competently, and responsibly provide care will be illustrated using official investigative reports as well as an anonymous survey completed by BP Texas City employees.

Background

On the morning of March 23rd, 2005, a singular board operator began starting up a distillation column designed to separate hydrocarbons in BP Texas City's ISOM unit. The operator filled the distillation column called the raffinate splitter with hot hydrocarbons to an unsafe level, which was not correctly indicated by malfunctioning sensors. These hydrocarbons were allowed to build up in the column until they eventually overflowed into a 50-year-old blowdown drum that vented hydrocarbons directly to the atmosphere. BP had refused to replace the outdated drum after new regulations banned its use in refineries (USCSB, 2007). The subsequent incident prompted investigations by both the CSB and private groups to assess both the technical and organizational failures that led to the accident.

Literature Review

Ample literature exists evaluating the Texas City explosion of 2005. These sources largely point to the human and technical actors that contributed to the downfall of the Texas City refinery; poor process safety culture is an overarching theme between these factors and is frequently identified as the root cause of the incident. Human factors listed by authors focus on errors made by overworked plant operators and poor communication rather than relationships between Texas City employees, management, and BP executives (MacKenzie et al., 2016). Despite the fact that many authors point to the plant's poor safety culture as the cause, little literature exists that examines BP's relationship with plant operators or ethical perspectives on its shortcomings in caring for the Texas City employees and plant.

In “Texas City refinery accident: Case study in breakdown of defense-in-depth and violation of the safety-diagnosability principle in design,” Saleh et al. (2014) cites numerous design errors and locations of on-site housing as issues that contributed to the incident. Poor safety culture in the refinery was also pointed out as a major contributor, as operators frequently deviated from safe operating conditions. The authors conclude that this normalization of deviance influenced the explosion, but the failure of built-in safety systems was the ultimate cause of the disaster in 2005 (Saleh et al., 2014). The review focused on the influence of local management in the plant rather than the culture of BP as a whole. Saleh et al.’s analysis fails to address the systemic issues present in BP’s management overall and the lack of care that BP as a company provided for its workers.

In “The Drive to Virtue: A Virtue Ethics Account of Leadership Motivation,” David Bauman (2017) utilizes virtue ethics to assess the morality of BP executives and the Texas City plant manager at the time of the explosion. The author condemns the lack of temperance of BP’s CEO and Head of Refining, both of whom indulged in lavish lifestyles while implementing sweeping cost cuts that endangered the safety of multiple operations (Bauman, 2017). This book section focuses more largely on BP executives’ roles in the downfall of the plant as compared to Saleh et al. but is largely concerned about the funding provided by BP to Texas City, which is not the only necessary form of care.

While both authors contribute meaningful ideas to discourse on the Texas City explosion, both fail to take into account BP’s failure to provide all necessary forms of care to the refinery. Current literature acknowledges that BP’s management played a role in the explosion but does not assess the company’s moral culpability or its care of employees. In this paper, I will both describe management issues within the Texas City plant and evaluate the morality of BP's actions leading up to the incident.

Conceptual Framework

BP's moral culpability in the Texas City ISOM explosion will be analyzed using a care ethics framework. Utilizing this layout will allow for the careful study of the attitudes and actions of care that BP did or did not exhibit leading up to the Texas City incident. Care ethics was developed by Carol Gilligan and Nel Noddings and provides a normalized structure to assess the roles of interpersonal relationships in determining morality in specific scenarios (van de Poel & Royakkers, 2011). Care ethics emphasizes the fact that morals are developed from relationships and experiences with others rather than through learning sets of ethical rules. This framework views care as a duty and social responsibility for all, with varying degrees of care required depending on the nature of specific relationships. To determine what is morally right from wrong, care ethics suggests that we should practice empathy and try to think from others' perspectives while stressing the importance of taking on both attitudes and actions of care.

Care as an action encompasses "all typically human activities that we carry out to maintain, continue, and repair our world, so that we can live in it as best as we can," (Tronto, 16, 1998). Care as an attitude involves investing appropriate attention and empathy to others in need of care. This care must be provided to human and non-human actors alike, including things such as technological devices and systems. Care ethics breaks stages of care into four distinct parts: attentiveness, responsibility, competence, and responsiveness (Tronto, 1998). Tronto's stages of care and their meanings are summarized below:

Table 1
Stages of Care

Stage of Care	Description
Attentiveness	Perceive needs
Responsibility	Assume responsibility to meet needs
Competence	Perform the necessary caring tasks adequately
Responsiveness	Care receiver responds to given care; Care giver must perceive new needs

The first stage, attentiveness, involves the care giver being open to learning about the needs of the care receiver. Responsibility requires the care giver to then exercise its authority to organize resources to provide for the care receiver. Competence in care is achieved when actions taken to provide care are successful and encompassing of the issue facing the care receiver. Finally, responsiveness relates to the way in which the care receiver responds the care. Based on these responses, the care giver must reevaluate the needs of the care receiver (Tronto, 1998).

Power dynamics and care are intimately linked; care ethics emphasizes the importance of relationships where power distribution is unequal such as that between an employer and employee (van de Poel & Royakkers, 2011). Duties of care for the more powerful party will differ from those of the less powerful party in the network. It is the responsibility of the more powerful party to provide sufficient care for those with less power. In the following section, I will analyze the Texas City ISOM unit explosion by assessing BP’s commitment to each of the four stages of care.

Analysis

Attentiveness

At Texas City, BP was aware of the dangers of outdated and faulty equipment. In early 2005, the Texas City Health, Safety, Security, and the Environment (HSSE) Business Plan identified severe safety deficiencies in the Texas City refinery. In the final report presented to BP executives, the plan stated that the refinery would “kill someone in the next 12-18 months” (USCSB, 177, 2007). By acknowledging the fact that there was a great risk to employees of Texas City, this report makes clear that BP knew that the Texas City refinery was in need of care.

Responsibility

Despite its success in identifying the need for care at Texas City, BP refused to take responsibility for the care of the refinery. This unwillingness to accept responsibility manifested in two forms: major cost-cuts to the plant budget and severe understaffing.

BP’s first critical failure to take responsibility at the Texas City plant surfaced in the form of severe understaffing in many crucial portions of the plant. In its extensive investigation of the Texas City incident, the CSB found the following:

> One board operator was in charge of monitoring and controlling the NDU [Naptha Desulfurization Unit], AU2 [Aromatics Unit #2], and ISOM units… the Board Operator was also responsible for managing the startup of the ISOM raffinate section… Even though the MOC [Management of Change] analysis required two Board Operators for any startup, Texas City management did not implement this recommendation. (USCSB, 86-87, 2006)

These findings reveal troubling trends within the Texas City site. Firstly, the CSB found that the board operator was not only responsible for the technically complex and cognitively intensive job of starting up the raffinate splitter, but also had to monitor two other process units. It is also mentioned that BP required two operators to be present during any startup. However, budget cuts had forced Texas City management to lay off multiple employees, including a number of board operators. Because fewer workers were available and the board operator's responsibilities were expanded, this suggests that employees who remained were required to multitask and run operations that they were not accustomed to performing. These operators also worked longer hours for more consecutive shifts. CSB investigators found that the day board operator in charge of starting up the raffinate splitter "had worked 12-hour shifts for 29 consecutive days" (USCSB, 89, 2006). Staffing shortages at the plant caused by budget cuts caused worker fatigue, impairing the decision-making and reasoning skills required to perform complex startup procedures. Combining worker fatigue and multitasking, it can be reasoned that BP employees were being pushed to the brink of their capabilities. BP's failure to address staffing shortages is representative of its unwillingness to take responsibility for the care of the Texas City employees.

BP's failure to take responsibility and act on known shortcomings is also illustrated in its cost cutting strategies. The Baker Panel, led by former Secretary of State James Baker III, conducted an independent review of the Texas City incident and BP's management strategies. The following excerpt comes from the Panel's findings:

> BP issued a company-wide challenge to each of the refineries to cut their budgets an additional 25 percent without jeopardizing the integrity of the facility…progress toward

> meeting that challenge to cut costs 25 percent became a milestone in each refinery plant manager's performance contract. (Baker et al., 82-83, 2007)

The quote above reveals BP's culture of pressuring plants to cut back on spending while maintaining plant integrity. By issuing a "challenge" rather than mandating a budget cut, it initially appears that BP grants flexibility to its plant managers in their budgeting. However, this careful phrasing belies the immense pressures placed on refineries to meet production demands at all costs while also distancing BP headquarters from the incident. The performance contract mentioned above was an agreement between BP, plant managers, and other high-ranking employees at the refinery that directly determined yearly bonuses (Baker, 28, 2007). By tying financial awards to production and spending habits, BP disincentivized plant managers from spending to repair and update faulty equipment.

As argued above, BP's budgeting pressures signified that adequate care was not being provided to Texas City by the company. However, it could be argued that it was the Texas City plant manager who failed to provide this care by adhering to BP's budgeting demands for personal benefit. In reality, the Texas City plant manager was deeply concerned about the safety issues present at the refinery and could not take responsibility for plant funding. The CSB found that the plant manager organized and compiled safety data from the plant to create a presentation to appeal for increased funding from upper management.

> The presentation, 'Safety Reality,' was intended as a wakeup call to site supervisors that the plant needed a safety transformation, and included a slide entitled 'Texas City is not a safe place to work'… The 'Safety Reality' presentation concluded that safety success begins with compliance, and that the site needed to get much better at controlling process safety risks. (USCSB, 172, 2007)

The plant manager intended to leave a bleak message in choosing the title of his final slide, “Texas City is not a safe place to work.” This phrasing conveys a sense of urgency to fix the process safety issues present at the plant before further incidents occur. Considering that this presentation was designed to convince executives that the Texas City site needed increased funding, it appears that the budgeting “challenge” issued by BP to plant managers was much less optional than initially suggested. As such, it can be reasoned that the Texas City plant manager did not have the authority to increase the refinery’s budget and thus cannot be held responsible.

It was only after this sobering presentation that BP slightly eased budgeting expectations for the Texas City refinery in 2005. BP still expected the plant to cut its budget by 12.5% (USCSB, 172, 2007). This relentless cost cutting meant that safety systems could not be adequately repaired. In failing to reduce budget cuts and promote safe practices, BP failed to take responsibility for the care of its employees and diverted blame to local plant management.

Though multiple reports and accounts identified serious budget shortages and staffing deficiencies at the Texas City refinery, no actions were taken by BP to address these problems at the plant. This indicates that BP would not accept responsibility for the care of the Texas City refinery.

Competence

Because BP could not identify the difference between personal and process safety, the actions taken by the company leading up to the explosion fall far short of competent care. Though BP ultimately refused to meaningfully increase the budget and staffing for the Texas City refinery, some actions were being taken by executive BP managers to repair the rapidly deteriorating safety in the plant at a surface level. After a series of safety audits performed in early 2004, BP executives implemented new safety rules and standards at the Texas City refinery. In a press release after the incident, Don Holmstrom, the CSB supervising investigator of the Texas City explosion, commented on the safety of Texas City prior to the incident:

> In 2004, BP Texas City had the lowest injury rate in its history, nearly one-third the oil refinery sector average… the injury rate does not take account of catastrophic hazards or distinguish between injuries and fatalities. That year, the refinery experienced three major accidents that resulted in a total of three fatalities. (CSB, 2007)

It is clear from its low injury rates that BP took measures to better safety programs at the Texas City plant. However, as Don Holmstrom notes, the lowering of injury rates at the plant does not necessarily mean that major equipment-related accidents were reduced. Understanding this difference between personal and process safety is critical to analyzing the competency of BP's safety policies and its apparent success in improving safety at the plant. The Center for Chemical Process Safety (CCPS) defines process safety as "a disciplined framework for managing the integrity of operating systems and processes handling hazardous substances by applying good design principles, engineering, and operating practices" (CCPS, 1, 2022). In short, process safety encompasses the maintenance and safe operation of all process equipment within the plant. This form of safety is closely tied to the idea of providing care to technology; without proper attention, the equipment will degrade and become less safe over time. Actions and attitudes of care must be adopted to ensure that the process remains reliable and safe. Meanwhile, personal safety relates to the slips, trips, and falls that affect singular individuals (AIChE, 2008). Incidents related to process safety tend to impact larger numbers of people than those from a personal safety standpoint.

Holmstrom reveals that BP used personal injury rates as a metric for safety within the refinery. However, injury rates are a poor indicator of process safety. Rather, they indicate the strength of the personal safety program in a plant. By selecting to use personal injury rates as a safety metric, BP unwittingly revealed its naivety in assessing and implementing safety needs of the Texas City plant. This also implies that process safety was not the main focus of the new standards and rules implemented by BP. The combination of low injury rates and no awareness of the difference between process and personal safety was dangerous; BP believed it had solved a majority of the safety issues at the Texas City plant as process safety continued to degrade. This is once again illustrated in the three deaths that occurred in 2004. As mentioned by Holmstrom, BP did not indicate the severity of injuries or fatalities within its injury rates. All three deaths were results of equipment failures that caused fires and explosions on site, linking them to process safety. Though BP exhibited an exemplary personal safety program, its failure to analyze the root causes of the three fatalities in 2004 is a strong indication of a weak process safety culture. In failing to distinguish process from personal safety, BP did not provide competent care to its employees.

Responsiveness

At the Texas City refinery, plant operators and contractors bore the brunt of BP’s cost-cutting practices and poor process safety culture. Though these workers were the less powerful party in the relationship between BP and its employees, contractors and operators had the expertise and hands-on experience that kept the plant running. BP owed these employees its care as the more powerful party. It was these workers who lived the changes in safety culture implemented by BP executives, which they found insufficient. In an anonymous survey of West Plant employees at Texas City in 2004, participants were asked “What would improve West Plant as a place to work?” (Boudreau & Yager, 2010). An excerpt from a response from a West Plant employee illustrates workers’ perspectives on safety systems at Texas City:

> This company deliberately put my life in danger to try and save a buck. This has happened more than once, but the company almost cost me my life this time. (Boudreau & Yager, 2010)

This worker not only claims that BP's management of the Texas City site is still unsafe, but also says that BP did this "deliberately" in order to save money. This reflects one of the aspects of care that BP refused to take responsibility for at Texas City: budget. The worker also claims that this has happened multiple times during his or her career. From this quote, it can be reasoned that BP's inability to accept responsibility negatively influenced worker morale at the Texas City site. Employees felt that BP valued profit over safety even with the implementation of personal safety programs. The quote implies that these personal safety programs were not received well; workers had identified the fact that the greatest risk came from failure to address process safety rather than personal safety. Despite BP's advances in personal safety culture, these comparatively minor actions were overshadowed by the forms of care it refused to provide to Texas City. Employees at Texas City did not appreciate the new rules that BP had put into place relating to personal safety; rather, they felt that BP had failed to provide the care that they needed as the less powerful party in their asymmetrical power relationship. It is also important to note that providing care is a cyclical process. After receiving negative feedback, BP needed to reevaluate its strategies to provide adequate care to its employees. Ultimately, BP did not change its course of action based on feedback it received from this survey. In failing to reevaluate the needs of plant workers, BP failed to respond appropriately.

Conclusion

BP failed to exhibit three critical aspects of care in practice leading up to the Texas City ISOM unit explosion: responsibility, competence, and responsiveness to feedback. In addition, BP did not uphold its role to protect and care for Texas City employees as the more powerful party in the relationship. Analyzing this case from a care ethics perspective, it was concluded that BP acted immorally as it did not fully commit to adopting actions and attitudes of care at the Texas City refinery.

In the absence of appropriate care, technologies can critically fail, permanently impacting the lives of those they touched. Engineers are not just responsible for the design of new technology; they are also accountable for ensuring that care is provided to both the technology itself and its users. To make moral decisions as an engineer, considering the actions and attitudes of care that are required to sustain and develop technology is essential. By using care ethics to both practice empathy and consider the opinions of others in our decision-making, we can create a roadmap to a better future.

References

AIChE. (2008). *What is "process safety"?* https://www.aiche.org/sites/default/files/cep/20080738.pdf

Baker, J., Bowman, F., Erwin, G., Gorton, S., Hendershot, D., Leveson, N., Priest, S., Rosenthal, I., Tebo, P., Wiegmann, D., & Wilson, L. (2007). *The report of the BP U.S. refineries independent safety review panel*. http://sunnyday.mit.edu/Baker-panel-report.pdf

Bauman, D. C. (2017). The drive to virtue: A virtue ethics account of leadership motivation. In A. J. G. Sison, G. R. Beabout, & I. Ferrero (Eds.), *Handbook of virtue ethics in business and management* (pp. 961–971). Springer Netherlands. https://doi.org/10.1007/978-94-007-6510-8_51

Boudreau, A., & Yager, C. (2010, June 16). *BP documents highlight PR strategy after deadly Texas blast*. CNN. http://www.cnn.com/2010/US/06/16/bp.refinery.reaction/index.html

CCPS. (2022). Introduction and regulatory overview. In *Process safety for engineers: An introduction* (2nd ed., p. 1). Wiley.

CSB. (2006, October 30). *CSB investigation of BP Texas City refinery disaster continues as organizational issues are probed*. Retrieved February 27, 2023, from https://www.csb.gov/csb-investigation-of-bp-texas-city-refinery-disaster-continues-as-organizational-issues-are-probed/

MacKenzie, C., Holmstrom, D., & Kaszniak, M. (2007). Human factors analysis of the BP Texas City refinery explosion. *Proceedings of the Human Factors and Ergonomics Society Annual Meeting*, *51*(20), 1444–1448. https://doi.org/10.1177/154193120705102015

Saleh, J. H., Haga, R. A., Favarò, F. M., & Bakolas, E. (2014). Texas City refinery accident: Case study in breakdown of defense-in-depth and violation of the safety–diagnosability principle in design. *Engineering Failure Analysis*, *36*, 121–133. https://doi.org/10.1016/j.engfailanal.2013.09.014

Tronto, J. C. (1998). An ethic of care. *Generations: Journal of the American Society on Aging*, *22*(3), 15–20. http://www.jstor.org/stable/44875693

USCSB. (2007). *Investigation report: Refinery explosion and fire.* https://www.csb.gov/bp-america-refinery-explosion/

USCSB. (2008, June 2). *CSB safety video: Anatomy of a disaster* [Video]. Youtube. https://www.youtube.com/watch?v=XuJtdQOU_Z4

van de Poel, I., & Royakkers, L. (2011). Care ethics. In *Ethics, technology, and engineering* (pp. 102–103). Wiley-Blackwell.

Prospectus

Introduction

With increased public consciousness of climate change driven by combustion of fossil fuels, demand for electric vehicles (EVs) has risen across the globe (Desilver, 2021). In the United States alone, EV sales nearly doubled between 2020 and 2021 with projections showing future increases in demand (Desilver, 2021). With pressures to ramp up EV production, lithium prices and markets have expanded, as a majority of EVs rely on rechargeable lithium-ion batteries. Lithium is commonly imported from South America, China, and Australia, though small processing plants exist within the United States (Warren, 2021). To decrease reliance on foreign suppliers, the Biden administration recently allocated $2.8 billion to fund development of battery manufacturing and lithium extraction infrastructure within the U.S. (United States Department of Energy, 2022). As EV production becomes increasingly important, establishing a domestic lithium supply is crucial.

The Salton Sea, located in southern California, possesses massive, untapped quantities of lithium in its geothermal brines with concentrations as high as 400 ppm (McKibben et al., 2021). Extensive research has been performed to find ways to extract lithium from the brine without utilizing environmentally damaging techniques such as evaporative extraction, a challenging task considering the identical charges and similar sizes of other monovalent cations present at much higher concentrations in brine (G. Geise, personal communication, October 7, 2022). Using chemical models, I will propose an environmentally friendly plant design for production of lithium hydroxide for use in rechargeable batteries.

In addition to technological setbacks, social factors have also significantly hindered development of lithium extraction infrastructure. Drawing parallels between the Salton Sea in the

United States and Bolivia’s Salar de Uyuni allows for analysis of social factors that heavily influence the success or failure of lithium production such as government and public perception, environmental and economic impacts at the local scale, and nationalistic values (Sanchez-Lopez, 2019). Understanding these social factors will aid in development and implementation of lithium extraction infrastructure in the U.S.

Considering both social and technological sides of lithium production is essential to creating successful lithium extraction infrastructure in the United States. Herein, I propose a plant design for production of battery-grade lithium hydroxide at a rate of 2,500 tons per year. I will examine the human and non-human actors of lithium production using actor network theory to study the Salar de Uyuni to determine what actors contribute to Bolivia’s lagging lithium development program.

Technical Prospectus Proposal

With technological advancements in electric vehicles and batteries, global demand for high-energy density materials, such as lithium, has increased significantly. It is estimated that rising demand will push production of lithium from 447 thousand tons of lithium carbonate equivalent in 2018 to over 2 million tons by 2050 (Stringfellow & Dobson, 2021).

Currently, the United States relies on lithium imported from Chile and Argentina, where an energy intensive and environmentally damaging process known as evaporative extraction is utilized (Warren, 2021). Geothermal brines from the Salton Sea in California contain a significant amount of lithium along with trace quantities of other valuable elements, such as rubidium and cesium. Directly adsorbing lithium from Salton Sea brines offers an attractive, environmentally conscious alternative to meet increasing lithium demands. With eleven geothermal wells drawing from the Salton Sea in California, lithium extraction holds the potential to produce $5 billion annually (Jones et al., 2022).

For this project, we propose a plant design to extract lithium and other valuable metals from an existing 6,000 gal/min well located in the Salton Sea (Ventura et al., 2020). A single well has the potential to produce 2,500 ton/yr of lithium. The plant can be separated into three distinct sections: pre-treatment, lithium extraction, and alternative products capture. Pretreatment of the feed involves the removal of silicates from brine by introducing calcium hydroxide to precipitate iron silicates, which are then physically filtered from the solution (G. Koenig, personal communication, October 10, 2022). Once silicates are removed, the stream is passed through a boiler, where the hot brine is used to produce high pressure vapor for geothermal power plants.

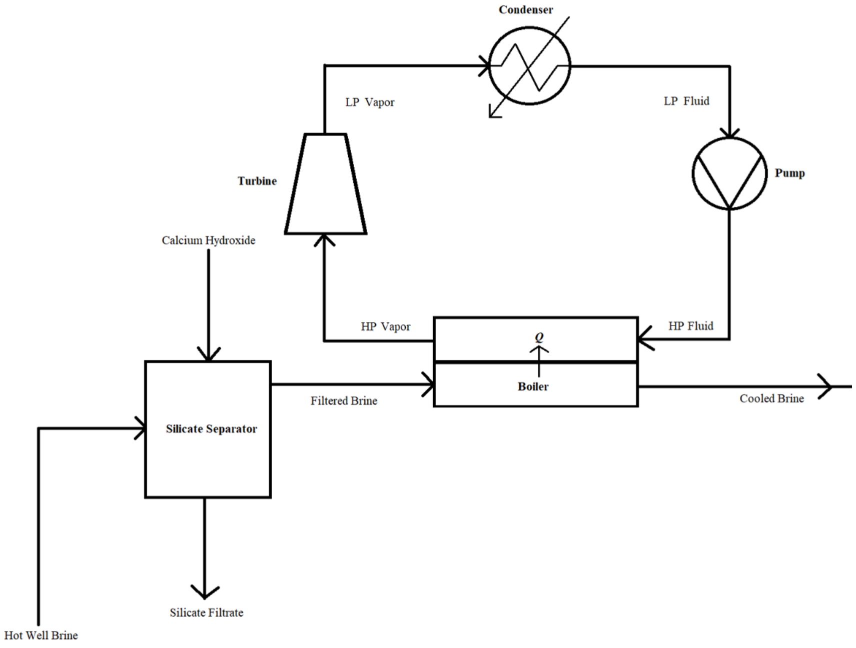

Figure 1. Process Flow Diagram of Brine Pretreatment

After passing through the power plant, cooled brine is processed using a series of packed bed reactors containing iron (III) phosphate, which selectively adsorbs lithium through a reduction-oxidation (redox) reaction (Geise, personal communication, 2022). The spent brine is then sent away for further product extraction. After reaching sorption capacity, iron (III) chloride is then fed to the reactor, which reacts with the lithium iron (II) phosphate to regenerate iron (III) phosphate and lithium chloride. The packed bed reactors are operated such that half are in adsorption mode and half are in regeneration mode to ensure the process is continuous.

Lithium-rich brine is then sent to an electrolysis unit, which selectively isolates lithium ions from chloride and iron ions via a redox reaction. Chloride ions from brine (Cl^-) are oxidized at the anode to form chlorine gas (Cl_2), while water is reduced at the cathode to form hydroxide ions (OH^-). Lithium ions pass from the anode to the cathode to form lithium hydroxide monohydrate ($LiOH{\cdot}H_2O$), which is sent to a crystallization unit for further purification. Oxygen (O_2) and hydrogen (H_2) gas are produced as side products as well as iron (III) chloride, which can be reused in the reactor.

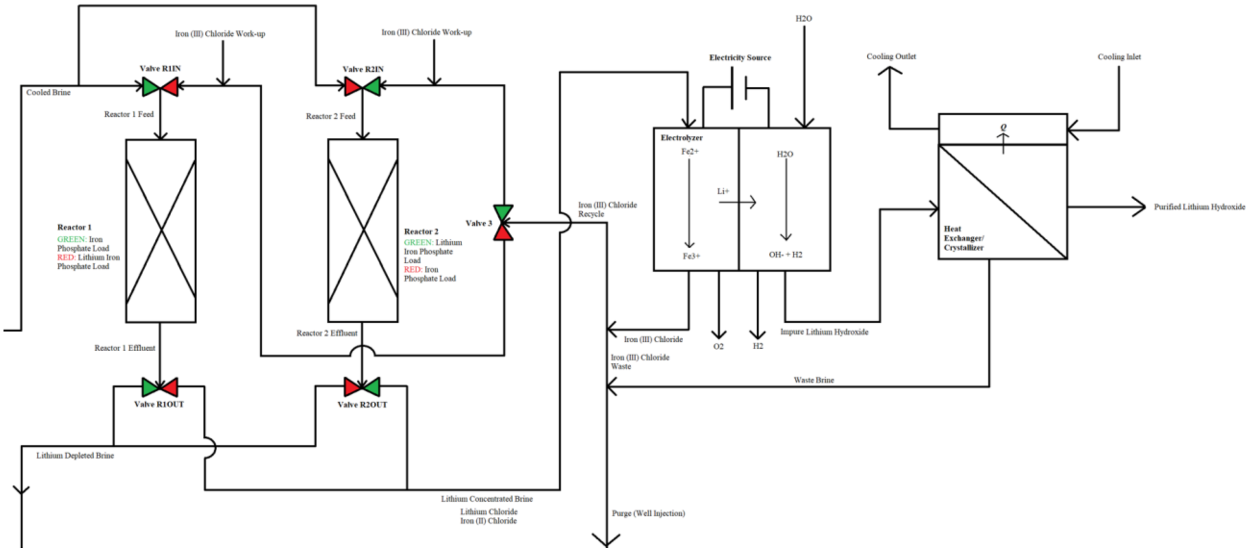

Figure 2. Process Flow Diagram of Lithium Extraction

Additional product capture involves the extraction of alkali metals from spent brines. While only present in small concentrations, rubidium (32 ppm) and cesium (6 ppm) have high market values (Warren, 2021). Rubidium and cesium can be selectively separated from other minerals via an ion exchange process using zeolite-based sorbents (Neupane & Wendt, 2017). A similar operation structure to the lithium extraction process could be implemented to extract rubidium and cesium products.

For proprietary adsorption and electrolysis unit operations, experimental design data will be sourced from professors Gaurav Giri, Gary Koenig, and Geoff Geise. Additional information regarding other components of the process, such as other alkali metals capture, will be acquired through peer reviewed journals. Data will be consolidated into a thermodynamic model using Aspen Plus design software with the Electrolyte-Nonrandom Two-Liquid equations activity model (ELECNRTL) which has shown to be successful in simulating high temperature and pressure brines in previous literature (Foley et al., 2019). Over the course of two semesters in CHE 4474 and CHE 4476, this project will be completed as a team of five members. Work will be divided equally where each member will focus on a specific unit operation's design and economic analysis; a project management tool, such as a Gantt chart, will be used to assess group progress.

STS Project Proposal

Before the late 1970s, the Uyuni salt flat located in Bolivia was virtually unknown. When the United States performed a geological survey on the region in 1977, the Salar de Uyuni came into the world's public eye with the discovery of vast mineral reserves in brines below the desert's salty crust (Sanchez-Lopez, 2019). The report revealed that the salt flat contained massive quantities of lithium, now the key element of rechargeable batteries. As calls for lithium-based batteries grow with rising interest in EVs, Andean salt flats like the Salar de Uyuni in Bolivia will face increased production demands (Berg, 2021). Whereas Chile and Argentina act as global leaders in lithium production due to their own mineral-rich salt flats, the Salar de Uyuni remains largely undeveloped (Quinteros-Condoretty, 2020). Argentinian and Chilean mining companies extract lithium from brine water underneath salt flats through a process known as evaporative extraction, which Bolivians could also employ. Mineral-rich solution is pumped from underground into large ponds to evaporate for a span of 18 to 24 months (Sanchez-Lopez, 2019). Chemicals are introduced to the highly concentrated solution, which then passes through a plant that performs multiple purification steps to produce lithium carbonate (Li_2CO_3) or lithium hydroxide monohydrate ($LiOH \cdot H_2O$) as final products (Warren, 2019). Lithium produced in these processes then gets shipped overseas to battery producers. Though the Salar de Uyuni contains 26.5% of the world's lithium supply, Bolivia's state-controlled lithium extraction agency, Yacimientos de Litio Bolivianos (YLB), has only built one evaporative extraction pilot plant (Bos & Forget, 2021). As demands for lithium grow globally, the Bolivian government and people have the opportunity to earn significant revenue from the Salar de Uyuni with the potential to lessen the high levels of poverty present in the nation (Quinteros-Condoretty, 2020). By failing to invest in lithium infrastructure, the Bolivian government risks giving up a significant source of income for its people. Despite Bolivia's abundant brine reserves, it has yet to match raw lithium outputs of Chile or Argentina.

Some assert lithium mining in Bolivia has flagged due to environmental concerns, negative impacts on tourism, and local disputes over land ownership (Sanchez-Lopez, 2019). However, this analysis fails to address the complex relationship between the lithium-rich salt flat, the Bolivian government, and Bolivia's past as a colonial territory. The Bolivian government, which retains total control over lithium production in Bolivia, pushes a nationalistic agenda that demands more than extraction of raw lithium; rather, it calls for manufacturing of lithium end-use products such as batteries and electric vehicles within Bolivia (Seefeldt, 2020). Lasting impacts of resource exploitation under Spanish colonial rule contribute to concerns over production of raw materials and potential for other countries to take advantage of Bolivia's natural resources (Seefeldt, 2020). Further development of lithium from its raw form requires infrastructure that Bolivia lacks, but the government is hesitant to grant access to its lithium resources to foreign parties (Quinteros-Condoretty, 2020). Social factors such as politics and both nationalistic and local values contribute to the current lack of lithium mining infrastructure in the Salar de Uyuni.

I argue that Bolivian nationalism, negative environmental and economic impacts on communities, and Bolivia's past under Spanish colonial rule have stymied lithium mining efforts thus far. Social factors stemming from these issues including reluctance to work with multinational partners, desire to manufacture end-use products, and a rapidly evolving political landscape has set back lithium production in Bolivia. I will build my argument using the science, technology, and society (STS) framework of actor-network theory (ANT), which analyzes the roles of numerous human and non-human actors that come together to achieve a common goal under the guidance of a network builder (Callon, 1987). I will apply translation theory, a subset of ANT, to investigate how networks form (Callon, 1987). Specifically, I will delve into how the Bolivian government formed a network for lithium production to understand the actors that contribute to setbacks in lithium mining operations. To perform this analysis, I will utilize press releases and reports from Bolivia and YLB, original United States geological surveys, and Bolivian laws and regulations on lithium production.

Conclusion

In the technical portion of this paper, we will design an environmentally conscious lithium extraction plant for the production of high purity lithium hydroxide monohydrate using Aspen Plus design software. For the STS research paper, I will utilize actor-network theory to determine how human and non-human actors contribute to and restrict progress of lithium production in Bolivia’s Salar de Uyuni and why it has failed thus far. By assessing both technical and social aspects, I will address concerns over performance of lithium production plants, emphasizing the importance of government and society’s perspective on lithium mining operations and implementation of a cleaner, more cost-effective lithium extraction technique. By understanding technical and social factors that contribute to the success or failure of lithium mining operations, we can effectively implement lithium extraction infrastructure to meet increasing demands and create a road map for a sustainable future.

References

Berg, R. (2021, August 17). *South America's lithium triangle: Opportunities for the Biden administration*. Center for Strategic and International Studies. https://www.csis.org/analysis/south-americas-lithium-triangle-opportunities-biden-administration

Bos, V., & Forget, M. (2021). Global production networks and the lithium industry: A Bolivian perspective. *Geoforum*, *125*, 168–180. https://doi.org/10.1016/j.geoforum.2021.06.001

U.S. Department of Energy. (2022). *Biden-Harris administration awards $2.8 billion to supercharge U.S. manufacturing of batteries for electric vehicles and electric grid*. https://www.energy.gov/articles/biden-harris-administration-awards-28-billion-supercharge-us-manufacturing-batteries

Callon, M. (1987). Society in the making: The study of technology as a tool for sociological analysis.

Desilver, D. (2021). *Today's electric vehicle market: Slow growth in U.S., faster in China, Europe*. Pew Research Center. https://www.pewresearch.org/fact-tank/2021/06/07/todays-electric-vehicle-market-slow-growth-in-u-s-faster-in-china-europe/

Foley, S., Gordon, A., Hong, S., & Ye, B. (2019). *Design of a geothermal power plant with downstream mineral extraction* [Scholarly project].

Jones, B., & McKibben, M. (2022). *How a few geothermal plants could solve America's lithium supply crunch and boost the EV battery industry*. UC Riverside College of Natural & Agricultural Sciences. https://cnas.ucr.edu/media/2022/03/21/how-few-geothermal-plants-could-solve-americas-lithium-supply-crunch-and-boost-ev

McKibben, M., Elders, W., & Raju, A. (2021). Lithium and other geothermal mineral and energy resources beneath the Salton Sea. *Crisis at the Salton Sea: Research Gaps and Opportunities*, 107-122.

Neupane, G., & Wendt, D. S. (2017). Assessment of mineral resources in geothermal brines in the US. *OSTI*, 13–15. https://www.osti.gov/servlets/purl/1402042

Quinteros-Condoretty, A. R., Albareda, L., Barbiellini, B., & Soyer, A. (2020). A socio-technical transition of sustainable lithium industry in Latin America. *Procedia Manufacturing*, *51*, 1737–1747. https://doi.org/10.1016/j.promfg.2020.10.242

Sanchez-Lopez, M. D. (2019). From a white desert to the largest world deposit of lithium: Symbolic meanings and materialities of the Uyuni salt flat in Bolivia. *Antipode*, *51*(4), 1318–1339. https://doi.org/10.1111/anti.12539

Seefeldt, J. (2020). Lessons from the lithium triangle: Considering policy explanations for the variation in lithium industry development in the “lithium triangle” countries of Chile, Argentina, and Bolivia. *Politics & Policy*, *48*(4), 727–765. https://doi.org/10.1111/polp.12365

Stringfellow, W. T., & Dobson, P. F. (2021). Technology for the recovery of lithium from geothermal brines. *Energies*, *14*(20), 6805. https://doi.org/10.3390/en14206805

Ventura, S., Bhamidi, S., Hornbostel, M., Nagar, A., & Perea, E. (2016). Selective recovery of metals from geothermal brines. *SRI International*. https://doi.org/10.2172/1336270

Warren, I. (2021). Techno-economic analysis of lithium extraction from geothermal brines. *National Renewable Energy Lab.* https://doi.org/10.2172/1782801